The Planetary Science Journal, 4:162 (36pp), 2023 September https://doi.org/10.3847/PSJ/acebed

Stratigraphy, Crater Size–Frequency Distribution, and Chronology of Selected Areas of Ganymede's Light and Dark Terrains

Namitha Rose Baby[1], Roland J. Wagner[1], Katrin Stephan[1], and Thomas Kenkmann[2]
[1] Institute of Planetary Research, German Aerospace Center (DLR), Berlin, Germany; Namitha.Baby@dlr.de
[2] Institute of Earth and Environmental Sciences—Geology, Albert-Ludwigs-University Freiburg, Freiburg, Germany
Received 2023 January 16; revised 2023 July 25; accepted 2023 July 26; published 2023 September 12

Abstract

The stratigraphy of the largest natural satellite of our solar system, Ganymede, is investigated using available global mosaic (basemap) and high-resolution images. We are focusing on the reconstruction of the formation and tectonic evolution of selected areas of dark and light terrain units and investigate their morphological characteristics and relative ages at a local scale using high-resolution images from the sub-Jovian and anti-Jovian hemispheres. For this, geological maps and crater size–frequency distributions for each of the terrain units were prepared, and relative as well as absolute ages were derived by applying the currently available lunar-derived impact chronology model and the Jupiter-family comet chronology model. The relative ages obtained from the cross-cutting relationships of terrain units are not always consistent with the ages derived from the crater size–frequency distributions. Some regions are influenced by secondary and sesquinary craters and tectonic resurfacing activities. Independent of the applied model, the derived crater size–frequency distribution showed that the light terrain started to form soon after the completion of dark terrain formation.

Unified Astronomy Thesaurus concepts: Ganymede (2188); Jupiter (873); Jovian satellites (872); Tectonics (2175); Galilean satellites (627); Natural satellite surfaces (2208)

1. Introduction

The Jovian satellite Ganymede, the major target of ESA's upcoming JUICE (JUpiter ICy moons Explorer) mission (Grasset et al. 2013; The JUICE Science Working Team 2014), exhibits a complex geology. The surface of Ganymede is dominated by two major geologic units. Approximately 35% of the surface is covered by so-called dark terrain, which is heavily cratered and represents the oldest preserved surface on Ganymede (Pappalardo et al. 2004). The dark terrain is cross-cut by a somewhat younger, so-called "light" terrain that shows strong indications for tectonic resurfacing (Pappalardo et al. 2004; Jaumann et al. 2022). It forms a complex network, surrounds and cross-cuts the dark terrains and builds up about 65% of Ganymede's surface. The tectonic pattern of the light terrain is a major key for understanding Ganymede's formation and geologic evolution.

In order to prepare for the JUICE mission (Grasset et al. 2013) and to refine the science questions and the requirements for the observations made by the Jovis, Amorum ac Natorum Undique Scrutator (JANUS) camera (Palumbo et al. 2014), as well as to evaluate the currently available methods and models for investigating Ganymede's geologic history, we reinvestigate the stratigraphic relationships of Ganymede's geologic terrains and particularly the light terrain units on the local scale at those locations on Ganymede's surface for which high-resolution imagery is available. We use cross-cutting relationships and crater-counting tools to derive the local geological history. The regions chosen for this study are strongly tectonized light terrains composed of different subunits. This study complements the work of Patterson et al. (2010) and Collins et al. (2013) at the local scale. The goal is to deepen our knowledge on the local formation processes of the light terrain, to evaluate changes in tectonic style through time across Ganymede, and/or to identify possible differences and similarities of the light terrain at different locations, but also various degrees of resurfacing. Further, we evaluate the currently available methods of deriving surface ages by crater size–frequency distribution measurements in order to verify previous estimations of the geologic age of Ganymede's light terrain units and the time of their formation with respect to Ganymede's evolution.

2. Database, Data Processing, and Selection of Study Areas

2.1. The Voyager and Galileo Missions and a Description of Their Imaging Instruments

In 1979, Voyagers 1 and 2 observed the surface of Ganymede at spatial resolutions up to 470 m pixel^{-1}, with an average of 1–2 km pixel^{-1} (Smith et al. 1977,1979a,1979b; Kersten et al. 2021). The Voyager Imaging Experiment encompassed a narrow angle (NA) and a wide angle (WA) Vidicon camera on each Voyager spacecraft. Both cameras could take images through several color filters ranging from 346 nm (UV) to ∼600 nm (red/orange), including a panchromatic (broadband) or clear filter (Smith et al. 1977).

Prior to the first Voyager flybys, NASA had been planning a mission with a Jupiter orbiter and an atmospheric probe, which was called Galileo. Images could be taken with an NA camera through eight color filters ranging from ∼400 nm (violet) to 968 nm (near-infrared) including a panchromatic or clear filter.

Galileo was inserted into Jupiter orbit in 1995 December and performed 34 orbits until it was set on an impact course with Jupiter's atmosphere in 2003 September. Orbits were increasingly numbered and designated according to the main satellite target chosen for a close flyby (G: Ganymede, C: Callisto, E: Europa, and I: Io). During the Galileo Prime Mission (orbits G1 through E11) Ganymede was selected for a close flyby in orbits G1, G2, G7, and G8. The gaps at the leading and trailing hemisphere left by Voyager could be filled in orbits E6 and C9, but only at spatial resolutions comparable to Voyager (C9), or even less (E6). In the two mission extensions, Galileo Europa Mission (GEM; orbits E12–I25) and Galileo Millennium Mission (GMM; orbits E26–A34, i.e., Amalthea flyby, no images taken), Ganymede was chosen in orbits G28 and G29 for two further close flybys.

Despite 34 orbits the loss of the High Gain Antenna (HGA) resulted in a significantly incomplete imaging at regional (100–300 m pixel^{-1}) and especially high ($\ll$100 m pixel^{-1}) resolution of Ganymede's surface, often resulting in mostly spatially isolated high-resolution images, which complicates efforts to derive an overall picture of Ganymede's geology, in terms of the extent of geologic units, measurements of their superimposed crater size–frequency distributions, and styles of tectonic deformations. Nevertheless, we could define four study areas (Regions A to D, Section 2.3) that are covered by up to three sets of 1 × 2, 2 × 2, or 2 × 3 Galileo Solid State Imaging (SSI) footprints (Figure 1 and Table 1). These regions cover light terrains that range from narrow bands to extensively resurfaced portions and a complex network of light terrains. Each region offers a view into the direct contact between the light and adjacent ancient dark terrains.

2.2. Data Processing

Geologic mapping, measurements of crater size–frequency distributions, and tectonic analyses are based on image mosaics exclusively produced at the DLR Institute of Planetary Research, Berlin. Mostly, the processing of images was carried out using the Video Image Communication and Retrieval (VICAR) program package developed by the Multi-Mission Image Processing Laboratory (MIPL) at JPL. For specific tasks, programs of the Integrated Software for Images and Spectrometers (ISIS) program package developed at the U. S. Geological Survey were used alternatively.

To generate image mosaics, several steps of systematic processing are necessary. In the first step, errors in data transfer, dark currents, and blemishes are corrected and a radiometrically calibrated image is produced. Calibration files and VICAR or ISIS programs are project and camera specific (Smith et al. 1977; Benesh & Jepsen 1978; Danielson et al. 1981; Klaasen et al. 1984; Belton et al. 1992). For the Voyager cameras an additional processing step is needed to correct distortions of the camera telescopes and of the Vidicon tubes geometrically (Smith et al. 1977; Benesh & Jepsen 1978). The second step is the map projection of images, based on a Voyager-derived control net (Davies & Katayama 1981), and on camera pointing information from the Navigation Ancillary Information Facility (NAIF) at JPL for the Galileo SSI images (Davies et al. 1998). From the map-projected images, local mosaics or a global image basemap can be created.

In this work we used a controlled global basemap, based on updated Ganymede radii and a new set of control points (Archinal et al. 2011; Zubarev et al. 2015, 2016; Kersten et al. 2021). The basemap also provides an essential planning tool for Ganymede imaging with the JANUS camera aboard the upcoming ESA JUICE Mission to Ganymede and the Galilean satellites (Grasset et al. 2013; Stephan et al. 2021). In agreement with the JUICE Task Group for the satellite coordinate systems, cartography, and nomenclature, east longitudes are used. The map resolution is 128 pixels degree^{-1}, corresponding to a map scale of 358.774 2 m pixel^{-1} (Kersten et al. 2021).

Since most of the areas of interest we selected for this work were imaged at spatial resolutions much higher than 358 m pixel^{-1}, we created local context mosaics. For this task, the basemap was zoomed up to the original map scale of each selected SSI target area, and the SSI frames from each area were registered manually onto the basemap. In addition, we applied high-pass filters to enhance the contrast and small-scale details in the Galileo SSI images. Depending on the geographic location of each target area, each context mosaic was reprojected into either a Mercator projection for locations in equatorial latitudes (±22°), or Lambert conformal with two standard parallels for the midlatitudes (±31° to ±66°).

2.3. Study Areas

Region A lies in the northern portion of Ganymede's anti-Jovian hemisphere, where Nippur Sulcus adjoins the dark terrain of Marius Regio with the Regio cross-cut by narrow bands of light material such as Byblus Sulcus (Figure 1(b)). Three high-resolution SSI observation sequences (50–300 m pixel^{-1}) cover several parts of this region (G2GSNIPPUR01, G2GSGRLVNS01, and G2GSTRANST01) with G8GSREGCON01 (936 m pixel^{-1}) offering the context of these SSI observations.

In contrast, Region B (Figure 1(c)) and C (Figure 1(d)) cover parts of Ganymede's sub-Jovian southern hemisphere. Region B is fully located within the dark ancient terrain of Nicholson Regio and cross-cut by the narrow but extended band of Arbela Sulcus. Region C, on the other hand, combines high-resolution observations that cover parts of Harpagia Sulcus. The Sulcus adjoins Nicholson Regio at its eastern border and represents an extended heavily resurfaced light terrain. Whereas Region B was observed by two sequences of SSI observations (G7GSNICHOL01 and 28GSARBELA02, 100–300 m pixel^{-1}) combined in two image mosaics, Harpagia Sulcus in Region C was imaged with high resolution between 100 and 300 m pixel^{-1} at three different locations (28GSBRTDRK02, 28GSSMOOTH02, and 28GSCALDRA02). Portions of Regions B and C were also imaged at very high resolution better than 50 m pixel^{-1} (Figure 1, SSI observations: 28GSARBELA01, 28GSBRTDRK01, 28GSSMOOTH01, and 28GSCALDRA01). Although these images were not analyzed in detail, they were considered in the geologic mapping procedure (see Section 3).

Like Region A, Region D (Figure 1(e)) is situated on Ganymede's anti-Jovian hemisphere, but in the southern hemisphere. It covers portions of Mummu, Sippar, and Erech Sulcus with the latter adjoining Marius Regio at its southern border. Mummu Sulcus is covered by a sequence of SSI observations (G8GSCALDRA01, 100–300 m pixel^{-1}), whereas Sippar and Erech Sulcus are imaged by two overlapping SSI images (100–300 m pixel^{-1}) of the G8GSERECH01 observation sequence.

3. Methodology

3.1. Mapping Procedure

Geologic mapping was performed for each of the high-resolution Galileo SSI images covering the study areas (Figure 1). Mapping units and their formation are defined by (i) their albedo characteristics, i.e., from light to dark; (ii)

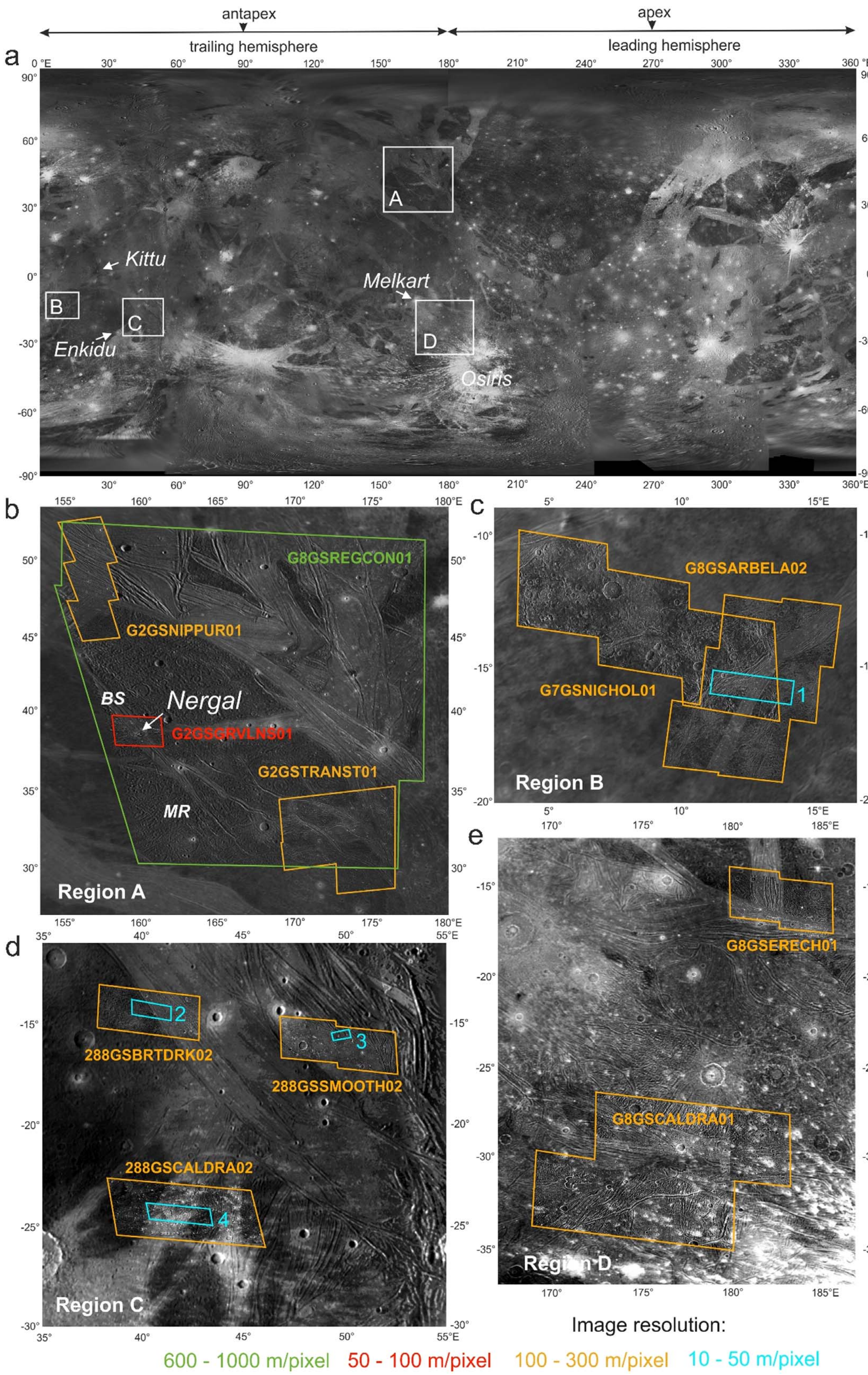

Figure 1. Overview of the studied regions: (a) global basemap of Ganymede (from Kersten et al. 2021) showing the location and distribution of the region of interests with subsets of each region such as (b) Region A—Byblus and Nippur Sulcus, (c) Region B—Arbela Sulcus, (d) Region C—Harpagia Sulcus, and (e) Region D—Mummu and Sippar Sulci and Erech Sulcus, with the frames indicating the areas observed by Galileo SSI (Table 1) at high resolution. The highest-resolution images indicated by numbers are (1) 28GSARBELA01 (34 m pixel^{-1}), (2) 28GSBRTDRK01 (20 m pixel^{-1}), (3) 28GSSMOOTH01 (16 m pixel^{-1}), and (4) 28GSCALDRA01 (43 m pixel^{-1}). For the location of the local features see Figures 5–21.

Table 1
Observational Parameters of the High-resolution Galileo SSI Observations Used in This Study, Including the Distances D_A in Degrees to the Apex Point of Ganymede's Orbital Motion (0° N, 270°E), Measured for the Center of the SSI Target Areas (see Appendix A.1.2.3)

Region	Sequences	No. of Images	Center Coordinate (Latitude, Longitude)	Apex Distance D_A (°)	Resolution (m pixel^{-1})	p/i/e	Covered Regions
A	G2GSNIPPUR01	3	49, 204	105.2	99	26/59/49	Nippur Sulcus in contact with Marius Regio
	G2GSGRLVNS01	2	40, 202	105.4	86	26/53/39	Byblus Sulcus within Marius Regio
	G2GSTRANST01	4	32, 188	95.5	188	30/39/34	Transitional terrains in contact with Marius Regio
	G8GSREGCON01	1	40, 193	(97.6; no counts)	936	62/79/44	Byblus Sulcus, Philus Sulcus, and transitional terrains in contact with Marius Regio
B	28GSARBELA02	6	−15, 347	101.5	133	28/37/11	Arbela Sulcus within Nicholson Regio
	G7GSNICHOL01	3	−13, 351	99.7	181	73/58/32	Nicholson Regio in contact with Arbela Sulcus
C	28GSBRTDRK02	2	−14, 337	129.5	121	24/63/39	Harpagia Sulcus in contact with Nicholson Regio
	28GSSMOOTH02	2	−16, 310	137.4	116	23/73/50	Harpagia Sulcus
	28GSCALDRA02	2	−24, 318	127.7	150	22/66/46	Harpagia Sulcus in contact with Nicholson Regio
D	G8GSERECH01	2	−16, 177	87.1	143	77/55/34	Erech and Sippar Sulcus in contact with Marius Regio
	G8GSCALDRA01	5	−31, 184	93.4	179	73/60/41	Mummu and Sippar Sulci

Note. Note that "p," "i," and "e" represent the phase, incidence, and emission angle of the corresponding observation sequence, respectively.

morphological surface characteristics, such as numbers and appearance of superimposed impact craters; (iii) the degree of erosion; and (iv) the occurrence of linear features, including their frequency and orientation, particularly in the light terrain. In order to be consistent with previous geologic mapping done for Ganymede, we followed the scheme and naming convention developed by Patterson et al. (2010) and Collins et al. (2013). This global geological map of Ganymede was produced directly from the digital image mosaic of the satellite's surface released by the USGS (Becker et al. 2001) with the included Galileo and Voyager images resampled at a resolution of 1 km pixel^{-1}. Since our study focuses on a more local scale, geologic units presented in the global map of Collins et al. (2013) were refined or additional subunits were added if necessary. The simple but powerful geological principle of superposition was used to derive details of the stratigraphic relationship between the mapped units. These data were compared with the results of the crater size–frequency measurements, which are described in Section 3.2.

According to Patterson et al. (2010) and Collins et al. (2013) the geological terrains in Ganymede are mainly divided into two broad categories: (1) the ancient, heavily cratered dark terrain (d) and (2) the less heavily cratered and thus presumably younger and strongly resurfaced light terrain (l). The dark terrain is classified as cratered (dc) and lineated (dl), whereas the light terrain is classified as grooved (lg), subdued (ls), and irregular (li). Reticulate terrain (r) appears to be transitional between dark terrain and light terrain. Terrain units whose morphological characteristics are unknown due to very low resolution are classified as undivided (Patterson et al. 2010). The term "sulcus" refers to a type of geological feature on Ganymede, a tectonic groove or furrow known as "sulci" in their plural form, and has been adopted as a designator by the IAU Planetary Nomenclature Committee.

Dark terrains are commonly seen as polygons with a distinct boundary, which are surrounded or cross-cut by the light terrains. They are always of low albedo due to surface ice contaminants, with the proportion of contaminants ranging from less than 10% (Clark 1980) to about 45% (Spencer 1987). Processes like tectonic deformation, cratering, sublimation, and mass wasting lead to local variations in albedo (Prockter et al. 1998; Moore et al. 1999). The terrain unit dl is inherently similar to dc except for the presence of straight, sinuous, or curvilinear lineaments or fractures. Like dc, it also has low albedo (Pappalardo et al. 2004).

About two thirds of Ganymede's surface area is covered by light terrain (Pappalardo et al. 2004). The light terrain contains a large number of parallel, subparallel, and curvilinear ridges and troughs, which extend for long distances (Shoemaker et al. 1982). Light grooved terrain (lg) has grooves that can form horst-and-graben-like structures, with their widths varying (e.g., Pappalardo et al. 2004). Grooves can be linear to curvilinear, equally to subequally spaced, parallel to subparallel in nature. Light subdued terrain (ls) is characterized by a moderate to high albedo and a smooth appearance, where grooves are mostly absent or not prominent enough to be characterized under lg. They are usually found associated with the light grooved and light irregular terrains. Satellite imagery with a high resolution of 10–50 m pixel^{-1}, however, shows that even this unit contains minor ridges and grooves. The light subdued terrain (ls) also shows caldera-like depressions that are interpreted as cryovolcanic features (Head et al. 1998; Kay & Head 1999; Spaun et al. 2001). However, the role of cryovolcanism and the formation of caldera-like features are not yet fully understood. Light irregular terrain (li) is characterized by irregularly spaced and oriented ridges and grooves, often seen as some portions of grooves and smooth regions within a single terrain unit. These terrains possess a moderate to high albedo and are usually found associated with lg and ls. These terrains are less common than other light terrains. Reticulate terrain is mesh-like in appearance, with many crisscross fractures or grooves, and is usually found adjacent to dark terrain. However, the grooves are not well developed. It has been suggested that block rotations within shear zones led to the formation of reticulate terrains (Murchie & Head 1988). Each of these light terrain units are further classified into three main categories based on the principle of cross-cutting relationships. Category 1 (lg_1, ls_1, and li_1) contains light terrain units which are cross-cut by all other light terrain units. Category 3 (lg_3, lg_3, and li_3) contains those light terrain units which cross-cut all adjacent light terrains. Category 2 (lg_2, ls_2, and li_2) contains those light terrain units which cross-cut Category 1 units and, in turn, are cross-cut by Category 3 units (Patterson et al. 2010).

3.2. Crater Size–Frequency Measurements

3.2.1. Size–Frequency Distributions of Impact Craters and Surface Ages

Crater size–frequency distributions (henceforth abbreviated CSFDs, or crater SFDs) are used to determine the relative ages of geological units. Deriving surface ages from crater SFDs superimposed on geologic units is based on the correlation between the frequency (or density) of impact craters and time: the higher the frequency of craters, the older the surface (e.g., Öpik 1960; Chapman & McKinnon 1986; Neukum & Ivanov 1994; Neukum et al. 2001; Werner & Ivanov 2015). Therefore, differences in crater frequencies generally reflect differences in the relative ages of surface units.

The absolute ages of surface units are obtained by using the two currently available impact chronology models. Both are subject to high degrees of uncertainties. Nevertheless, we will use such models in this study to compare and discuss the derived absolute ages and their uncertainties, as described in the following subsections, with respect to possible implications of geologic activities on Ganymede in the past. We introduce here the basics of how CSFDs are measured and used for extracting relative and absolute surface ages. A more thorough description of the methodology and the procedure of deriving ages from crater counts is described in Appendix A.1.

3.2.2. Crater Production Function

In our study, we prefer to use the cumulative CSFD when plotting crater counts. In the ideal case, a crater SFD represents an image of the SFD of the members of a projectile family impacting a surface over time. In this case a CSFD is termed a production distribution; a crater formed by the impact of an external projectile is termed a primary crater (e.g., Neukum & Ivanov 1994; Werner & Ivanov 2015). Numerous studies on lunar, terrestrial planet, or asteroid surface units and also on the icy satellites of Jupiter have shown that the CSFDs on these bodies can be approximated by a (body-specific) production function (henceforth abbreviated as PF)—representing the production distribution of craters—as a polynomial of at least

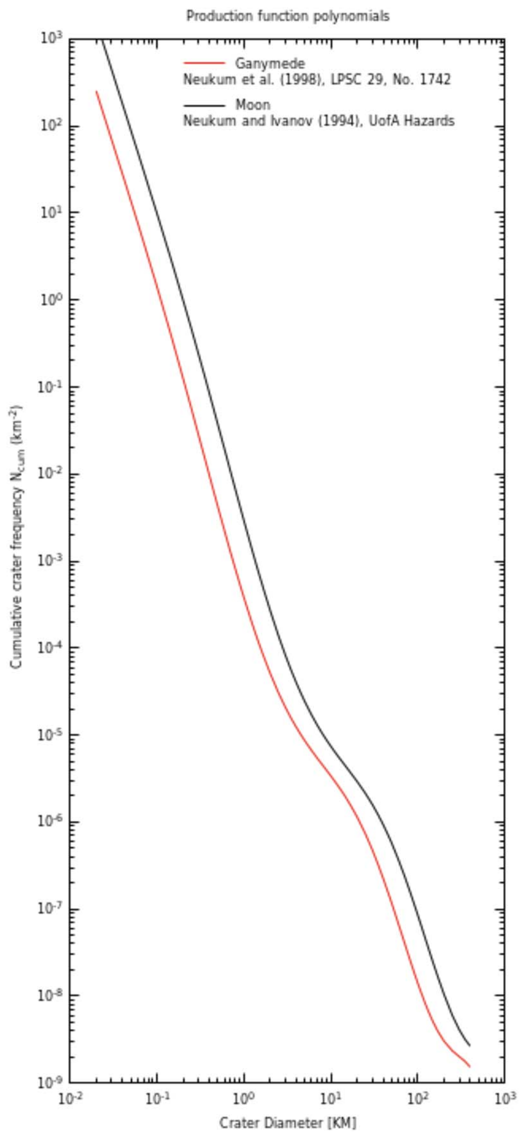

Figure 2. The PF polynomial of eleventh degree for Ganymede (Neukum et al. 1998; red), compared to the lunar PF (Neukum & Ivanov 1994; black) shown in a cumulative CSFD diagram.

tenth or eleventh degree from the smallest measurable crater diameter (meters or tens of meters) to the largest diameter (impact basins of several hundreds of kilometers; e.g., Neukum & Ivanov 1994; Neukum et al. 1998, 2001; Werner & Ivanov 2015; Hiesinger et al. 2016). The lunar PF polynomial is shown in Figure 2 (black curve).

Based on their CSFD measurements from Voyager images and, later, from Galileo SSI images, Neukum et al. (1998 and references therein) found a remarkable similarity between, e.g., lunar CSFDs and those from the icy Galilean satellites of Jupiter. Therefore, they derived a Ganymede-specific PF by shifting the lunar PF laterally in log(D) (see Appendix A.1.1). This PF derived for Ganymede is shown in comparison with the lunar PF in Figure 2 (red curve). Coefficients of the lunar and Ganymede PFs are listed in Table A1 in Appendix A.1.1.

3.2.3. Processes Affecting and Changing the Production CSFDs

In many cases the CSFDs are no longer pristine production distributions, but were subject to several processes affecting their shapes, which have to be considered in interpreting CSFD measurements. Among these are (a) saturation/equilibrium, (b) secondary craters and/or other sources, and (c) geologic processes. We briefly discuss these potential influences on our measurements, but we emphasize that these issues are still being intensely debated and are not fully solved. Also, a thorough discussion of crater scaling laws that link the size (or mass) of an impactor to the size of the crater it forms via specific impact conditions is beyond the scope of this paper (see, e.g., Werner & Ivanov 2015 as a reference).

3.2.3.1. Saturation/Equilibrium versus Production Distributions

If a surface is impacted long enough that each newly formed crater obliterates preexisting craters the CSFD is termed to have reached saturation or equilibrium (e.g., Woronow 1978; Hartmann 1984; Chapman & McKinnon 1986; Neukum & Ivanov 1994; Richardson 2009; Werner & Ivanov 2015). Saturation/equilibrium is represented by a straight line with a cumulative slope of −2, which is achieved for CSFDs with slopes of −3 or steeper reaching equilibrium if subsequent impacts of small craters erase preexisting ones (e.g., Chapman & McKinnon 1986; Neukum & Ivanov 1994).

There is no consensus whether the most densely cratered regions such as, e.g., the lunar highlands, show equilibrium CSFDs (e.g., Richardson 2009) or not (e.g., Neukum & Ivanov 1994). As shown in Figure 3, we found that the CSFDs measured in both light and dark terrains on Ganymede in general are lower than a saturation/equilibrium distribution and therefore represent production distributions down to ∼500 m crater diameter in the examples shown in the graph.

3.2.3.2. Secondary and Sesquinary Craters

Blocky material, which is ejected when a primary crater is formed, creates smaller satellite craters around the primary, termed secondary craters (e.g., Werner & Ivanov 2015 and references therein). These craters are different in morphology than primaries, characterized by less pronounced crater rims and more shallow floors, by more irregularly shaped rims, and by their occurrence in clusters or rays pointing radially away from the center of the primary (see Figure 15(a) for an example of suspected secondary craters). They generally form at lower velocities than primary craters. Secondary craters can also form at great distances from their parent crater by blocks ejected at high velocities close to the impact contact point, and thus they resemble primary craters, making them indistinguishable from each other (e.g., Bierhaus et al. 2005). It has been suggested that small craters (several kilometers and smaller) are predominantly of secondary origin and, therefore, are practically useless for dating surfaces at these crater sizes (e.g., McEwen et al. 2005). However, this issue is still under discussion.

Small craters on the Jovian satellites (and on other satellites in the outer solar system) could be almost exclusively of secondary origin if these bodies are mainly bombarded by projectiles derived from the Kuiper Belt, e.g., by ecliptic comets (ECs) since this impactor family is characterized by a deficit of small bodies (e.g., Dones et al. 2009; Kirchoff et al. 2018; Singer et al. 2019; Kirchoff et al. 2022). Such a scenario has been inferred by Bierhaus et al. (2001) for Europa, but a more recent work (Bierhaus et al. 2018) showed that local,

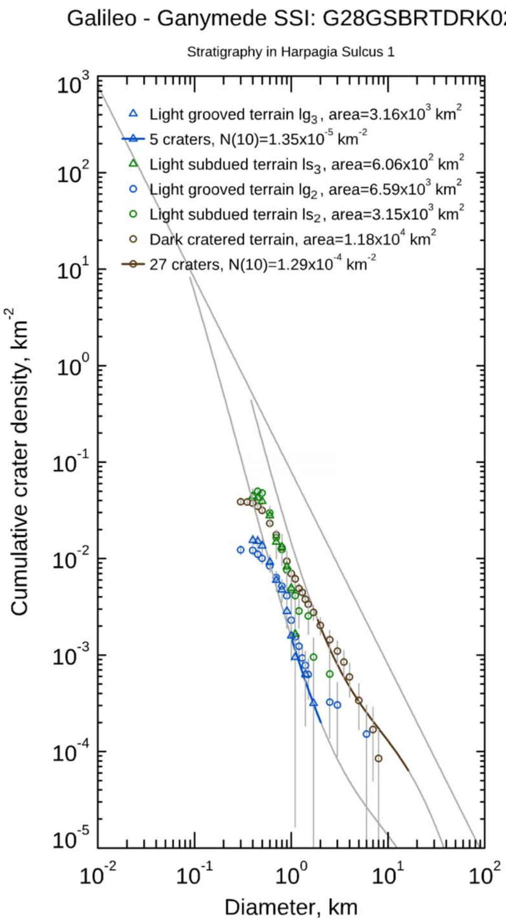

Figure 3. CSFDs measured in several light terrain units and in dark terrain (Galileo SSI target area 28GSBRTDRK02) with the Ganymede PF (Neukum et al. 1998) fitted to the data, and the equilibrium distribution with a cumulative slope of −2 (Neukum & Ivanov 1994). The graph demonstrates that the CSFDs on Ganymede are well below saturation/equilibrium for small craters down to ∼500 m diameter even in the old dark densely cratered terrains. See the text for further explanation.

target-specific effects of primary versus secondary cratering have to be considered on these satellites.

Material can be ejected and accelerated beyond the escape velocity of the satellite, impacting another satellites in the system, or even the satellite of origin again. This type of craters is termed sesquinary (e.g., Alvarellos et al. 2002; Zahnle et al. 2008). Sesquinary craters and/or long-traveling secondaries smaller than ∼2 km are practically indistinguishable from primary craters and may contribute to a measured CSFD with some uncertainty for craters smaller than this size (e.g., Singer et al. 2013; Kirchoff et al. 2022).

For measurements closely to or within the strewn field of a larger crater we tried to avoid measuring potential secondaries based on their morphological characteristics described above. However, it cannot be completely guaranteed that such secondaries, with these typical morphological characteristics, were excluded in our measurements, especially near primary craters with strewn fields of several 100s or 1000s of kilometers.

3.2.3.3. Geologic Resurfacing Processes

Erosion through micrometeoritic bombardment and sublimation, flooding with liquid material, or tectonic events tend to obliterate or completely erase especially smaller craters below a threshold diameter (e.g., Prockter et al. 1998; Moore et al. 1999; Werner & Ivanov 2015). Below this threshold diameter the slope of the CSFD becomes characteristically flatter in a cumulative crater frequency diagram. When this geologic process comes to an end, the surface becomes recratered with a steeper cumulative slope and remains undisturbed unless further geologic processes become active at later times. Such resurfacing events can be identified and even be dated in measured CSFDs (Michael & Neukum 2010). Indeed, resurfacing events have been documented on various celestial bodies, including the Moon, where early studies on resurfacing events in relation to CSFDs were conducted by Neukum & Horn (1976). These events play a significant role on Ganymede.

Previous measurements of impact craters in Ganymede's dark terrain have also revealed that viscous relaxation could have a major effect on impact degradation (Bland et al. 2017), providing a window into Ganymede's thermal history. However, since mainly the depths of the majority of impact craters are reduced, this process is not expected to have a major influence on the CSFD measurements. The complete relaxation of small craters (<4 km diameter) requires high heat fluxes (150 mW m^{-2}) over long timescales (∼1 Gyr) and is difficult to explain by viscous relaxation alone and thus requires an alternative explanation (Bland et al. 2017) such as the resurfacing processes mentioned above.

3.2.4. Absolute Ages Based on Impact Chronology Models

In order to reconstruct the geologic history of a planetary surface, crater frequencies representing the relative ages of surface units can be used to derive the absolute ages for these units. Since no radiometric ages of surface materials are available except for the Moon, this can only be done by impact chronology models, based on impact rates of the members of a dominating projectile family. Due to this model dependence of absolute ages from CSFD measurements, the term absolute model age (AMA) is commonly used (see, e.g., Hiesinger et al. 2016). Despite the high uncertainties associated with such models, we concentrate in our study on relative ages when discussing the stratigraphic relationships of the mapped surface units (Section 4). Since, however, absolute ages are essential to shed light on the potential timescales of Ganymede's geologic and tectonic activity, we also derived and discussed their absolute ages of using both models (Section 5).

The SFDs of craters described by a body-specific crater PF reflects the SFD of projectiles creating craters in a given time (e.g., Chapman & McKinnon 1986; Neukum & Ivanov 1994; Werner & Ivanov 2015 and references therein). The SFDs of craters also reflect the rheological properties of the surface (e.g., Massironi et al. 2009; Le Feuvre & Wieczorek 2011; Marchi et al. 2011). Craters are formed by members of distinct impactor families; on the terrestrial planets and asteroids in the inner solar system, craters were, and are at present, mainly created by impacts of Main Belt asteroids (MBAs), or from near-Earth objects (NEOs), with a contribution of comets being on the order of less than 10% (e.g., Neukum & Ivanov 1994; Neukum et al. 2001; Bottke et al. 2002; Strom et al. 2005; Marchi et al. 2009). For planets and icy satellites in the outer solar system, several potential impactor families are inferable (Shoemaker & Wolfe 1982; Chapman & McKinnon 1986; Neukum et al. 1998; Zahnle et al. 1998, 2003; Schenk et al. 2004; Dones et al. 2009; Werner & Ivanov 2015; Kirchoff et al. 2018; Singer et al. 2019): (a) MBAs, (b) short-period ECs and

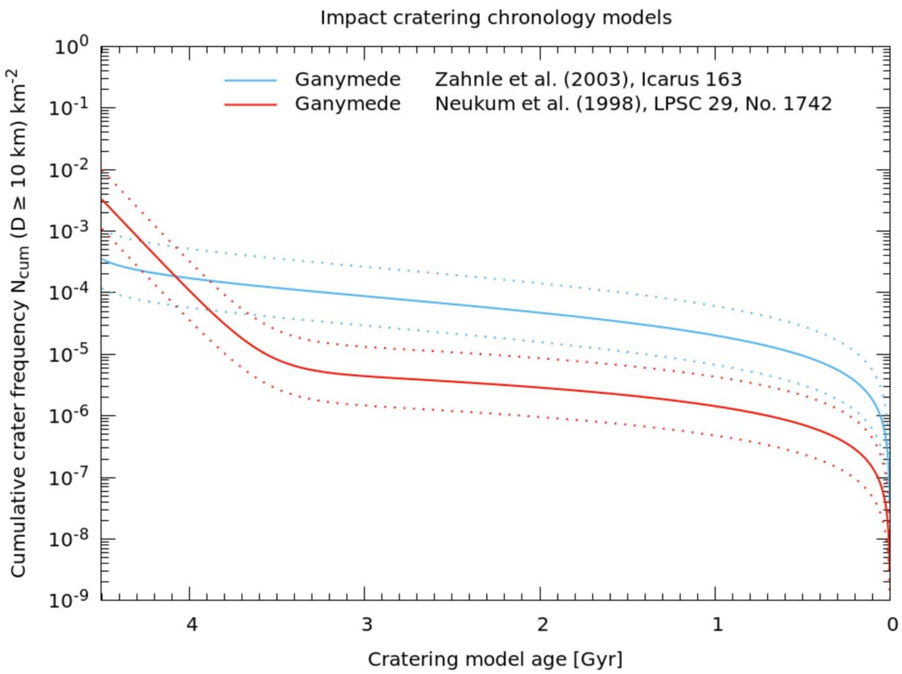

Figure 4. Comparison of the impact chronology models by Zahnle et al. (2003; JCM, blue) and Neukum et al. (1998; LDM, red) for a cumulative crater frequency N_{cum} ($D \geqslant 10$ km). Also shown are the lower and upper model uncertainties (dotted curves; see the text in this section and Section 3.2.5). For the parameters (coefficients) and cratering rates of the two model functions we refer to Neukum et al. (1998), Zahnle et al. (2003), and to Appendix A.1.2.1.

Centaurs from the Kuiper Belt, (c) long-period, nearly isotropic comets (NICs) from the Oort cloud, (d) Trojans librating around the L4 and L5 Lagrangian points of Jupiter and Neptune, (e) irregular satellites, and (f) planetocentric material. The major source of impactors has strong implications on the absolute timescales in cratering these surfaces.

Currently, there are two available chronology models for the satellites of Jupiter, which were developed at the time of the early Voyager (late 1970s) and Galileo missions (late 1990s). The lunar-derived model (Neukum et al. 1998), henceforth abbreviated as LDM, is based on the similarities of lunar CSFDs and those on the Galilean satellites, assuming preferential impacts of MBAs on the Galilean satellites with a similar time dependence of crater frequency as in the case of the moon, as Neukum et al. (1998; and references therein) concluded. In this model, the impact rate drops exponentially but smoothly from ∼4.3 Ga ago and becomes more or less constant since ∼3–3.3 Ga until the present (Figure 4).

The second chronology model for the Jovian satellites is based on the predominant impacts of ECs or Jupiter-family comets (JFCs), henceforth termed JCM. By observing such Jupiter-crossing bodies, Shoemaker et al. (1986) and later Zahnle et al. (1998, 2003) derived an impact chronology for each satellite with a more or less constant cratering rate from the present time back to ∼4 Ga. Prior to ∼4 Ga, the cratering rate is assumed to increase exponentially due to a $\sim 1/t$ depletion of impactors leaking from the Kuiper Belt with time (t; see the discussion in Zahnle et al. 1998).

Impacts from NICs from the Oort cloud occur much less often than do impactors from ECs (Zahnle et al. 1998). In this study we use the JCM with cratering rates for ECs by Zahnle et al. (2003) with updated cratering rates with respect to Zahnle et al. (1998; Figure 4).

According to Zahnle et al. (2003), the SFD of JFCs for projectiles smaller than 20 km is derived from the crater SFD on Europa, young basins on Ganymede and Callisto, and Triton. In contrast, the SFD of projectiles larger than 50 km is derived from observed Kuiper Belt bodies. To bridge the gap between 20 and 50 km, Zahnle et al. (2003) use interpolation. It is evident that an impactor with a diameter of 20 km creates a crater on Ganymede with a diameter of at least 200–300 km for heliocentric impact velocities. Consequently, Zahnle et al. (2003) infer the impactor SFD from the CSFD for craters with diameters up to 200–300 km, similarly to our approach, but they use a diameter-dependent power-law distribution instead of an eleventh-degree polynomial.

The similarity between CSFDs measured on the surfaces of the moon and of, e.g., Ganymede, reported by Neukum et al. (1998), was never unequivocally explained by them—unless under the premise of mainly asteroidal impacts. Collisional evolution for nonasteroidal impactors dominating the bombardment of the Galilean satellites producing CSFD shapes similar to lunar CSFDs has been suggested (e.g., Wagner et al. 2017). Bottke et al. (2022), eventually, concluded recently that these similarities really exist and are indeed based on the collisional evolution of comets or other potential outer solar system impactors. Therefore, a lunar-derived Ganymede PF can be used to fit CSFDs measured on Ganymede and to derive AMAs from both models, despite different origins of impactors.

The graphs of the two concurring model chronology functions by Neukum et al. (1998; LDM) and Zahnle et al. (2003; JCM) are shown in Figure 4. We also included the upper and lower uncertainties of the chronology function graphs (dotted curves). For the JCM, Zahnle and colleagues assume an uncertainty of a factor of 2 in the cratering rate (Zahnle et al. 2003). In the LDM an uncertainty in cratering rate was not specifically given by Neukum et al. (1998). However, studies involving lunar-like chronologies in the inner solar system imply average uncertainties of at least factors of 2–3 (e.g., Neukum et al. 2001) similar to the case of the JCM, therefore we chose the same uncertainty factor of 3 for the LDM too (see the more detailed description in Section 3.2.5). The procedure of how AMAs for both chronology models are obtained is described in more detail in Appendix A.1.2.1.

The relative ages and AMAs from a CSFD measurement are obtained either by a least-squares fit of the Ganymede PF to the crater statistics data, or by a procedure termed Poisson timing analysis (PTA) (Michael et al. 2016). In this latter improved approach, an impact chronology model is exactly evaluated on the basis of Poisson statistics and a likelihood with an intrinsic uncertainty. The advantage of this procedure over a least-squares fit is that it is also applicable to a surface with no superimposed craters at all, which allows one to estimate the maximum age of a surface by considering the measurement area and the image resolution. For such cases, we assumed the existence of at least one crater with a (bin) diameter (in kilometers) beneath a factor of three times the image resolution (in kilometers per pixel). This procedure has been proven to be useful for the estimation of ages especially of those stratigraphically young craters which, at a given image resolution, are devoid of superimposed craters (e.g., Wagner et al. 2010, 2018, 2019). Therefore, the PTA approach is used for fitting CSFD measurements in our study.

3.2.5. Uncertainties in the Relative Ages and AMAs

The uncertainties in our CSFD measurements and derived AMAs are derived following the recommendations in Arvidson et al. (1979), Zahnle et al. (2003), Michael et al. (2016), and Robbins et al. (2018). If the formation of craters on a surface with area A (square kilometers) is assumed to have a Poisson distributed, the uncertainty, or the confidence interval, for n craters equal to, or larger than diameter D in a cumulative distribution is log $[(n \pm \sqrt{n})/A]$ (Arvidson et al. 1979). In general, as implemented in the craterstats 2.0 software package (see Appendix A.1.2.1), measured crater diameters are binned using 18 bin diameters in each decade (semilogarithmic binning; e.g., Neukum & Ivanov 1994), and confidence intervals are calculated and plotted accordingly (Arvidson et al. 1979). Despite being recommended by Arvidson et al. (1979), we do not use a bin width of $\sqrt{2}$ km crater diameters, which is comparably coarse, but prefer the finer semilogarithmic binning instead, similar to studies discussed by others (e.g., Hiesinger et al. 2000; Schenk et al. 2004; Werner & Ivanov 2015).

The error handling of both crater frequencies for a reference crater diameter and associated AMAs in the craterstats 2.0 software tool is currently being reworked, expanded, and improved (G. Michael, personal communication). Therefore, we had to use work-arounds using our own software tools to present the uncertainties for the surface ages and/or to calculate AMAs for the JCM chronology.

Using the PTA approach described above (Michael et al. 2016), an LDM AMA and an associated cumulative frequency for craters $\geqslant$1 (or 10) km is obtained, along with upper and lower uncertainty frequencies. These uncertainties in the cumulative frequency are shown in plots of relative ages (Figure 23). However, this procedure does not consider that the chronology has a substantial additional uncertainty in the cratering rate, assumed to be a factor of ∼2–3, as shown in Figure 4 (Section 3.2.4). The total uncertainty in the LDM AMA is therefore higher than from the application of the PTA alone, on the order of ±100–200 Ma for ages older than ∼3.5 Ga and up to ∼±1 Ga for ages younger than ∼3–3.3 Ga.

For JCM AMAs, the upper and lower uncertainties are calculated from the factor of 3 in the cratering rate for ECs (Zahnle et al. 2003), holding the cumulative frequency fixed. Due to the low constant cratering rate, these uncertainties in the AMA are high, approximately ±0.5–1 Ga. The calculation of the (generally smaller) upper and lower uncertainties of the JCM AMA from the uncertainty in the cumulative frequency was not carried out in this study. An implementation to consider the total uncertainty in the craterstats 2.0 tool is in development (G. Michael, personal communication). Despite the high uncertainties in both chronology models, we chose to use two significant figures in the AMA (refer to Tables 2 through 10) since the units of different ages can be distinguished in cumulative frequencies, and increasing or decreasing trends in ages are inferable (see, e.g., Figure 23).

4. Mapping Results

4.1. Region A: Byblus and Nippur and Philus Sulci and Transitional Terrain (G8GSREGCON01)

Region A offers a detailed look into the light terrain units of Byblus Sulcus, Nippur, and Philus Sulci and the transitional terrain between Marius Regio and Nippur Sulcus, which surrounds and intersects the extended dark terrain of Marius Regio (Figures 1(b), 5, 7, and 9). The light terrain units comprise grooves/fractures, narrow bands, and extensively resurfaced complex networks. Byblus (Figure 5(a)) and Nippur Sulcus (Figure 7(a)) exhibit a northwest–southeast orientation (Head et al. 1997). Akitu Sulcus connects these two sulci and has an east–west orientation. The Galileo SSI observation sequence G2GSNIPPUR01 (Figure 7) covers portions of Nippur and Philus Sulci that lie approximately 200 km north of the Byblus Sulcus region (G2GSGRVLNS01, Figure 5). The transitional terrain (G2GSTRANST01, Figure 9) lies approximately 400 km southeast of Byblus Sulcus. The extended portion of Nippur Sulcus and Byblus Sulcus toward its south can be considered as part of transitional terrain.

4.1.1. Byblus Sulcus (G2GSGRVLNS01)

i. Geological Mapping

Byblus Sulcus is a narrow band of light terrain located at ∼40°N/160°E trending in the northwest–southeast direction and intersecting the adjacent dark terrain of Marius Regio. The mosaic of two Galileo SSI images of G2GSGRVLNS01 having 86 m pixel^{-1} resolution is used for detailed mapping and CSFD estimation (Figure 5(a)). The geologic units that could be distinguished in this image include two impact craters (c), light grooved terrain lg_3, light subdued terrain ls_3, light grooved terrain lg_2, furrows (F) and dark cratered terrain (dc; Figure 5(b)). From the cross-cutting relationship, lg_3 and ls_3 cross-cut all adjacent terrains and are consequently the youngest terrains. The terrain unit dc is cross-cut by all other light terrains and is the oldest terrain.

The youngest features observed in this region are two morphologically fresh impact craters (possibly the result of a double impact) with the larger one, called Nergal (∼8 km diameter), showing a dark halo of about one crater radius extent that is surrounded by light ejecta. These craters are located in the center of Byblus Sulcus and are superimposed on the youngest light grooved terrain lg_3. The light terrain of Byblus

Table 2
Measured CSFDs (Cumulative Frequencies for 10 km (*N* (10)) and 1 km (*N* (1)) Craters) for All Mapped Terrain Units in the Byblus Sulcus Region, Including LDM and JCM Age Estimates, Terrain Unit Areas, and the Number of Craters Counted

Region A	Terrain Unit	*N* (10) (km^{-2})	*N* (1) (km^{-2})	LDM (Ga)	JCM (Ga)	Area (km^2)	No. of Craters Counted
G2GSGRLVNS01 (Byblus Sulcus)	lg_3	$2.61 \times 10^{-5} \pm 5.38 \times 10^{-6}$	$2.94 \times 10^{-3} \pm 6.06 \times 10^{-4}$	$3.77^{+0.038}_{-0.044}$	$1.25^{+1.57}_{-0.79}$	4027.26	156
	ls_3	$3.95 \times 10^{-5} \pm 1.95 \times 10^{-5}$	$4.45 \times 10^{-3} \pm 2.20 \times 10^{-3}$	$3.83^{+0.083}_{-0.12}$	$1.62^{+1.72}_{-1.0}$	209.806	20
	lg_2	$3.11 \times 10^{-5} \pm 1.03 \times 10^{-5}$	$3.51 \times 10^{-3} \pm 1.16 \times 10^{-3}$	$3.80^{+0.055}_{-0.067}$	$1.41^{+1.65}_{-0.88}$	1223.04	9
	dc	$9.89 \times 10^{-5} \pm 1.67 \times 10^{-4}$, $3.38 \times 10^{-4} \pm 1.18 \times 10^{-4}$	$1.11 \times 10^{-2} \pm 1.88 \times 10^{-2}$, $3.81 \times 10^{-2} \pm 1.33 \times 10^{-2}$	$3.99^{+0.024}_{-0.029}$ $4.17^{+0.057}_{-0.066}$	$3.28^{+1.18}_{-1.71}$ $4.46^{+0.1}_{-1.16}$	4064.55	324

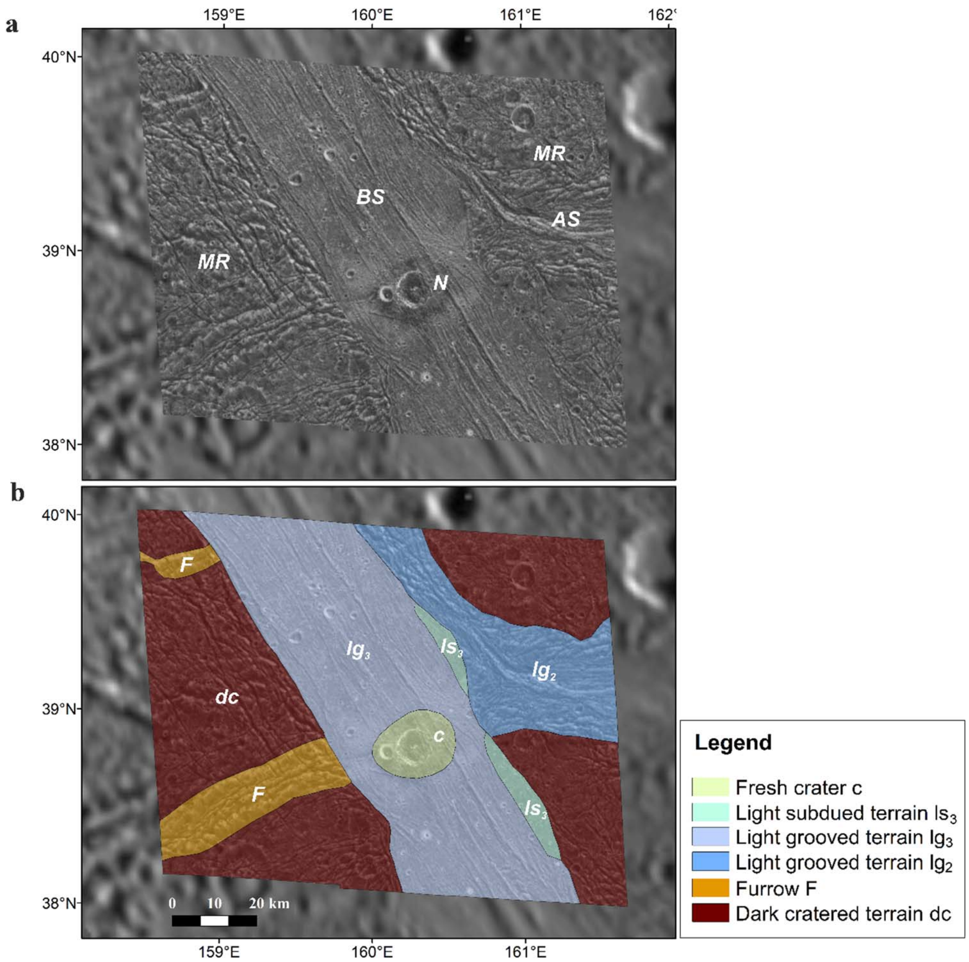

Figure 5. Region A/Byblus Sulcus: (a) SSI observation G2GSGRVLNS01 with the location of Byblus (BS) and Akitu Sulcus (AS), Marius Regio (MR), and impact crater Nergal (N) indicated and (b) the associated geologic map produced following the mapping style of Collins et al. (2013).

Sulcus, in general, shows a parallel and regular array of grooves in its middle part and more irregular grooves adjacent to it. The contact toward dark terrain on the western side is sharp whereas on the eastern side the grooves disappear gradually and two ls_3 terrains are present.

The light subdued terrains ls_3 are very smooth and show only a few indistinct grooves. This terrain has a sharp border separating dc and lg_2, but separation from lg_3 does not show any sharp trough. The light grooved terrain lg_2 is characterized by the presence of a sigmoidally shaped large ridge in the middle part, which has a high albedo and is surrounded by a number of short grooves which are trending obliquely to the main ridge. The dark cratered terrain dc is the oldest unit in G2GSGRVLNS01 (Figure 5). It is not only densely cratered but also highly fractured. Northeast–southwest trending furrows (F) are common geomorphological features in dc. Fractures in between the furrow sets and on either side of lg_2 either run parallel to the trend of lg_3 (northwest–southeast) and seem to be related to the formation of the lg_3 light terrain, or they trend perpendicular to this direction. The furrows usually occur in sets (Smith et al. 1979a, 1979b). The most striking feature of the entire area is the bent Akitu Sulcus with a sigmoidal ridge at its center, mapped as lg_2. This unit suggests that dextral strike-slip may have occurred along the northwest–southeast direction, which was later formed by the lg_3 and ls_3 units. This suspected shearing led to drag folding of unit lg_2 (Cameron et al. 2018).

ii. CSFDs

The youngest terrains in Byblus Sulcus (Figure 5), based on mapping, ls_3 and lg_3, have CSFDs of $3.95 \times 10^{-5} \pm 1.95 \times 10^{-5}$ km^{-2} and $2.61 \times 10^{-5} \pm 5.38 \times 10^{-6}$ km^{-2} (Table 2). Note that in the following we use N (10) values as a CSFD. Since they do not have considerable variation in their CSFD and no clear borders separating these terrains both seem to be cogenetic (Figure 6). The second youngest terrain known from mapping results, lg_2, has a CSFD of $3.11 \times 10^{-5} \pm 1.03 \times 10^{-5}$ km^{-2}, which is in the range of ls_3 and lg_3. This suggests that the relative chronology is constrained solely by cross-cutting relationships, as the crater-counting technique alone cannot distinguish between these units. The similar CSFDs of ls_3, lg_3, and lg_2 imply similar ages and a formation in a short period. The relatively low number of craters on lg_2 may indicate some resurfacing activity.

Terrain unit dc has the highest CSFD among all mapped terrain units, consistent with our mapping results. Two possible CSFDs are identified as $9.89 \times 10^{-5} \pm 1.67 \times 10^{-4}$ km^{-2} and $3.38 \times 10^{-4} \pm 1.18 \times 10^{-4}$ km^{-2}. The lower CSFD indicates resurfacing activity which could have erased some craters.

4.1.2. *Nippur and Philus Sulcus (G2GSNIPPUR01)*

i. Geological Mapping

Nippur and Philus Sulcus represent extended areas of intense resurfacing. Both sulci surround Marius Regio in the north and

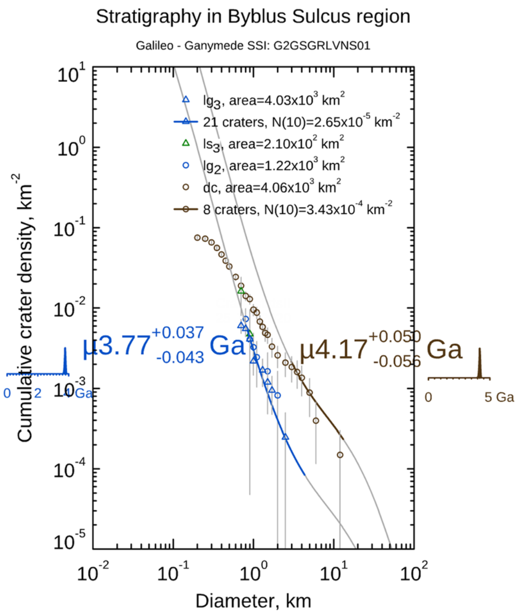

Figure 6. Comparison of the relative ages of different terrain units in Byblus Sulcus (SSI observation G2GSGRVLNS01) based on CSFDs. The plot displayed here represents ages derived from LDM. For ages based on JCM, refer to Table 2.

east (Figure 7(a)). Nippur Sulcus has an overall trend in the northwest–southeast direction while Philus Sulcus has a trend in the northeast–southwest direction. The Galileo SSI observation sequence G2GSNIPPUR01 comprising three images with a spatial resolution of 99 m pixel^{-1} is used for detailed mapping and CSFD measurements. The geology in this region includes various light terrain units of different ages and minor dark terrain (Figure 7(b)). Among these, ls_3, lg_2, and lg_1 build Nippur Sulcus, and lg_2 (2), ls_2, and li_1 form Philus Sulcus. In general, Nippur Sulcus is younger as it cross-cuts Philus Sulcus. From the cross-cutting relationships, the smooth light unit ls_3 is the youngest terrain unit.

The subdued terrain ls_3 is a narrow band ∼15 km wide of northwest–southeast trending smooth terrain. It has two sharp ridges and a trough at the border to the adjacent terrains on its either side. Subdued lineaments mostly trend parallel to the borders. The light grooved terrain lg_2 is a broad band of ∼144 km wide northwest–southeast trending grooved terrain with ridges and graben-like depressions. Its contact with ls_3 is long and sharp while its contact with lg_1 consists of many short curvilinear lineaments. The unit contains densely packed linear to sigmoidal-shaped ridges. The spindle-like arrangement of the ridges leads to frequent low-angle unconformities with adjacent straight lineaments.

The light grooved terrain lg_1 is the oldest one among the light terrains of Nippur Sulcus. Unlike ls_3 and lg_2 terrain units, its lineaments trend in the west–east direction and are parallel to subparallel to each other. The lineaments are not strongly grooved as the lineaments of lg_2. The average spacing between the ridges is less than 1 km. It has a 7 km diameter crater located in the center. The contact to lg_2 is a sudden high-angle unconformity with parallel fractures.

The terrain units lg_2 (2), ls_2, and li_1 of Philus Sulcus follow a northeast–southwest trend perpendicular to the orientation of ls_3 and lg_2. Thus, Nippur Sulcus (ls_3) sharply truncates these units. The lineaments of lg_2 (2) are equally spaced, parallel to subparallel to each other and also to its borders. There are some younger fractures that cut the lineaments of lg_2 (2) and reach into ls_2, and further east into the dark terrain. The unit ls_2 appears somewhat smoother, but generally gradational transitions occur here between lg_2 (2), ls_2, and li_1. We mapped a region of light irregular terrain li_1 as it appears more rugged than the surrounding terrain. It appears that the li_1 terrain is being resurfaced by ls_2 and the trend of the lineaments in li_1 and ls_2 are different. The li_1 terrain comprises many closed-spaced minor ridges at low angle to the general trending, but most of them are destroyed by smaller craters.

The dark cratered terrain dc has an overall rugged topography with many dominating north–south trending fractures. Sharp grooves separate dc from lg_2. The terrain is more fractured than cratered. An unnamed crater is strongly strained to an ellipse with an aspect ratio of ∼2, with the long axis in the north–south direction.

Mapping of Nippur and Philus Sulci indicates that the relatively smooth terrain ls_3 formed latest. The previously formed wrinkly lg_2 unit with sigmoidal-shaped ridges suggests a contribution of strike-slip tectonics active at the time of formation. We also observed that a small section of the exposed dark terrain has experienced significant tectonic deformation, as evidenced by the strained crater (Pappalardo & Collins 2005; Cameron et al. 2018).

ii. CSFDs

At Nippur Sulcus (Figure 7), lg_1, has a CSFD of $6.44 \times 10^{-5} \pm 5.48 \times 10^{-6}$ km^{-2} followed by lg_2 having a a CSFD of $5.54 \times 10^{-5} \pm 3.01 \times 10^{-6}$ km^{-2} and ls_3 with a CSFD of $4.44 \times 10^{-5} \pm 4.26 \times 10^{-6}$ km^{-2} (Table 3). Although the cross-cutting relationship infers that lg_2 is older than ls_3, the intervals for CSFD values of lg_2 and ls_3 overlap. However, for lg_1, there are large error bars. At Philus Sulcus, li_1 has a CSFD of $3.34 \times 10^{-5} \pm 4.79 \times 10^{-6}$ km^{-2}, which is slightly older than that of ls_2 ($2.05 \times 10^{-5} \pm 2.13 \times 10^{-6}$ km^{-2}) and lg_2 (2) ($1.64 \times 10^{-5} \pm 3.61 \times 10^{-6}$ km^{-2}), respectively.

The relative age between Nippur Sulcus and Philus Sulcus remains unclear because the ls_3, lg_2, and lg_1 terrain units of Nippur Sulcus shows higher CSFDs than the li_1, ls_2, and lg_2 (2) terrain units of Philus Sulcus. This is in contrast to the cross-cutting relationship, where Nippur Sulcus cross-cuts Philus Sulcus. Nevertheless, from our crater-counting results, we found that the oldest terrain in overall Nippur and Philus Sulcus region is lg_1 (Figure 8). Terrain unit dc has a CSFD of $4.14 \times 10^{-5} \pm 1.98 \times 10^{-6}$ km^{-2}, lower than those of lg_2 and lg_1, which is also in discrepancy with the mapping.

Possible reasons for the lower CSFD of Philus Sulcus compared to Nippur Sulcus may be due to more intense tectonic deformation or resurfacing activities in these regions, or a counting bias. The relatively low CSFD obtained for the dark terrain is an effect of intense fracturing and deformation obliterating preexisting craters. Evidence for this is the presence of deformed ridges and a large strained crater.

4.1.3. Transitional Terrain (G2GSTRANST01)

i. Geological Mapping

Light terrain units that extend from Nippur Sulcus into Marius Regio comprise the so-called "transitional terrain" observed during the G2GSTRANST01 SSI observation sequence (Figures 1(b) and 9). The Galileo SSI images having ∼188 m pixel^{-1} resolution are used for this study area (Figure 9(a)). Overall, the light terrains and the fractures within the dark terrain dc trend in the northwest–southeast direction.

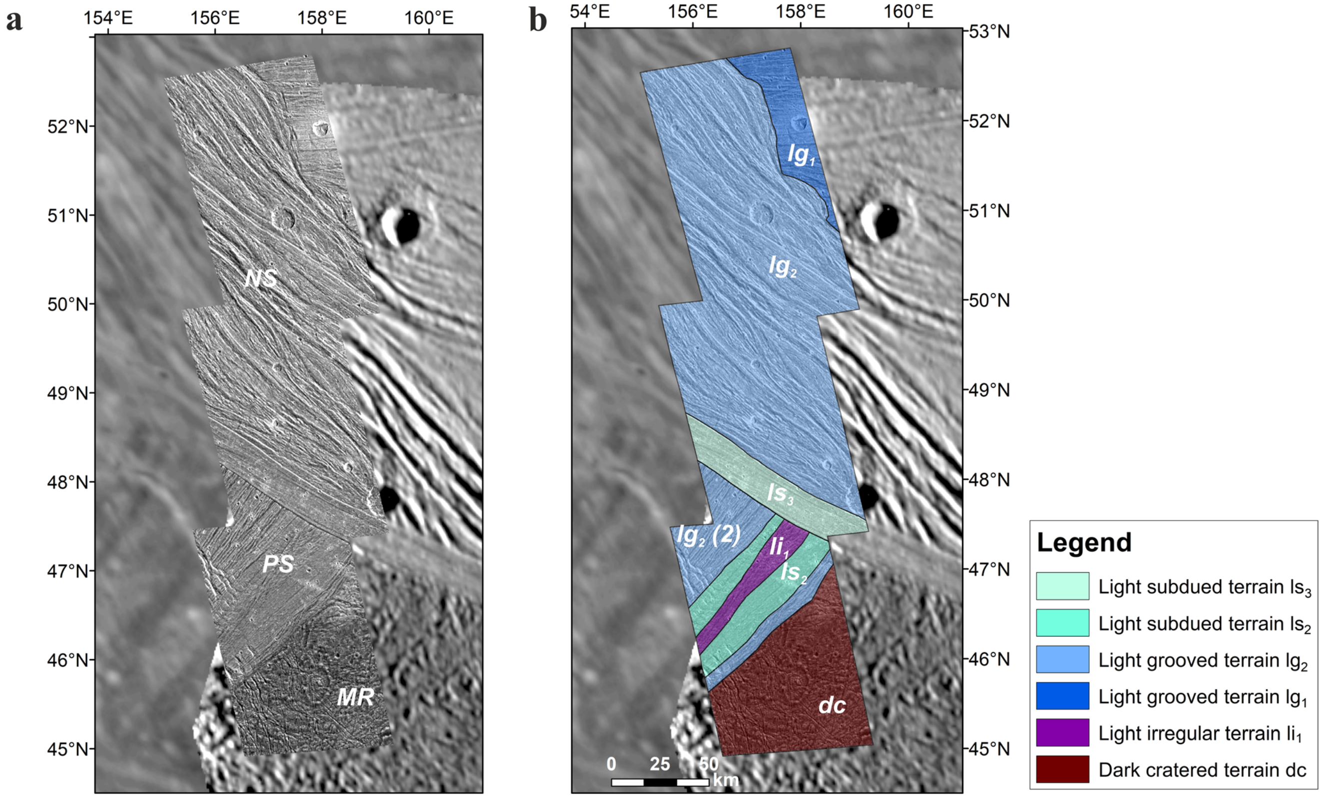

Figure 7. Region A/Nippur Sulcus: (a) SSI observation G2GSNIPPUR01 with the location of Philus (PS), Nippur Sulcus (NS), and Marius Regio (MR) indicated and (b) the associated geologic map produced following the mapping style of Collins et al. (2013).

Table 3
Measured CSFDs (N (10) and N (1)) for All Mapped Terrain Units in the Nippur and Philus Sulcus Region, Including LDM and JCM Age Estimates, Terrain Unit Areas, and the Number of Craters Counted

Region A	Terrain Unit	N (10) (km^{-2})	N (1) (km^{-2})	LDM (Ga)	JCM (Ga)	Area (km^2)	No. of Craters Counted
G2GSNIPPUR01 (Nippur Sulcus)	ls_3	$4.44 \times 10^{-5} \pm 4.26 \times 10^{-6}$	$5.00 \times 10^{-3} \pm 4.8 \times 10^{-4}$	$3.85^{+0.020}_{-0.023}$	$1.90^{+1.76}_{-1.15}$	1675.80	291
	lg_2	$5.54 \times 10^{-5} \pm 3.01 \times 10^{-6}$	$6.25 \times 10^{-3} \pm 3.39 \times 10^{-4}$	$3.90^{+0.084}_{-0.089}$	$2.32^{+1.70}_{-1.36}$	15,352.3	1624
	lg_2 (2)	$1.64 \times 10^{-5} \pm 3.61 \times 10^{-6}$	$1.85 \times 10^{-3} \pm 4.07 \times 10^{-4}$	$3.68^{+0.039}_{-0.055}$	$0.83^{+1.23}_{-0.53}$	4970.65	240
	ls_2	$2.05 \times 10^{-5} \pm 2.13 \times 10^{-6}$	$2.31 \times 10^{-3} \pm 2.4 \times 10^{-4}$	$3.72^{+0.019}_{-0.022}$	$1.01^{+1.40}_{-0.64}$	2670.53	217
	lg_1	$6.44 \times 10^{-5} \pm 5.48 \times 10^{-6}$	$7.26 \times 10^{-3} \pm 6.18 \times 10^{-4}$	$3.92^{+0.013}_{-0.014}$	$2.46^{+1.66}_{-1.42}$	1576.71	303
	li_1	$3.34 \times 10^{-5} \pm 4.79 \times 10^{-6}$	$3.77 \times 10^{-3} \pm 5.4 \times 10^{-4}$	$3.81^{+0.024}_{-0.028}$	$1.96^{+1.76}_{-1.18}$	808.295	95
	dc	$4.14 \times 10^{-5} \pm 1.98 \times 10^{-6}$	$4.67 \times 10^{-3} \pm 2.23 \times 10^{-4}$	$3.85^{+0.0077}_{-0.0081}$	$1.81^{+1.75}_{-1.10}$	4781.27	924

The geological units in transitional terrain includes superimposed generations of grooved and subdued light terrain (Figure 9(b)). The units li_1, ls_3, and lg_3 are part of Nippur Sulcus. From the cross-cutting relationship, the lg_3 and ls_3 terrains are found to be the youngest ones since they cross-cut adjacent terrains.

The light grooved terrain ls_3 is the youngest terrain in this region. It has a northwest–southeast trend, like ls_3 of Nippur Sulcus. Apart from a few lineaments, the terrain appears mostly very smooth. It has a single groove close to two craters with diameters of 7 and 4 km.

The most striking features of the area are sigmoidal-shaped light subdued terrains mapped as ls_2, which are surrounded by grooved and irregular terrains (lg_1 and lg_2). Some of the minor lineaments inside of these sigmoidal-shaped block units are curved like their borders. But most of the lineaments' spacing and orientation are not clear from this resolution image and the terrain appears mostly smooth. A small portion of dc is found inside unit ls_2.

The light grooved terrains lg_2 form narrow and elongated, vein-like zones, which constitute parallel to subparallel sets of ridges trending in the northwest–southeast direction. Their borders to the dark terrain dc are very sharp and are marked by ridges. The elevation of lg_2 seems to be lower than the surrounding dark terrain. A large, 37 km diameter crater of the neighboring dark terrain is being cut by one of the light terrain veins. The southern half of the crater is absent, suggesting either a large strike-slip offset or submergence beneath ice. The light grooved terrain lg_1 also belongs to the network of ls_2, but is somewhat younger as it is terminated by lg_2.

The unit ls_1 surrounds the sigmoidal-shaped ls_2 units in a vein-like network. The ridges of lg_1 are intensely grooved, linear to curvilinear in shape and produce a rough topography.

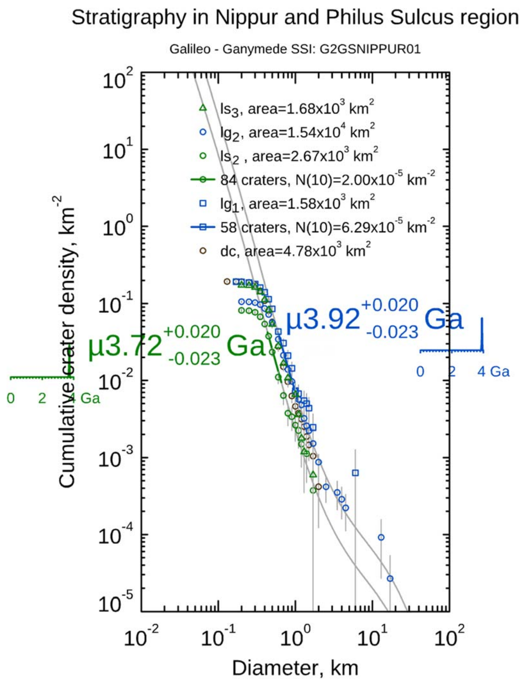

Figure 8. Comparison of the relative ages of the different terrain units in Nippur and Philus Sulcus (SSI observation G2GSNIPPUR01) based on CSFDs. The plot displayed here represents ages derived from LDM. For ages based on JCM, refer to Table 3.

The light irregular terrain li_1 is one of the oldest terrains in this region. It has irregular sets of lineaments with different orientation. It appears that li_1 is partly resurfaced by ls_2 and ls_3, and it is also cut by the veins lg_1.

As everywhere else the dark cratered terrain is the oldest unit. It appears strongly fractured. The fractures have overall trend in the northwest–southeast and in the westsouthwest–eastnortheast directions like lg_2 and lg_1. The orientation of lg_2 including the fractures within dc indicates that these are conjugate shear fractures. Indeed, the sigmoidal shape of ls_2 (reminiscent to SC fabrics) and the presence of a half crater cut by lg_2 demonstrate the importance of the conjugate shearing localized in lg_2 and lg_1.

ii. CSFDs

The youngest mapped units in the transitional terrain (Figure 9) i.e., lg_3 and ls_3, which were believed to be geologically cogenetic, have quite different CSFDs, which are precisely $5.17 \times 10^{-5} \pm 1.53 \times 10^{-5}$ km^{-2} and $1.72 \times 10^{-4} \pm 4.85 \times 10^{-5}$ km^{-2}, respectively (Table 4). The second youngest terrain, lg_2, lg_2 (2), and ls_2 are found to have similar CSFDs of $6.01 \times 10^{-5} \pm 9.76 \times 10^{-6}$ km^{-2}, $8.37 \times 10^{-5} \pm 1.61 \times 10^{-5}$ km^{-2}, and $6.40 \times 10^{-5} \pm 8.1 \times 10^{-6}$ km^{-2}, respectively. Mapping and crater counting match here. The oldest light terrains, lg_1 and li_1, have CSFDs of $4.06 \times 10^{-5} \pm 1.46 \times 10^{-5}$ km^{-2} and $1.15 \times 10^{-4} \pm 2.04 \times 10^{-5}$ km^{-2}, respectively. Unlike li_1, lg_1 has a lower CSFD than all other terrain units (younger than Category 1 and 2 terrains). In other words, lg_1 was expected to have a much higher CSFD than all other terrains except for li_1, whose CSFD is similar to the dark terrain. The dark cratered terrain (dc) has a CSFD of $1.23 \times 10^{-4} \pm 1.03 \times 10^{-5}$ km^{-2}, which is in accordance to the geological context.

The high CSFD of ls_3 equivalent to that of dc and the low value for lg_1 is not understood, and disagrees with the relative chronology derived from the cross-cutting relationships (Figure 10). Overall, the higher CSFDs observed in most terrains, as compared to the adjacent Byblus Sulcus, may be attributed to secondaries impinging from the pene-palimpsest Epigeus or to the possibility that the light terrain here was formed during an earlier stage, perhaps soon after the formation of the dark terrain.

4.2. Region B: Arbela Sulcus

The narrow band (width ∼21 km) of light terrain constituting Arbela Sulcus located at 21.1° S, 10.2° E was selected for Region B (Figures 1(c) and 11). Arbela Sulcus traverses the dark terrain of Nicholson Regio located in the southern part of Ganymede's sub-Jovian hemisphere. Nicholson Regio is a type locality of the so-called Nicholsonian, the oldest stratigraphic unit or chronological period on Ganymede in the current time–stratigraphic system established by Collins et al. (2013). Unlike Harpagia Sulcus (Region C, Figures 1(d) and 13), which confines with Nicholson Regio in the north and west, Arbela Sulcus has an overall trend in the northeast–southwest direction and terminates Nicholson Regio in the southeast. The high-resolution images of the Galileo SSI observation sequences 28GSARBELA01+02 and G7GSNICHOL01+02 with spatial resolution between 34 and 133 m pixel^{-1} offer a detailed look into this area (Figure 11(a)).

4.2.1. Arbela Sulcus (G28GSARBELA02 and G7GSNICHOL01)

i. Geological Mapping

The geological units of Arbela Sulcus from young to old are light subdued terrain ls_3 and light grooved terrain lg_2. They form vein-like systems within dark terrain. The dark lineated (dl) terrain is younger than the dark cratered terrains (dc; Figure 11(b)).

The light subdued terrain ls_3 of Arbela Sulcus forms a narrow, smooth band with straight and parallel boundaries. It trends in the northeast–southwest direction. It has an average width of about 20–30 km but it narrows down to less than 15 km in its north. It has sharp troughs at its borders which separates it from the other units. It has parallel ridges and troughs but unlike lg_2, it appears striated only in some areas. ls_3 is topographically lower than lg_2 and the dark terrains dl and dc (Giese et al. 2001). The light grooved terrain lg_2 is strongly grooved with densely packed sets of lineaments. Like ls_3, it trends in the northeast–southwest direction. It has an average width of about 30–40 km. A sharp border to the dark terrain is not observed but uneven sets of lineaments form its borders. The ridges and grooves have a curvilinear appearance. These grooves are interconnected with the grooves of dl. The length of ridges varies from a few kilometers to 50 km. The average spacing between the ridges is less than 1 km.

The dark lineated terrain dl shows abundant lineaments. The lineaments are unevenly spaced and are parallel to subparallel to each other within each set. Compared to lg_2, the lineaments in dl are widely spaced. The spacing between the lineaments in most cases is ∼1 km. The lineaments are connected to each other and also connected to lg_2. But there are some lineaments that on one side of dl do not have counterparts on the other side. The lineaments east of lg_2 mostly trend in the northeast–southwest direction similar to $lg_2$2, but west of lg_2 lineament sets perpendicular to lg_2 exist. There are many craters being cut by lineaments or fractures, distorting them from their actual

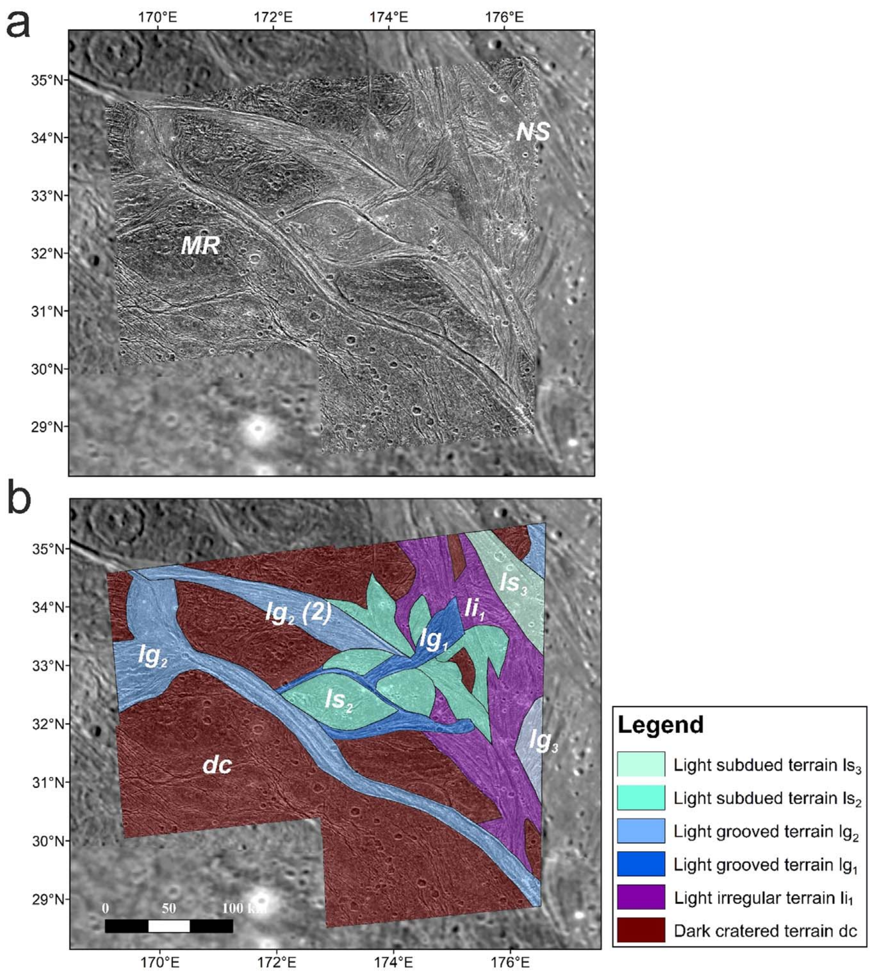

Figure 9. Region A/Transitional terrain: (a) SSI observation G2GSTRANST01 with the location of Marius Regio (MR) and Nippur Sulcus (NS) indicated and (b) the associated geologic map produced following the mapping style of Collins et al. (2013).

Table 4

Measured CSFDs (N (10) and N (1)) for All Mapped Terrain Units in the Transitional Terrain, Including LDM and JCM Age Estimates, Terrain Unit Areas, and the Number of Craters Counted

Region A	Terrain Unit	N (10) (km^{-2})	N (1) (km^{-2})	LDM (Ga)	JCM (Ga)	Area (km^2)	No. of Craters Counted
G2GSTRANST01 (Transitional terrain)	lg_3	$5.17 \times 10^{-5} \pm 1.53 \times 10^{-5}$	$5.83 \times 10^{-3} \pm 1.72 \times 10^{-3}$	$3.88^{+0.041}_{-0.047}$	$2.13^{+1.74}_{-1.37}$	922.337	23
	ls_3	$1.72 \times 10^{-4} \pm 4.85 \times 10^{-5}$	$1.94 \times 10^{-2} \pm 5.47 \times 10^{-3}$	$4.07^{+0.037}_{-0.041}$	$4.00^{+0.55}_{-1.71}$	2153.93	49
	lg_2	$6.01 \times 10^{-5} \pm 9.76 \times 10^{-6}$	$6.78 \times 10^{-3} \pm 1.09 \times 10^{-3}$	$3.91^{+0.023}_{-0.028}$	$2.37^{+1.69}_{-1.38}$	8243.58	81
	lg_2 (2)	$8.37 \times 10^{-5} \pm 1.61 \times 10^{-5}$	$9.44 \times 10^{-3} \pm 1.82 \times 10^{-3}$	$3.96^{+0.027}_{-0.034}$	$2.92^{+1.43}_{-1.60}$	3134.09	41
	ls_2	$6.40 \times 10^{-5} \pm 8.1 \times 10^{-6}$	$7.21 \times 10^{-3} \pm 9.13 \times 10^{-4}$	$3.92^{+0.019}_{-0.022}$	$2.47^{+1.65}_{-1.42}$	6365.98	125
	lg_1	$4.06 \times 10^{-5} \pm 1.46 \times 10^{-5}$	$4.58 \times 10^{-3} \pm 1.65 \times 10^{-3}$	$3.85^{+0.050}_{-0.059}$	$1.78^{+1.75}_{-1.09}$	4817.12	26
	li_1	$1.15 \times 10^{-4} \pm 2.04 \times 10^{-5}$	$1.30 \times 10^{-2} \pm 2.30 \times 10^{-3}$	$4.01^{+0.025}_{-0.030}$	$3.44^{+1.06}_{-1.74}$	9266.77	91
	dc	$1.23 \times 10^{-4} \pm 1.03 \times 10^{-5}$	$1.39 \times 10^{-2} \pm 1.16 \times 10^{-3}$	$4.02^{+0.012}_{-0.013}$	$3.54^{+0.97}_{-1.75}$	72,876.6	728

circular shape. For instance, the crater west to ls_3 and lg_2 is separated by dl at its center by a distance of about 21 km.

The dark cratered terrain dc is an intensely cratered terrain. It is unevenly distributed within dl and there is no distinctive border between them. It appear as patches embedded in dl.

The cross-cutting relationships and orientations of all terrains suggest that evident tectonic reworking has taken place in this region. lg_2 is interpreted as a result of shearing which includes ~65 km of left-lateral strike-slip movement followed by ~25 km of crustal separation creating ls_3 and ~4° counterclockwise relative rotation of the eastern side of lg_2 (Head et al. 2002). The intermediate age of dl between that of dark cratered terrain and light terrains would be indicative of a gradual transition from dark terrain to light terrain.

ii. CSFDs

The two light terrains ls_3 and lg_2 in Arbela Sulcus (Figure 11), whose CSFDs are $2.95 \times 10^{-5} \pm 4.73 \times 10^{-6}$ km^{-2} and $2.00 \times 10^{-5} \pm 2.89 \times 10^{-6}$ km^{-2}, respectively (Table 5), have lower CSFDs than dl ($6.02 \times 10^{-5} \pm 1.17 \times 10^{-5}$ km^{-2}) and dc ($1.78 \times 10^{-4} \pm 3.64 \times 10^{-5}$ km^{-2}), which are all consistent with

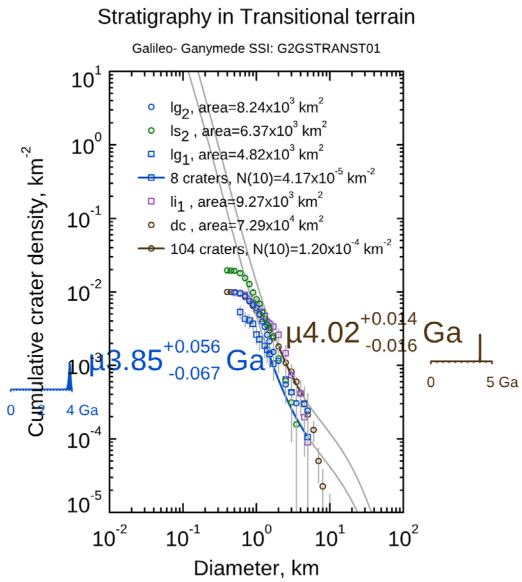

Figure 10. Comparison of relative ages of different terrain units in transitional terrain (SSI observation G2GSTRANST01) based on CSFDs. The plot displayed here represents ages derived from LDM. For ages based on JCM, refer to Table 4.

the geological mapping. The minor difference in the CSFDs between ls_3 and lg_2 indicates formation within a short period (Figure 12).

4.3. Region C: Harpagia Sulcus

Harpagia Sulcus (Region C, Figures 1(d) and 13, 15, and 17), an extensively resurfaced portion of Ganymede's light terrain is situated at southern near-equatorial latitudes of the sub-Jovian hemisphere. It confines the northern and western border of Nicholson Regio. The high-resolution images 28GSBRTDRK02 (Figure 13) and 28GSCALDRA02 (Figure 15) allow us to study the direct contact of Harpagia Sulcus with the dark terrain of Nicholson Regio, while 28GSSMOOTH02 (Figure 17) is completely enclosed within the Sulcus.

4.3.1. Harpagia Sulcus I (28GSBRTDRK02)

i. Geological Mapping

The given image shows a part of Harpagia Sulcus and Nicholson Regio located in the sub-Jovian hemisphere at ∼14° S, 40°S, with a spatial resolution of 121 m pixel^{-1} (Figure 13(a)). The various light terrain units of Harpagia Sulcus trend northwest–southeast and cross-cut the dark terrain of Nicholson Regio. The geological subdivision is shown in Figure 13(b). The light terrain units are aligned parallel to each other except for the youngest units, ls_3 and lg_3, which branch off from this trend obliquely like a railroad switch. It has an average width of about 13 km. The light grooved terrain lg_3 borders ls_3 on both sides. The light subdued terrain ls_2 is a narrow, smooth terrain unit within lg_2. It trends in the northwest–southeast direction like its adjacent terrains. It has an average width of about 25 km. The eastern light grooved terrain lg_2 is obliquely cut by the younger unit lg_3. The western lg_2 occurrence has a sharp grooved contact to the dark terrain of Nicholson Regio, which is characterized by predominantly deeply incised, roughly 20 km long grooves that trend in northwest direction, and many impact craters as large as 33 km in diameter. From these cross-cutting relationships we could infer that lg_3 and ls_3 were formed later than lg_2 and ls_2. But among these terrains, it is unclear whether lg or ls is younger.

ii. CSFDs

The light terrain units, lg_3 and ls_3, have CSFDs of $1.31 \times 10^{-5} \pm 2.31 \times 10^{-6}$ km^{-2} and $4.20 \times 10^{-5} \pm 1.12 \times 10^{-5}$ km^{-2}, respectively (Table 6). The large difference between these units and the high value of the CSFD for ls_3 are remarkable, as both units belong to the same category. A similar trend can be observed for lg_2 ($2.00 \times 10^{-5} \pm 3.53 \times 10^{-6}$ km^{-2}) and ls_2 ($4.18 \times 10^{-5} \pm 4.0 \times 10^{-6}$ km^{-2}). One reason for such a discrepancy between lg and ls is that either the smooth ls terrains are indeed older than lg, suggesting a real difference in age, or both ls units are cogenetic. Alternatively, the nature of the smooth terrain makes it highly unlikely to miss craters, whereas the high relief grooved terrain makes it highly likely to miss craters on the slopes, and hence the identification of craters is subject to a non-zero error. As geologically expected the dark cratered terrain (dc; $1.47 \times 10^{-4} \pm 3.34 \times 10^{-5}$ km^{-2}) has the highest CSFD among other terrain units (Figure 14).

4.3.2. Harpagia Sulcus II (28GSCALDRA02)

i. Geological Mapping

This region lies roughly 300 km south of Harpagia Sulcus I. It includes a part of Harpagia Sulcus located near the prominent impact crater Enkidu (∼26.6°S, ∼34.9°E). The two Galileo contextual images, 28GSCALDRA02 have a spatial resolution of 147 m pixel^{-1} and the four high-resolution images, 28GSCALDRA01, have a spatial resolution of 42 m pixel^{-1} (Figure 15(a)). The region comprises various light terrains, dark terrains (dc and dl), and two caldera-like depressional features (Figure 15(b)). The subdued light terrains (ls_1 and ls_1 (2)) are found to be the youngest terrains that cross-cut the dark terrains. The lineated dark terrain dl is found to be intermediate in age as it cross-cuts the dark cratered terrain. All of these terrains are aligned northwest–southeast parallel to each other. The western border between light and dark terrains is very sharp, while gradual transitions occur with the dark lineated terrain. Specific structures are two caldera-like features like the Hammamat Patera (HP; Figure 15(a)), which are formed within the ls_1 terrain. Spaun et al. (2001) observed that caldera-like features have an inward-facing scarp. The scarps are high standing, and the interiors of the caldera-like features are depressed with a very smooth appearance. From the cross-cutting relationships, caldera-like features are found to be the lately formed ones. Previous studies have suggested that these features are only present on light terrains, and may serve as source vents for icy volcanism (Lucchita 1980; Schenk & Moore 1998; Kay & Head 1999; McKinnon et al. 2001; Spaun et al. 2001).

The dark lineated terrains dl (1 + 2) are separated by ls_1 (2). The terrain unit dl (1) contains some sinuous lineaments that also extends into ls_1 (2). In contrast, the dark cratered terrain dc shows very few lineaments, but is highly cratered. Along the sharp border to the light terrain, there is a crater that is exactly cut into half. The missing half is not exposed. The light terrain ls_1 shows a polygonal crater, whose straight rim segment is defined by a lineament.

ii. CSFDs

The two light terrain units, ls_1 and ls_1 (2), have CSFDs of $2.09 \times 10^{-4} \pm 2.26 \times 10^{-5}$ km^{-2} and $1.63 \times 10^{-4} \pm 4.17 \times$

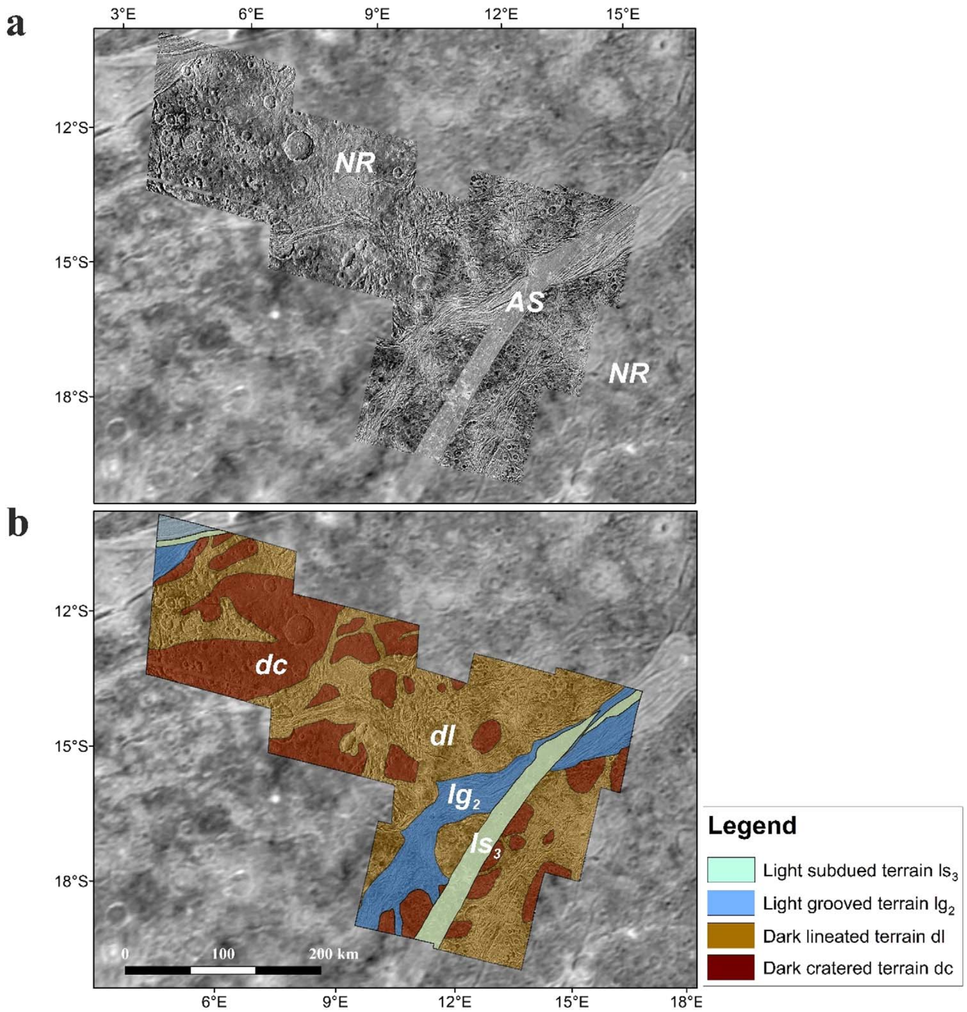

Figure 11. Region B/Arbela Sulcus: (a) SSI mosaic combining observations 28GSARBELA02 and G7GSNICHOL01 with the location of Arbela Sulcus (AR) and Nicholson Regio (NR) and (b) the associated geologic map produced following the mapping style of Collins et al. (2013).

10^{-5} km^{-2}, respectively (Table 7). The two dark lineated terrains, dl (1) and dl (2), have CSFDs of $1.83 \times 10^{-4} \pm 4.67 \times 10^{-5}$ km^{-2} and $1.61 \times 10^{-4} \pm 3.81 \times 10^{-5}$ km^{-2}. Their CSFDs are similar among each other and also with regard to the ls units (Figure 16). However, according to their cross-cutting relationships, the lineated dark terrain unit dl is expected to have higher CSFDs than ls terrains. As expected, the dark cratered terrain (dc) has the highest CSFD of $3.94 \times 10^{-4} \pm 3.48 \times 10^{-5}$ km^{-2}.

Possible explanations for the counterintuitive CSFDs of dl and ls are a number of potential secondary craters on these terrains formed by the Enkidu crater or some degree of resurfacing.

4.3.3. Harpagia Sulcus III (28GSSMOOTH02)

i. Geological Mapping

At a distance of about 180 km east of Harpagia Sulcus I (Figure 13(a)), there lies the SSI observation sequence 28GSSMOOTH02 (Figure 17(a)). The two images have a spatial resolution of about 116 m pixel^{-1}. This portion is located at ∼16°S, 50 °E completely within Harpagia Sulcus and comprises an area of about 24,649 km^2. The four high-resolution 16 m pixel^{-1} images provide a more detailed view of the contact between the light subdued terrain ls$_2$ and the light grooved terrain lg$_2$ (Figure 17(b)). The exposed subdued and grooved terrains all belong to the light terrains (Figure 17(c)). The cross-cutting relationships allows us to derive a relative chronology from lg$_3$ (youngest) via ls$_2$ and lg$_2$ to ls$_1$ (oldest). All light terrain units are characterized by different orientations of their lineaments, with typical form unconformity angles of ∼30° at the border of adjacent terrains. In contrast to previous case studies, lg$_3$ is the youngest terrain unit that has a strongly grooved surface while the older unit ls$_1$ is relatively smooth with subdued lineaments. This unit hosts the largest impact structure of the scene whose continuous ejecta blanket is clearly visible. The crater has a diameter of about 19 km with a small central pit.

While the light grooved terrains lg$_3$, lg$_2$, and ls$_1$ contain long, parallel, and equally spaced ridges and troughs, the undivided terrain (undiv) differs from the other grooved terrains for the presence of strongly curved lineaments that are cross-cut by lg$_3$.

ii. CSFDs

The youngest terrain units, lg$_3$and lg$_3$ (2), have CSFDs of $1.66 \times 10^{-5} \pm 2.87 \times 10^{-6}$ km^{-2} and $2.87 \times 10^{-5} \pm 1.64 \times 10^{-5}$ km^{-2} (Table 8). These CSFDs are similar to the terrains lg$_2$ and ls$_2$, with CSFDs of $1.23 \times 10^{-5} \pm 1.96 \times 10^{-6}$ km^{-2} and $2.81 \times 10^{-5} \pm 2.98 \times 10^{-6}$ km^{-2}, respectively. Consistent with the geological findings, the light terrain ls$_1$

Table 5
Measured CSFDs (N (10) and N (1)) for All Mapped Terrain Units in the Arbela Sulcus Region, Including LDM and JCM Age Estimates, Terrain Unit Areas, and the Number of Craters Counted

Region B	Terrain Unit	N (10) (km^{-2})	N (1) (km^{-2})	LDM (Ga)	JCM (Ga)	Area (km^2)	No. of Craters Counted
28GSARBELA02/G7GSNICHOL01 (Arbela Sulcus)	ls_3	$2.95 \times 10^{-5} \pm 4.73 \times 10^{-6}$	$3.33 \times 10^{-3} \pm 5.33 \times 10^{-4}$	$3.79^{+0.026}_{-0.031}$	$1.37^{+1.63}_{-0.86}$	7086.41	85
	lg_2	$2.00 \times 10^{-5} \pm 2.89 \times 10^{-6}$	$2.25 \times 10^{-3} \pm 3.26 \times 10^{-4}$	$3.72^{+0.026}_{-0.031}$	$0.99^{+1.38}_{-0.63}$	12,872.1	137
	dl	$6.02 \times 10^{-5} \pm 1.17 \times 10^{-5}$	$6.79 \times 10^{-3} \pm 1.32 \times 10^{-3}$	$3.91^{+0.028}_{-0.035}$	$2.60^{+1.60}_{-1.48}$	20,781.0	468
	dc	$1.78 \times 10^{-4} \pm 3.64 \times 10^{-5}$	$2.01 \times 10^{-2} \pm 4.13 \times 10^{-3}$	$4.08^{+0.028}_{-0.034}$	$4.04^{+0.52}_{-1.69}$	7380.38	1,062

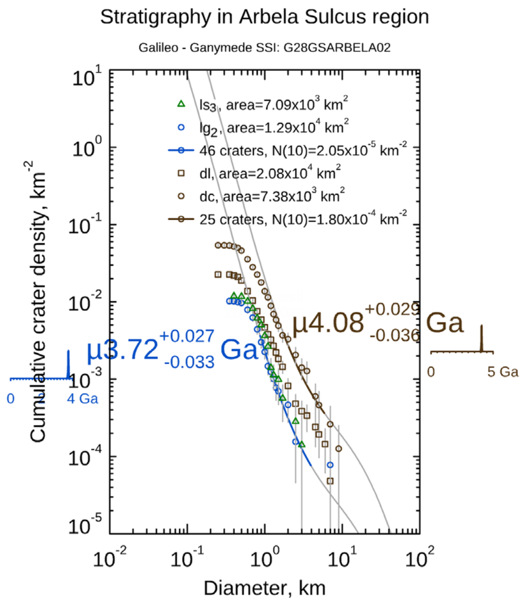

Figure 12. Comparison of relative ages of different terrain units from Region B based on CSFDs: Arbela Sulcus—SSI observation 28GSARBELA02. The plot displayed here represents ages derived from LDM. For ages based on JCM, refer to Table 5.

shows a slightly higher CSFD than the other terrain units (Figure 18). We measured two possible CSFDs of $7.97 \times 10^{-5} \pm 3.02 \times 10^{-5}$ km^{-2} and $1.93 \times 10^{-5} \pm 1.91 \times 10^{-6}$ km^{-2}. The two CSFD values are due to two cumulative curves that best fit the data points. Such an uneven CSFD within ls_1 may indicate the imprint of secondaries or local resurfacing. The formation time differences between lg_3 and $lg_3(2)$ may be real, as they are not directly connected to each other. The low CSFD measured in the undiv light terrain suggests that deformation has erased some craters.

4.4. Region D: Erech, Sippar, and Mummu Sulci

The portions of Erech, Mummu, and Sippar Sulci observed by Galileo SSI selected for Region D constitute extended light terrain units located in the southern near-equatorial and midlatitudes of Ganymede's anti-Jovian hemisphere, northwest to Osiris crater (Figures 1(a) and (e)). Mostly Mummu and Sippar Sulci consist of terrain units trending in an east–west direction, while Erech Sulcus lies perpendicular to it (Figures 19 and 21). These Sulci form the southern margin of the dark terrain Marius Regio. The region observed in G8GSCALDRA01 constituting Mummu and Sippar Sulcus lies approximately 480 km south of Erech Sulcus (G8GSERECH01), in which Erech Sulcus is being cross-cut by Sippar Sulcus. The light terrain (lg_2) of Erech Sulcus decreases in width toward the north, where it is cross-cut by Uruk Sulcus.

4.4.1. Erech Sulcus (G8GSERECH01)

i. Geological Mapping

Erech Sulcus is a 75–85 km wide band of light terrain (lg_2), located in the anti-Jovian hemisphere at ∼16°S, 177°W trending in a north–south direction and cutting through the dark terrain of Marius Regio. The terrain extends for approximately 900 km in the northward direction. The Galileo image mosaic has a resolution of 143 m pixel^{-1} (Figure 19(a)). Erech Sulcus has a pronounced relief caused by parallel to subparallel grooves and partly spindle-like ridges. Erech Sulcus is cut by the east–west trending younger Sippar Sulcus (ls_3). This Sulcus is adjacent to the large crater named Melkart. The mapped terrains of Sippar Sulcus are subdivided according to superposition and surface properties (Figure 19(b)). The terrain ls_3 is a narrow band of ∼9 km width bifurcating westward. This unit has a smooth and only weakly lineated surface. Although it is the youngest unit, the terrain shows a large number of craters. The proximity of Melkart crater may be the factor contributing to the large number of craters in the area. The borders of the terrain are sharp with all its adjacent terrains.

The light irregular terrain unit li_1 is a small triangular-shaped area between the two bifurcating arms of ls_3 with differently oriented lineaments. To the west, it borders with a sharp trough to the light subdued terrain ls_1, whose surface appears smooth, except for a few distinct grooves. The outer shape and the internal lineament structure of the light subdued terrain ls_2 are remarkably curved.

This is in stark contrast to the light grooved terrain lg_1 whose long ridges are straight and parallel and exceed a length of 70 km. This unit is separated from the adjacent terrains by means of oblique contacts. The dark cratered terrain dc has a high crater density and many northwest–southeast trending fractures. Its borders with the light terrains are sharp and the terrain seems to be slightly elevated with respect to lg_2 and ls_3. At 16.5° S, 175.5°W lies a half-circular feature whose classification as either a crater or caldera cannot be determined with certainty.

ii. CSFDs

The youngest terrain known from cross-cutting relationship, ls_3, has a CSFD of $7.52 \times 10^{-5} \pm 1.3 \times 10^{-5}$ which is very similar to the CSFDs obtained for the other light terrains of this studied area (Table 9). The minimum value was found for lg_2 ($5.65 \times 10^{-5} \pm 1.45 \times 10^{-5}$). The oldest light terrains outlined in the geological maps, i.e., ls_1, lg_1, and li_1, have CSFDs of $7.39 \times 10^{-5} \pm 2.02 \times 10^{-5}$, $9.93 \times 10^{-5} \pm 1.93 \times 10^{-5}$, and $7.56 \times 10^{-5} \pm 2.87 \times 10^{-5}$, respectively. The dark terrain dc has a CSFD of $1.49 \times 10^{-4} \pm 1.39 \times 10^{-5}$, which, unlike what is observed in the other regions, is only slightly higher than the light terrains (Figure 20).

To conclude, we found that the CSFDs of all terrains are very similar and also the difference between the light and dark terrains is minimal. In other words, the CSFDs of light terrains are much higher than the CSFDs in other regions. We propose that secondary craters formed by material ejected from Melkart crater (which is ∼340 km away from this study area) may have masked and modified the original CSFDs. The secondaries covering all the studied terrains of this area were then wrongly marked as primaries.

4.4.2. Mummu and Sippar Sulcus (G8GSCALDRA01)

i. Geological Mapping

Mummu and Sippar Sulcus are located on the anti-Jovian hemisphere at ∼39°S, 180° E (Figures 1(e) and 21). The images acquired during the sequence G8GSCALDRA01 have a resolution of 179 m pixel^{-1} (Figure 21(a)). The mosaic shows a complex pattern of cross-cutting relationships of 28 light terrain units. The terrain types observed include three superimposed generations of light grooved terrains (lg_1, lg_2, and lg_3), light subdued terrains (ls_1, ls_2, and ls_3), light irregular terrains (li_1, li_2, and li_3), plus reticulate terrains (Figure 21(b)). The most striking features are seven caldera-like depressions. The light

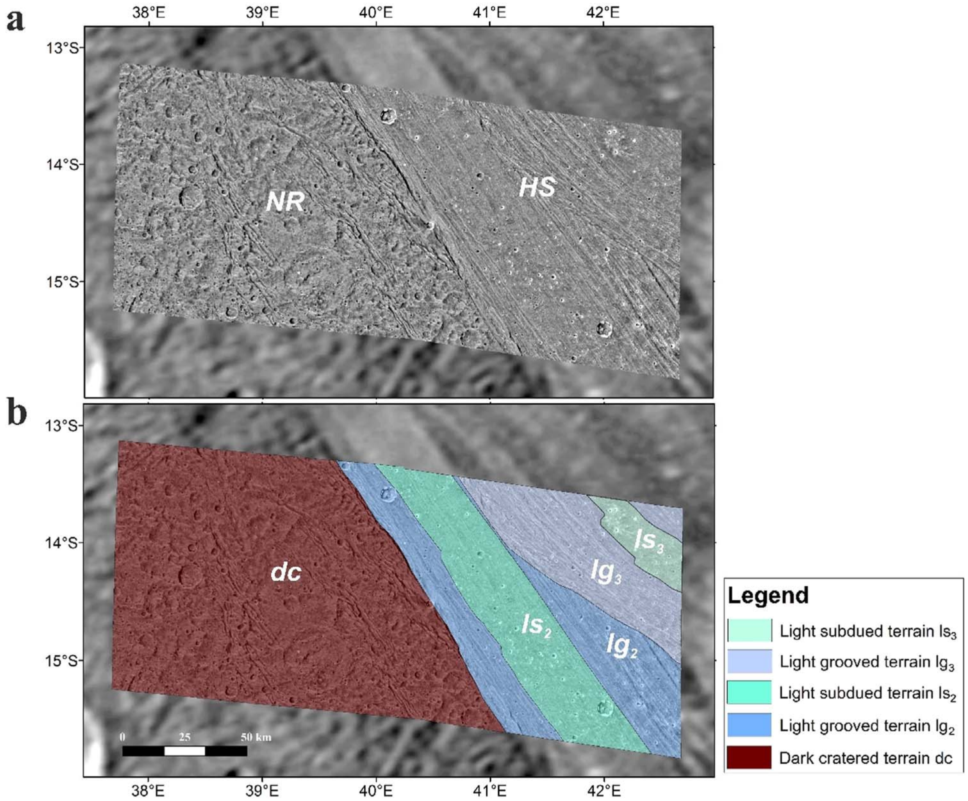

Figure 13. Region C/Harpagia Sulcus I: (a) SSI observation 28GSBRTDRK01/02 with the location of Nicholson Regio (NR) and Harpagia Sulcus (HS) indicated and (b) the associated geologic map produced following the mapping style of Collins et al. (2013).

Table 6
Measured CSFDs (N (10) and N (1)) for All Mapped Terrain Units in the Harpagia Sulcus I Region, Including LDM and JCM Age Estimates, Terrain Unit Areas, and the Number of Craters Counted

Region C	Terrain Unit	N (10) (km^{-2})	N (1) (km^{-2})	LDM (Ga)	JCM (Ga)	Area (km^2)	No. of Craters Counted
28GSBRTDRK02 (Harpagia Sulcus I)	lg_3	$1.31 \times 10^{-5} \pm 2.31 \times 10^{-6}$	$1.48 \times 10^{-3} \pm 2.6 \times 10^{-4}$	$3.63^{+0.036}_{-0.048}$	$0.67^{+1.06}_{-0.44}$	3163.81	49
	ls_3	$4.20 \times 10^{-5} \pm 1.12 \times 10^{-5}$	$4.74 \times 10^{-3} \pm 1.26 \times 10^{-3}$	$3.85^{+0.038}_{-0.043}$	$1.83^{+1.75}_{-1.11}$	606.372	27
	lg_2	$2.00 \times 10^{-5} \pm 3.53 \times 10^{-6}$	$2.26 \times 10^{-3} \pm 3.98 \times 10^{-4}$	$3.72^{+0.030}_{-0.039}$	$0.99^{+1.38}_{-0.63}$	6587.83	81
	ls_2	$4.18 \times 10^{-5} \pm 4.0 \times 10^{-6}$	$4.71 \times 10^{-3} \pm 4.51 \times 10–4$	$3.85^{+0.015}_{-0.017}$	$1.82^{+1.75}_{-1.11}$	3145.05	166
	dc	$1.47 \times 10^{-4} \pm 3.34 \times 10^{-5}$	$1.66 \times 10^{-2} \pm 3.76 \times 10^{-3}$	$4.05^{+0.030}_{-0.039}$	$3.80^{+0.74}_{-1.75}$	11,802.6	458

subdued terrain ls_3 is a narrow, smooth, and subdued terrain bifurcating in the west and has a width of ∼25 km. Like in most of the previous study areas, the smoothest terrain is the youngest. Six of the seven caldera-like features are cross-cut by the youngest terrain ls_3 or merge with it. The calderas are always asymmetric with a steep inward-facing fault scarp. This fault scarp shows indentations. The low-lying caldera interiors contain smooth material that seems to have flown out on one side toward the ls_3 unit.

Light terrains are more frequent than reticulate terrains, which are found to be the oldest terrain type in this area. This region is a good example because all types of grooves and ridges exist, ranging from sharp edged (grooved and irregular terrains) to faint ones (subdued terrains; Baby et al. 2022). Clusters of irregular craters often found on the subdued terrains are interpreted as secondary craters, which radiate from the large Osiris crater (38° S, 193.69° E; Figure 1(a)), which is ∼440 km away from the study area.

The light grooved terrains, lg_3, lg_3 (2), lg_3 (3), lg_3 (4), and lg_3 (5), form narrow and deep troughs just a few kilometers wide. Their borders with adjacent terrains are usually sharp. In contrast, the light subdued terrains, ls_2 and ls_2 (2), are much broader, showing a smooth relief. The light grooved terrains lg_2, lg_2 (2), and lg_2 (3) are broader than the younger lg_3 generation. However, the lineaments in lg_2 (2) have a trend in the east–west direction, while those in lg_2 (3) have a trend in the northwest–southeast direction. The light grooved terrains, lg_1, lg_1 (2), lg_1 (3), and lg_1 (4), are broad and grooved. Their borders separating them from adjacent terrains are sharp. The lineaments they contain appear to have similar widths, lengths, spacings, and orientations.

The light irregular terrains li_1, li_1 (2), li_1 (3), and li_1 (4) have very rough surface morphologies with lineaments occurring in various directions. Mummu and Sippar Sulci are examples of the complex tectonic processes imprinting one over the other in which the dark terrain is completely erased by the formation of

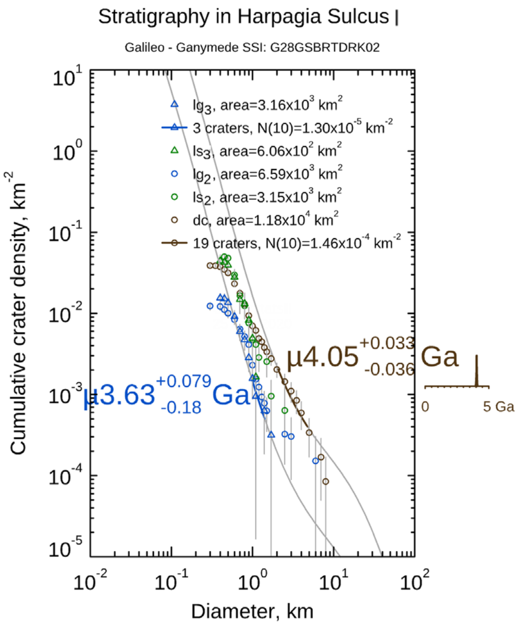

Figure 14. Comparison of the relative ages of different terrain units from Harpagia Sulcus I (SSI observation G28GSBRTDRK02) based on CSFDs. The plot displayed here represents ages derived from LDM. For ages based on JCM, refer to Table 6.

light terrain. The light terrains intersect and cut across one another, sometimes leaving only a small portion of a particular type of terrain visible. Earlier studies suggested that a combination of cryovolcanism and tectonic activities played an important role in shaping the present light terrains (Schenk et al. 2001; Showman et al. 2004).

ii. CSFDs

The youngest terrains known from cross-cutting relationships, ls_3, lg_3, and $li_{3,}$ have CSFDs that lie in the range from 3.45×10^{-5} to 1.416×10^{-4} km^{-2} (when considering the upper and lower error bars of the uncertainty values; Table 10). Among these, lg_3 and lg_3 (4) have similar CSFDs of $4.75 \times 10^{-5} \pm 1.3 \times 10^{-5}$ km^{-2} and $5.23 \times 10^{-5} \pm 7.42 \times 10^{-6}$ km^{-2}, respectively, which are lower in comparison to those of other terrains. Apart from lg_3 and lg_3 (4), the other studied terrains are characterized by CSFDs with values similar to each other and to any typical dark terrain. The second youngest terrains inferred from mapping results, ls_2, lg_2, and li_2, have CSFDs that lie in the range from 6.3296×10^{-5} to 3.059×10^{-4} km^{-2} (when considering the upper and lower error bars of the uncertainty values). This range overlaps with that of the younger ones. The oldest light terrains inferred from the mapping results, ls_1, lg_1, and li_1, as well as the reticulate terrain, have CSFDs that lie in the range from 2.14×10^{-5} to 1.687×10^{-4} km^{-2} (when considering the upper and lower error bars of the uncertainty values; Figure 22). Again, this shows a complete overlap between the CSFDs of the oldest and youngest light terrain units. Overall, the CSFDs are quite high, comparable to those of the dark terrains found in other locations.

To summarize, the CSFDs of the light terrains are much higher than the CSFDs in other study regions and show only small differences between the various light terrain units, which are often in contraposition to geological observations. Like for Erech Sulcus, the reasons for such similar CSFDs could be the superposition with secondary craters, which formed by the material ejected by Osiris crater (∼440 km east from this study area). The secondaries have evenly disturbed all the terrains, and were mistaken as primaries due to the close similarity in shape between the two sets of landforms. Overprinting with secondaries prevents us from correctly constraining the period of light terrain formation. Hence, geological interpretation by the cross-cutting relationship is the better method here to derive a relative chronology.

5. AMAs of the Mapped Terrain Units

Despite the uncertainties in determining the absolute ages of Ganymede's geologic units, we applied impact crater chronology models to understand better and constrain the formation period of the light terrains and to shed some light into Ganymede's geologic evolution. Additionally, we aimed to constrain the prerequisites that should be implemented and/or improved when using these models before the JUICE spacecraft will arrive in the Jovian system.

Region A

In Byblus Sulcus, the youngest unit is the fresh crater Nergal (Figures 1(b) and 5(a)), whose model age ranges between ∼1.2 and ∼2.7 Ga (LDM; ±1 Ga) and ∼0.1 to ∼0.4 Ga (JCM), and acts as a stratigraphic marker (Figure 23(a)). Among all the terrain units in Region A, the transitional region shows a higher CSFD than the various units of Byblus and Nippur Sulcus. Moreover, the range of ages in the ls and li terrain units of the transitional region is high. In contrast, the CSFDs and hence the period of formation of Byblus and Nippur Sulcus suggest a rather short period of formation. The formation period of all light terrains units lies between ∼3.68 Ga and ∼4.07 Ga (LDM; ±0.1–0.2 Ga) or ∼0.83 Ga and ∼4 Ga (JCM). The model ages of the dark terrains of Marius Regio range between ∼3.85 and ∼4.17 Ga (LDM; ±0.1–0.2 Ga) or ∼1.81 to ∼4.46 Ga (JCM). Thus, using LDM the light terrain could have formed immediately after the dark terrain. In JCM, the formation period of light terrains lasts considerably longer.

Region B

In Arbela Sulcus, the youngest unit is the fresh crater Enkidu (Figure 1(a)), which seems to have formed shortly after the light terrain (Figure 23(b)). The light terrains have formation ages of ∼3.72 to ∼3.79 Ga (LDM; ±0.1–0.2 Ga) or ∼0.99 to ∼1.37 Ga (JCM). The dark terrains (dc and dl) of Nicholson Regio formed between ∼3.91 and ∼4.08 Ga (LDM; ±0.1–0.2 Ga) or ∼2.60 to ∼4.04 (JCM). Thus, the dark terrain is somewhat older in comparison to Region A. There is a possible hiatus between the dark and light terrain formation. However, Region B is less well explored than the other regions.

Region C

In Harpagia Sulcus, the youngest unit is crater Kittu (Figure 1(a)), which is younger than Enkidu and the light terrain units (Figure 23(c)). Its model age ranges between ∼0.2 and ∼1.5 Ga (LDM; ±1.0 Ga) or less than ∼0.1 Ga (JCM). The light terrain of Region C spans a period between ∼3.61 Ga and ∼4.10 Ga (LDM; ±0.1–0.2 Ga) or ∼0.64 to ∼4.20 Ga (JCM). Within this range, the smooth light terrains ls generally have higher CSFDs than the grooved light terrain units lg. Whether this reflects older ages is questionable. A selective increase of the CSFD of the smooth terrain by bombardment with secondaries is only reasonable if the crater-forming event happened prior to the formation of the grooved terrain and after the formation of the smooth terrain. Enkidu may be the origin of secondary craters. The extensive secondary field of Enkidu

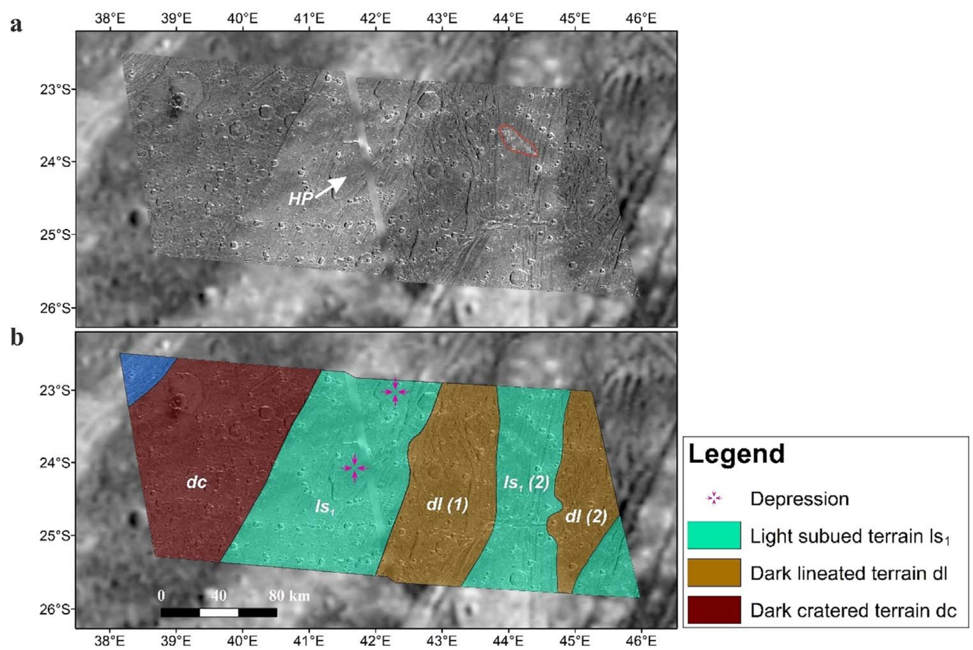

Figure 15. Region C/Harpagia Sulcus II: (a) SSI observation 28GSCALDRA01/02 indicating the location of HP. The red polygon represents an example of suspected secondary craters. (b) The associated geologic map produced following the mapping style of Collins et al. (2013).

Table 7
Measured CSFDs (N (10) and N (1)) for All Mapped Terrain Units in the Harpagia Sulcus II Region, Including LDM and JCM Age Estimates, Terrain Unit Areas, and the Number of Craters Counted

Region C	Terrain Unit	N (10) (km^{-2})	N (1) (km^{-2})	LDM (Ga)	JCM (Ga)	Area (km^2)	No. of Craters Counted
28GSCALDRA02 (Harpagia Sulcus II)	ls$_1$	$2.09 \times 10^{-4} \pm 2.26 \times 10^{-5}$	$2.36 \times 10^{-2} \pm 2.55 \times 10^{-3}$	$4.10^{+0.015}_{-0.017}$	$4.20^{+0.36}_{-1.59}$	10,725.9	174
	ls$_1$ (2)	$1.63 \times 10^{-4} \pm 4.17 \times 10^{-5}$	$1.84 \times 10^{-2} \pm 4.7 \times 10^{-3}$	$4.06^{+0.034}_{-0.037}$	$3.93^{+0.61}_{-1.73}$	5423.41	116
	dl (1)	$1.83 \times 10^{-4} \pm 4.67 \times 10^{-5}$	$2.06 \times 10^{-2} \pm 5.26 \times 10^{-3}$	$4.08^{+0.034}_{-0.037}$	$4.06^{+0.49}_{-1.68}$	6815.56	116
	dl (2)	$1.61 \times 10^{-4} \pm 3.81 \times 10^{-5}$	$1.82 \times 10^{-2} \pm 4.29 \times 10^{-3}$	$4.06^{+0.031}_{-0.037}$	$3.93^{+0.62}_{-1.73}$	3400.43	82
	dc	$3.94 \times 10^{-4} \pm 3.48 \times 10^{-5}$	$4.44 \times 10^{-2} \pm 3.92 \times 10^{-3}$	$4.19^{+0.012}_{-0.014}$	$4.52^{+0.04}_{-0.88}$	10,194.2	255

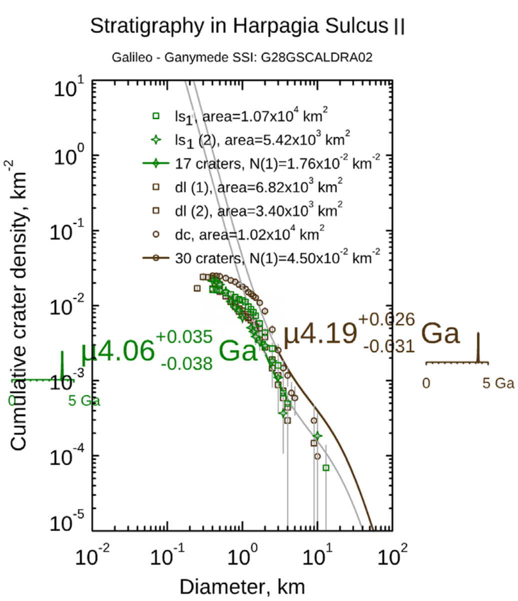

Figure 16. Comparison of the relative ages of the different terrain units from Harpagia Sulcus I (SSI observation 28GSCALDRA02) based on CSFDs. The plot displayed here represents ages derived from LDM. For ages based on JCM, refer to Table 7.

spans about 600 km around the crater, and, since our study regions lie within this field, it can potentially cause a bias in the counted primary craters. The dark terrain formation that belongs to Nicholson Regio happened between ∼4.05 and 4.19 Ga (LDM; ±0.1–0.2 Ga) or ∼3.80 to ∼4.52 Ga (JCM). To summarize, the time gap between the formation of the dark terrain units and the light terrains appears to be short using both chronologies.

Region D

In Region D, the youngest feature, Osiris crater (Figure 1(a)), has a model age of ∼0.5 to ∼1 Ga (LDM; ±1.0 Ga) or less than ∼0.1 Ga (JCM) (Figure 23(d)). The CSFD of Melkart crater is slightly lower than that of the light terrains, whose age corresponds to ∼3.63 Ga (LDM; ±0.1–0.2 Ga) or ∼1.5 Ga (JCM). Unlike Regions A, B, and C, the light terrains in region D have generally high CSFDs, which is similar to that of the dark terrain. In Erech Sulcus, as well as in Mummu and Sippar Sulci, no large differences in the CSFDs could be detected between the various light terrains and the dark terrains. As outlined before, secondary craters, likely radiating from the Osiris and Melkart craters, superposed the original CSFDs, and therefore they hampered a genuine/realistic age determination of the geological units.

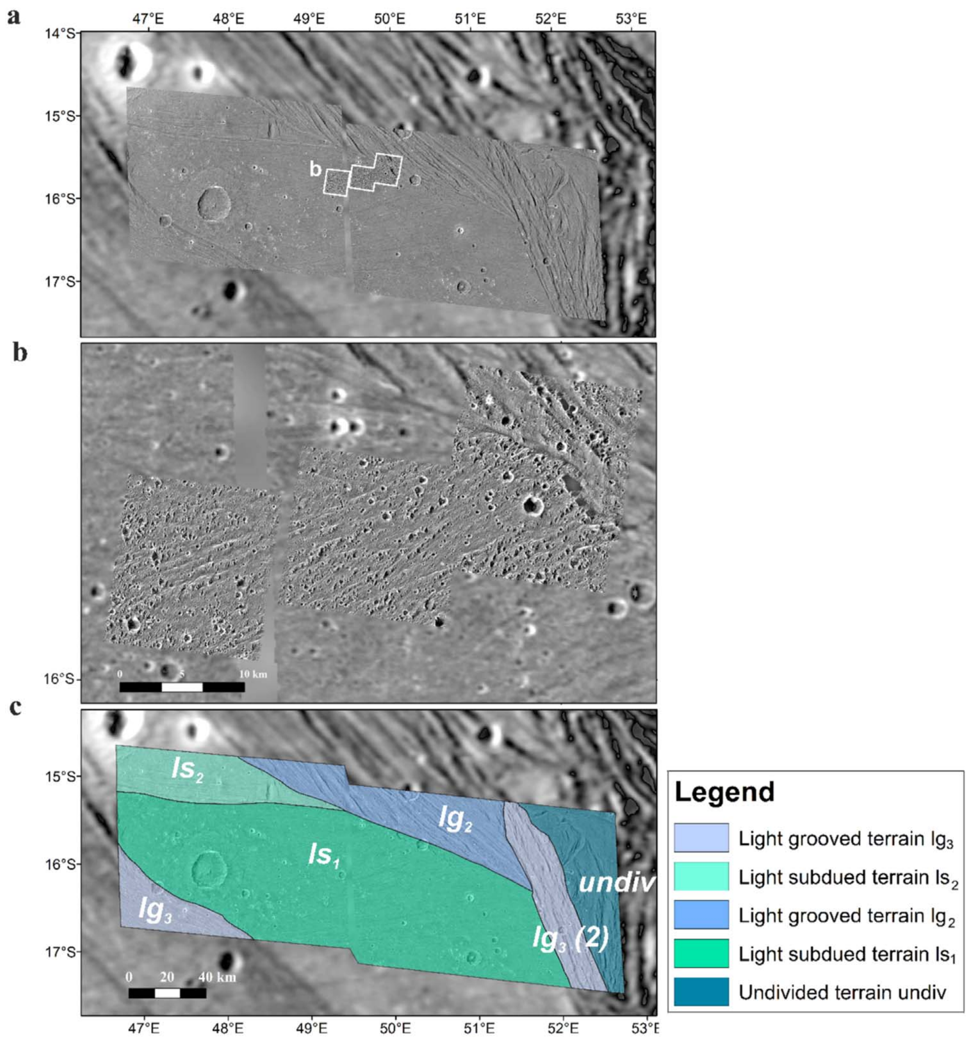

Figure 17. Region C/Harpagia Sulcus III: (a) SSI observation 28GSSMOOTH02; (b) the highest-resolution image sequence 28GSSMOOTH01, and (c) the associated geological map of panel (a) following the mapping style of Collins et al. (2013).

5.1. Summary of Results

First, from the above discussion about the relative age relationships of the different terrains, it is clear that the dc units feature higher CSFDs. Also, they possess comparatively higher AMAs than the light terrains and exhibit a similar age in all regions (Figure 23). Unlike the case of the light terrains, the ages estimated for the dark terrains from both models also equally suggest dc to have formed very early in Ganymede's evolution. This implies that they belong to the Nicholsonian era. But dc in Nippur and Philus Sulcus has a lower CSFD value like that of the light terrains. This is an exceptional case because dark terrain has usually undergone tectonic deformation, resulting in the presence of many fractures cutting through it and a large crater having strained to a great extent. The dl terrains have slightly lower CSFD values than dc and their values are similar to that of the light terrains. As a rule, dl is formed when dc undergoes intense fracturing.

Second, the nearest youngest impact craters belonging to the Gilgameshan era are considered in each study regions since they represent the latest prominent impact events and act as stratigraphic markers in these regions. They are found to have formed completely after the tectonic events forming the light terrains. So, their ages would lie above the ages of the light terrains. Also, their model ages in comparison with the model ages of the old dark terrains would help to derive the relative ages for the light terrains. A comparatively older impact crater from our study regions is Melkart, having a CSFD value of $2.80^{+0.49}_{-0.55} \times 10^{-5}$ km^{-2} and the youngest impact crater is Kittu having CSFD value of $8.67^{+13.4}_{-6.48} \times 10^{-7}$ km^{-2} (Figure 23). Except for Melkart and Enkidu, which have similar CSFDs compared to those of some light terrain units, other large craters such as Nergal, Kittu, and Osiris have lower CSFDs than all light terrains. Therefore, the young impact craters stand as a stratigraphic marker, in which the light terrain formation has ended before such impact events happened.

Furthermore, the model ages derived for the light terrains belonging to the Harpagian era are found to be more complicated than the model ages of the dark terrains and young impact craters. According to LDM, the ages of the different light terrains range between ∼3.6 Ga and ∼4 Ga. The ages given by this model are very old compared to JCM. The range infers that there is no large time gap between the formation periods of the different light terrains. In other words, the different light terrains formed simultaneously and/or subsequently one after the other. According to JCM, however, the ages of the different light terrains range between ∼0.7 Ga

Table 8
Measured CSFDs (N (10) and N (1)) for all Mapped Terrain Units in the Harpagia Sulcus III Region, Including LDM and JCM age Estimates, Terrain Unit area, and the Number of Craters Counted.

Region C	Terrain Unit	N (10) (km^{-2})	N (1) (km^{-2})	LDM (Ga)	JCM (Ga)	Area (km^2)	No. of Craters Counted
28GSSMOOTH02 (Harpagia Sulcus III)	lg_3	$1.66 \times 10^{-5} \pm 2.87 \times 10^{-6}$	$1.87 \times 10^{-3} \pm 3.23 \times 10^{-4}$	$3.68^{+0.032}_{-0.041}$	$0.84^{+1.24}_{-0.54}$	1303.16	51
	lg_3 (2)	$2.87 \times 10^{-5} \pm 1.64 \times 10^{-5}$	$3.23 \times 10^{-3} \pm 1.85 \times 10^{-3}$	$3.79^{+0.076}_{-0.11}$	$1.35^{+1.62}_{-0.84}$	1825.55	15
	lg_2	$1.23 \times 10^{-5} \pm 1.96 \times 10^{-6}$	$1.39 \times 10^{-3} \pm 2.21 \times 10^{-4}$	$3.61^{+0.034}_{-0.045}$	$0.64^{+1.02}_{-0.41}$	3107.27	62
	ls_1	$7.97 \times 10^{-5} \pm 3.02 \times 10^{-5}$, $1.93 \times 10^{-5} \pm 1.91 \times 10^{-6}$	$8.98 \times 10^{-3} \pm 3.4 \times 10^{-3}$, $2.18 \times 10^{-3} \pm 2.15 \times 10^{-4}$	$3.95^{+0.049}_{-0.057}$	$0.96^{+1.36}_{-0.62}$	13,832.8	404
				$3.71^{+0.012}_{-0.013}$	$2.83^{+1.48}_{-1.52}$		
	ls_2	$2.81 \times 10^{-5} \pm 2.98 \times 10^{-6}$	$3.16 \times 10^{-3} \pm 3.36 \times 10^{-4}$	$3.78^{+0.018}_{-0.020}$	$1.32^{+1.60}_{-0.83}$	2190.27	103
	undiv	$1.60 \times 10^{-5} \pm 2.17 \times 10^{-6}$	$1.80 \times 10^{-3} \pm 2.45 \times 10^{-4}$	$3.67^{+0.026}_{-0.032}$	$0.81^{+1.21}_{-0.52}$	2438.51	65

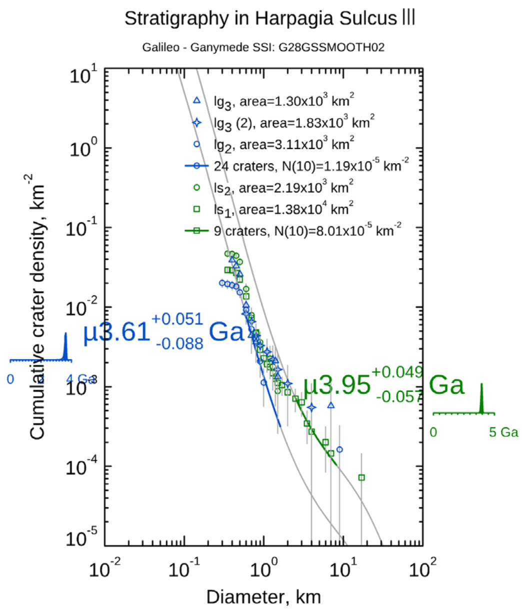

Figure 18. Comparison of relative ages of different terrain units from Harpagia Sulcus II (SSI observation 28GSSMOOTH02) based on CSFDs. The plot displayed here represents ages derived from LDM. For ages based on JCM, refer to Table 8.

and ∼4.3 Ga. The ages given by this model for most of the light terrains are much younger. This range implies that there is a very large time gap between the formation periods of the different light terrains. This means that the different light terrain formations could have taken place gradually and that the tectonic activities responsible for the light terrain formation have lasted over a long time, or several periods of tectonic activity occurred. Nevertheless, their ages when compared with the JCM ages of the dark terrain shows that the light terrain formation took place shortly after the dark terrain formation ended.

Finally, between all of the individual terrains investigated so far, we found more grooved and subdued terrains than irregular ones. The irregular terrains are mostly comparably old ones since they were cross-cut by adjacent terrain units. But an older li_1 not always exhibits higher CSFD values. For instance, the li_1 terrains in Mummu and Sippar Sulci shows lower CSFD values than the more lately formed terrains. In Regions A, B, and D we have a similar number of lately formed grooved and subdued terrains. In Harpagia Sulcus III, we found that the older ls_1 terrain, which is being cross-cut by adjacent terrains, has a higher CSFD value. Therefore, the CSFD values for most of the regions (Regions A, C, and D) do not always follow the same relative age relationships that we obtained from their cross-cutting relationships. But the CSFD values of the terrains in Arbela Sulcus follow the relative age relationships inferred from their cross-cutting relationships.

In general, in most of the regions, the ls terrain unit accumulated higher CSFDs than lg and li terrain units. The smoother the terrains are (with fewer grooves), the higher the CSFDs found on them are. This is in exception to Mummu and Sippar Sulci, where almost all the terrains are highly cratered and no relative age relationships could be obtained from the CSFD measurements alone. In regions like Nippur, Philus Sulcus, and Harpagia Sulcus I, the younger ls_3 terrains display higher CSFD values than the lg_2 and lg_3 terrains. If these ls_3 terrains had accumulated secondaries from large impact craters causing the CSFD to increase to higher values, then it remains unknown why the neighboring lg_3 and lg_2 have lower CSFDs than it. The possible reason behind this would be that the light grooved terrains may have undergone resurfacing activities while Ganymede was tectonically active. Besides, Ganymede's surface may have initially formed as smooth terrain (i.e., ls terrain), which later underwent faulting, resulting in the creation of the lg and li terrains. This could explain why the ls terrains have higher CSFD values than the lg and li terrains. Therefore, the light terrain on Ganymede would have undergone tectonic processes and evolved into morphologically different terrains from its initial formation until the moon's active stage. In addition, their complex cross-cutting relationships with each other point toward a complex tectonism and subsurface activities of Ganymede responsible for the formation of the morphologically different terrains.

6. Discussion

6.1. Stratigraphic Analysis of the Terrain Units in the Different Regions

In general, the stratigraphic relationships of the terrain units investigated in this study support the results of the earlier works of Patterson et al. (2010) and Collins et al. (2013). They showed that the dark cratered terrains are the geologically oldest and the light terrains are the relatively youngest terrains, whereas the dark lineated terrains and reticulate terrains have intermediate ages between them. Thus, a dark lineated terrain represents a dark cratered terrain with subsequent tectonic resurfacing (Pappalardo et al. 2004). The reticulate terrains examined in Mummu and Sippar Sulci show that they formed shortly before the light terrain formation had started, because they are being cross-cut by light terrain and have slightly higher CSFDs with respect to the light terrain. Therefore, our result supports earlier studies on reticulate terrains by Guest et al. (1988), Wilhelms (1997), Schenk et al. (2001), Patterson et al. (2010), and Collins et al. (2013).

In our study, we investigated whether the distances of the target areas relative to the apex could significantly influence our findings. For each of our study areas, we calculated the apex distance using the center of each Galileo SSI observation. Table 1 reports these distances (see the fifth column). Regions A, B, and D have distances ranging from approximately 80° to 110°, situated halfway between the apex and antapex. According to Xu et al. (2017), frequencies between a 80° and 110° apex distance differ by a factor of 1.5–2, which is comparable to the average measurement uncertainties in the cumulative frequencies for diameters of 1 km and 10 km. Consequently, we deduce that, in terms of apex distance, the frequencies and ages measured in these three regions are comparable from a stratigraphic perspective. The three study areas in Region C (Harpagia Sulcus I, II, and III) have a greater distance to the apex, ranging from 120° to 140°. On average, the cumulative frequencies in these areas are approximately 2 times lower than the frequency obtained in a unit at a 90° distance, similarly to the findings of Xu et al. (2017) for light terrains. Therefore, it is essential to consider that the cumulative frequencies measured in Harpagia Sulcus I to III, which are lower than the average frequencies in Regions A, B, or D, could actually indicate a similar age or even older than the units in Regions A, B, and D.

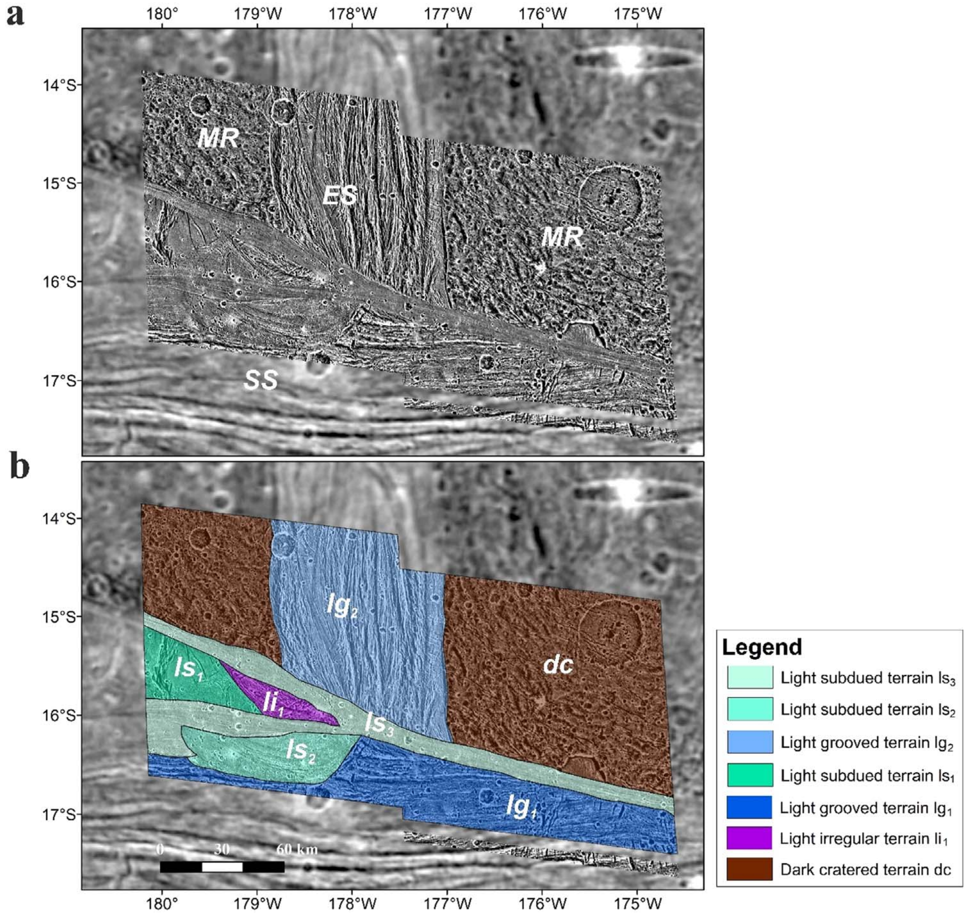

Figure 19. Region D/Erech Sulcus: (a) SSI observation G8GSERECH01 with the main surface features Erech Sulcus (ES), Sippar Sulcus (SS), and Marius Regio (MR) indicated and (b) the associated geologic map produced following the mapping style of Collins et al. (2013).

Table 9
Measured CSFDs (*N* (10) and *N* (1)) for All Mapped Terrain Units in the Erech Sulcus Region, Including LDM and JCM Age Estimates, Terrain Unit Areas, and the Number of Craters Counted.

Region D	Terrain Unit	N (10) (km^{-2})	N (1) (km^{-2})	LDM (Ga)	JCM (Ga)	Area (km^2)	No. of Craters Counted
G8GSERECH01 (Erech Sulcus)	ls_3	$7.52 \times 10^{-5} \pm 1.3 \times 10^{-5}$	$8.48 \times 10^{-3} \pm 1.46 \times 10^{-3}$	$3.94^{+0.024}_{-0.030}$	$2.74^{+1.53}_{-1.54}$	3101.21	54
	lg_2	$5.65 \times 10^{-5} \pm 1.45 \times 10^{-5}$	$6.37 \times 10^{-3} \pm 1.63 \times 10^{-3}$	$3.90^{+0.036}_{-0.040}$	$2.27^{+1.71}_{-1.33}$	6280.42	49
	ls_2	$7.90 \times 10^{-5} \pm 1.97 \times 10^{-5}$	$8.91 \times 10^{-3} \pm 2.22 \times 10^{-3}$	$3.95^{+0.034}_{-0.038}$	$2.82^{+1.49}_{-1.57}$	1476.20	39
	lg_1	$9.93 \times 10^{-5} \pm 1.93 \times 10^{-5}$	$1.12 \times 10^{-2} \pm 2.18 \times 10^{-3}$	$3.99^{+0.027}_{-0.033}$	$3.21^{+1.23}_{-1.69}$	4550.63	106
	ls_1	$7.39 \times 10^{-5} \pm 2.02 \times 10^{-5}$	$8.33 \times 10^{-3} \pm 2.28 \times 10^{-3}$	$3.94^{+0.037}_{-0.041}$	$2.71^{+1.55}_{-1.52}$	1145.05	55
	li_1	$7.56 \times 10^{-5} \pm 2.87 \times 10^{-5}$	$8.52 \times 10^{-3} \pm 3.23 \times 10^{-3}$	$3.95^{+0.049}_{-0.057}$	$2.74^{+1.53}_{-1.54}$	488.008	23
	dc	$1.49 \times 10^{-4} \pm 1.39 \times 10^{-5}$	$1.68 \times 10^{-2} \pm 1.57 \times 10^{-3}$	$4.05^{+0.013}_{-0.015}$	$3.82^{+0.72}_{-1.75}$	12,248.7	298

Comparing the different study regions, we could find a consistent relative age relationship between the light terrains lg, ls, and li. In some of the selected areas, the smooth, light subdued terrain forms the youngest stratigraphic unit, which indicates tectonic extension in spreading mode.

We have not observed a significant variation in the CSFDs (and, consequently, the absolute ages derived from both models) with respect to an increment in area for any specific type of terrain (for a more detailed explanation, please refer to Appendix B). Due to the cross-cutting relationships of the geological units, a relative chronology could be derived from geological mapping. This is not always congruent with the age determination derived from the CSFD measurement. In the following, we are going to explain both such deviations and the possible reasons for their occurrence. First, we defined that the degree of matching between both methods is expressed in percentages. For example, if five different chronological units are inferred from mapping, matching is 80% when four of the five units show the same sequence in crater counting. In brief, in Byblus Sulcus (Region A) the two light terrains are of similar age from the crater counts while lg_3 is younger than lg_2 from the cross-cutting relationships. In the Nippur and Philus Sulcus region, the terrains of Nippur Sulcus have an older age than Philus Sulcus from the crater counts. This is in contrast to the mapping result of this area where Nippur Sulcus cross-cuts Philus Sulcus. This may indicate a short period between the

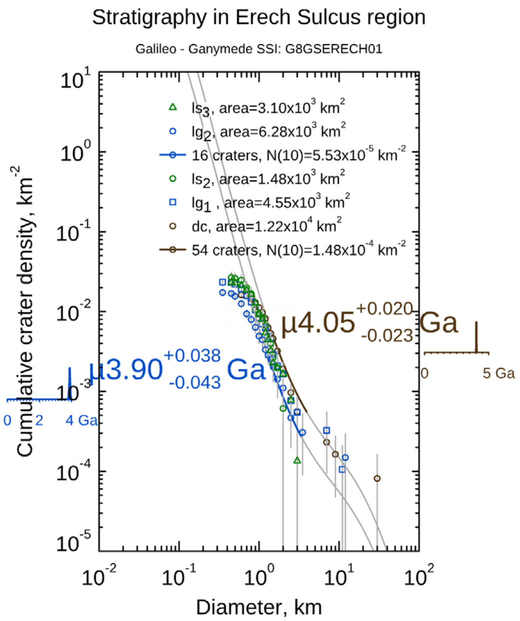

Figure 20. Comparison of the relative ages of the different terrain units from Erech Sulcus (SSI observation G8GSERECH01) based on CSFDs. The plot displayed here represents ages derived from LDM. For ages based on JCM, refer to Table 9.

formation of these terrains. To conclude, the matching in Region A between geological mapping and crater counting is 60%. In the case of Region B (Arbela Sulcus), we found that the age relationship of the two light terrains and two dark terrains agrees with the relative age inferred from the cross-cutting relationships. The matching is 80%. In Region C, the light subdued terrains have a comparatively higher age than the light grooved terrains. In these regions, we hypothesized that the light subdued terrains formed earlier and subsequent faulting could have developed into light grooved terrains at a later stage. The region constituting Harpagia Sulcus II (28GSCALDRA02) is inferred to be older based on its cross-cutting relationships and CSFDs compared to the regions containing Harpagia Sulcus III (28GSSMOOTH02) and Harpagia Sulcus I (28GSBRTDRK02). The overall matching of Region C is 60%. In Region D, the terrains are highly contaminated by secondary craters from the Osiris and Melkart craters. There is no significant difference of the crater-counting-derived ages between the studied terrains, but the related cross-cutting relationships clearly suggest subsequent formations. Nevertheless, a saturation of craters or the short period between the formation of different terrains could be possible reasons for such a disagreement. The derived CSFDs and ages from such regions should be taken with caution. Due to the superposition with secondaries the matching between the relative chronology derived from geological mapping and crater counting is only 40%.

6.2. Discrepancies of Crater Chronology Models

The usage of JCM and the obtained age interpretation is difficult in older regions since this model uses the present cometary fluxes to infer the dynamical motion of these bodies in the past. Therefore, such extrapolation results in ages older than the solar system caused by highly uncertain conditions in a planetary migration period prior to ∼3.6 Gyr with a possible exponentially decaying impactor flux versus mainly constant flux.

On the contrary, LDM is based on a lunar-like model with its assumption that the craters on Ganymede were mainly created by asteroidal impacts, like those on the Moon. Although this might be unrealistic for the bombarding flux on Ganymede, recent studies (Bottke et al. 2022) supported a similar SFD between comets and asteroids, i.e., both groups of impactors represent a collisionally evolved impactor family showing similar crater distributions, such as, e.g., asteroidal impacts on the Moon. Possibly different impactor families existed through time with preferentially asteroids prior to ∼3.6 Gyr and preferentially JFCs at later time to the present (G. Neukum, personal communication; Schenk et al. 2004). However, the projectile SFD can be similar; the result of an impact (i.e., the crater SFD) can be different due to the distinct surfaces of the Moon and Ganymede and the variation in impact velocities.

6.3. Formation Scenarios for the Light Terrain on Ganymede

The variations of the SFDs of impact craters on different terrains are not always coherent with geological observations. The moderate variations of CSFDs suggest that the range of formation ages is not large. Knowledge of the absolute ages of the light terrain units, however, is essential to solve which processes or conditions could be responsible for the tectonic activity in Ganymede's past and the light terrain formation. The following formation scenarios have been discussed in recent studies.

(A) Global Volume Expansion Through Internal Differentiation

A global expansion through differentiation early in Ganymede's history (Squyres 1980; Schubert et al. 1981; Zuber & Parmentier 1984; Mueller & McKinnon 1988; Bland et al. 2009) would be most likely a continuous process that is associated with a continuous formation of the different light terrains. So different light terrains were formed via extension of the lithosphere once differentiation started. Under such circumstances, the light terrains would have likely formed shortly one after the other or contemporarily with the tectonic style (grooved or subdued) depending on the local surface properties. Light terrain formation might have stopped once the differentiation process and associated thermal expansion has been completed.

Light terrains could have already started developing through lithospheric extension, when the Ganymede surface was made up by a thin ice shell (Nimmo 2004), as evidenced from its low thermal gradient at present and high thermal gradient in the past (Pappalardo et al. 2004). Although the depth to diameter ratios of craters that formed after the grooved terrains suggest an ice shell thickness of at least 60 km (Schenk 2002), the ancient palimpsests suggest instead a much lower ice shell thickness in the past (Bland et al. 2009).

Our results support that the light terrains started to form soon after dark terrain formation. However, although, using LDM, the derived ages imply a light terrain formation in a short period early in Ganymede's evolution, when applying JCM, an unrealistically large time span is often observed because of the model's large overlapping error bars.

(B) Laplace Resonance and Orbital Recession—Tidal Heating

It is estimated that Ganymede's eccentricity (presently $e = 0.0013$) is currently too low to cause prominent tidal

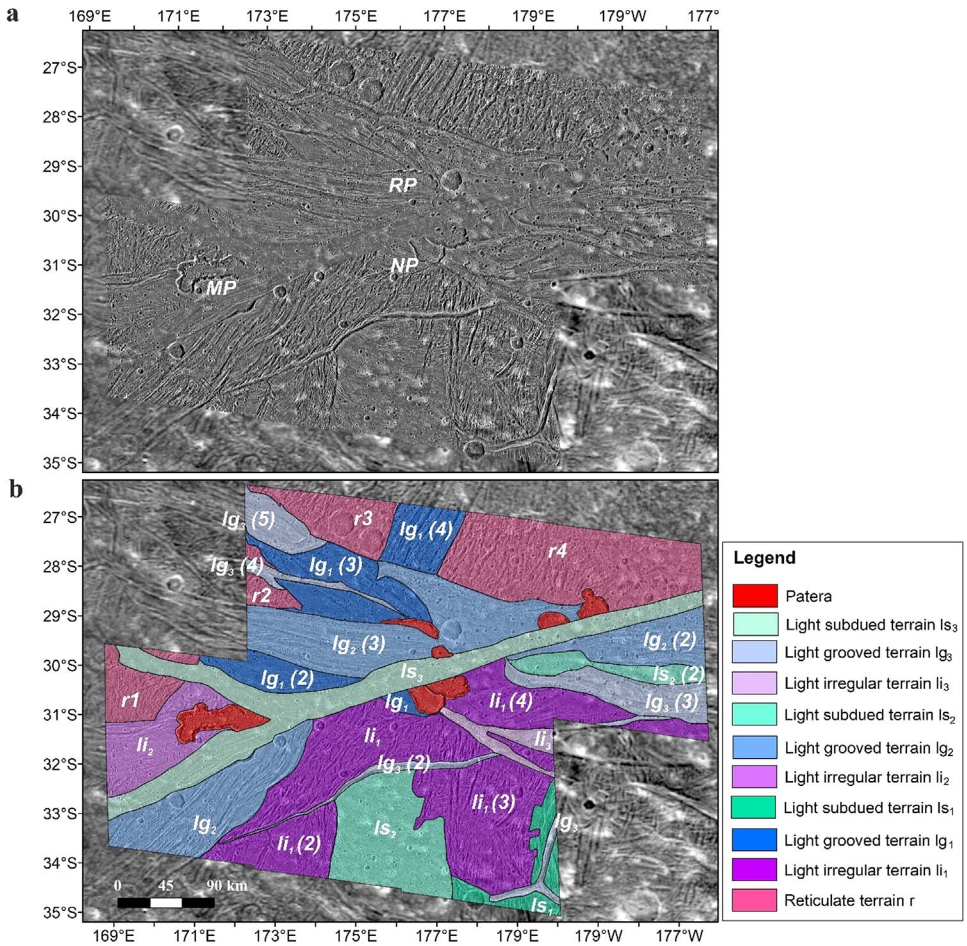

Figure 21. Region D/Mummu and Sippar Sulci: (a) SSI observation sequence G8GSCALDRA01 with the location of Musa (MP), Natrum (NP), and Rum Patera (RP) indicated and (b) the associated geologic map produced following the mapping style of Collins et al. (2013).

heating effects (Mckinnon & Parmentier 1986) and subsequent tectonic resurfacing activities (Bland et al. 2009). Nevertheless, an orbital eccentricity originated by periods of Laplace-like resonances with Europa and Io in the past could have triggered periods of tidal heating and internal melting, which, in turn, would have led to enhanced differentiation and geologic activity (Showman et al. 1997). In such a scenario, the light terrains could have resulted from Ganymede's past high eccentricity and higher tidal dissipation (Showman & Malhotra 1997), if the Laplace resonance has a major effect in generating tectonism.

The CSFDs of different terrain units show that the period between the end of dark terrain formation and beginning of light terrain formation is generally small if LDM is used. In this case, eccentricity-induced tidal heating would have taken place soon after dark terrain formation. The morphological characteristics distinguishing light terrain into grooved, subdued, and irregular terrains could have reflected changes in the internal dynamics of the outer ice shell. The reason for such changes, as suggested by Choblet et al. (2017), is the chemical transfer of melt or liquid water from the surface of a silicate core or high-pressure ice mantle layer. Such transport through heat pipes could have taken place up to at least 500 Myr ago and may have affected the history of ocean crystallization. This theory is contradicted by the surface ages estimated by using LDM, but is supported by JCM because this model assumes ages of $\sim$ 1 Ga for some terrains and suggest larger formation period for light terrains.

(C) Nonsynchronous Rotation

The tectonic activity in Ganymede's past could have taken place in a time of nonsynchronous rotation. At present Ganymede's synodic rotation around Jupiter is synchronous. Studies, however, showed that Ganymede could have rotated nonsynchronously in the past (Nimmo & Pappalardo 2004; Cameron et al. 2019, 2020). Past nonsynchronous motion could have produced diurnal and tidal stresses, which would have induced shear failure giving rise to strike-slip faulting within light terrains (Cameron et al. 2019). If nonsynchronous rotation is the cause of the formation of the light terrain then the time of completion of the light terrain would help to constrain the time of the gradual transition toward synchronous rotation. If we consider nonsynchronous rotation to represent the main reason responsible for light terrain formation, then LDM is somewhat unlikely as it suggests a short formation period for light terrains. In contrast, JCM, which implies a rather long formation for light terrain formation, would better fit to such a scenario. In that case, light terrain formation has ended $\sim$1 Ga ago and Ganymede would have successively entered a synchronous state.

(D) Large Impacts in Ganymede's *Early History*

Could the formation of the light terrain have been initiated by intense impact cratering? Large impact basins, like Gilgamesh basin (62.8° S, 125° W; 600 km diameter) on

Table 10
Measured CSFDs (N (10) and N (1)) for All Mapped Terrain Units in the Mummu and Sippar Sulcus Region, Including LDM and JCM Age Estimates, Terrain Unit Areas, and the Number of Craters Counted.

Region D	Terrain Unit	N (10) (km^{-2})	N (1) (km^{-2})	LDM (Ga)	JCM (Ga)	Area (km^2)	No. of Craters Counted
G8GSCALDRA01 (Mummu and Sippar Sulcus)	lg$_3$	$4.75 \times 10^{-5} \pm 1.3 \times 10^{-5}$	$5.35 \times 10^{-3} \pm 1.47 \times 10^{-3}$	$3.87^{+0.039}_{-0.044}$	$2.00^{+1.75}_{-1.20}$	869.719	20
	lg$_3$(2)	$1.05 \times 10^{-4} \pm 3.53 \times 10^{-5}$	$1.18 \times 10^{-2} \pm 3.98 \times 10^{-3}$	$4.00^{+0.044}_{-0.050}$	$3.29^{+1.17}_{-1.71}$	1225.49	21
	lg$_3$(3)	$1.99 \times 10^{-4} \pm 2.92 \times 10^{-5}$	$2.24 \times 10^{-2} \pm 3.29 \times 10^{-3}$	$4.09^{+0.020}_{-0.024}$	$4.15^{+0.40}_{-1.63}$	4917.89	165
	lg$_3$(4)	$5.23 \times 10^{-5} \pm 7.42 \times 10_{-6}$	$5.90 \times 10^{-2} \pm 8.36 \times 10^{-4}$	$3.89^{+0.021}_{-0.025}$	$2.14^{+1.74}_{-1.28}$	2489.43	43
	lg$_3$(5)	$1.06 \times 10^{-4} \pm 3.59 \times 10^{-4}$	$1.19 \times 10^{-2} \pm 4.05 \times 10^{-3}$	$4.00^{+0.055}_{-0.064}$	$3.31^{+1.16}_{-1.71}$	998.227	75
	ls$_3$	$9.67 \times 10^{-5} \pm 7.9 \times 10^{-6}$	$1.09 \times 10^{-2} \pm 8.91 \times 10^{-4}$	$3.98^{+0.012}_{-0.013}$	$3.16^{+1.27}_{-1.68}$	13,428.0	355
	li$_3$	$2.41 \times 10^{-4} \pm 5.55 \times 10^{-5}$	$2.72 \times 10^{-2} \pm 6.26 \times 10^{-3}$	$4.12^{+0.033}_{-0.035}$	$4.32^{+0.24}_{-1.47}$	1930	41
	lg$_2$	$9.67 \times 10^{-5} \pm 9.93 \times 10^{-6}$	$1.09 \times 10^{-2} \pm 1.12 \times 10^{-3}$	$3.98^{+0.015}_{-0.017}$	$3.16^{+1.27}_{-1.68}$	8894.42	238
	lg$_2$(2)	$2.60 \times 10^{-4} \pm 4.39 \times 10^{-5}$	$2.93 \times 10^{-2} \pm 4.95 \times 10^{-3}$	$4.13^{+0.023}_{-0.027}$	$4.37^{+0.19}_{-1.29}$	4976.44	130
	lg$_2$(3)	$7.03 \times 10^{-5} \pm 7.04 \times 10^{-6}$	$7.93 \times 10^{-3} \pm 7.94 \times 10^{-4}$	$3.93^{+0.015}_{-0.017}$	$2.62^{+1.59}_{-1.49}$	8044.88	250
	lg$_2$(4)	$1.50 \times 10^{-4} \pm 2.03 \times 10^{-5}$	$1.69 \times 10^{-2} \pm 2.29 \times 10^{-3}$	$4.05^{+0.019}_{-0.022}$	$3.83^{+0.71}_{-1.75}$	5955.69	201
	ls$_2$	$2.39 \times 10^{-4} \pm 7.03 \times 10^{-5}$	$2.70 \times 10^{-2} \pm 7.92 \times 10^{-3}$	$4.12^{+0.038}_{-0.042}$	$4.31^{+0.25}_{-1.48}$	4709.82	103
	ls$_2$(2)	$2.00 \times 10^{-4} \pm 3.1 \times 10^{-5}$	$2.26 \times 10^{-2} \pm 3.49 \times 10^{-3}$	$4.09^{+0.021}_{-0.025}$	$4.17^{+0.39}_{-1.62}$	2637.59	94
	li$_2$	$1.21 \times 10^{-4} \pm 1.3 \times 10^{-5}$	$1.36 \times 10^{-2} \pm 1.47 \times 10^{-3}$	$4.02^{+0.015}_{-0.017}$	$3.50^{+1.00}_{-1.74}$	5626.47	164
	lg$_1$	$3.26 \times 10^{-5} \pm 1.12 \times 10^{-5}$	$3.68 \times 10^{-3} \pm 1.26 \times 10^{-3}$	$3.81^{+0.049}_{-0.058}$	$1.50^{+1.68}_{-0.93}$	495.831	88
	lg$_1$(2)	$6.97 \times 10^{-5} \pm 1.51 \times 10^{-5}$	$7.86 \times 10^{-3} \pm 1.7 \times 10^{-3}$	$3.93^{+0.030}_{-0.039}$	$2.61^{+1.59}_{-1.48}$	2928.20	270
	lg$_1$(3)	$1.10 \times 10^{-4} \pm 1.03 \times 10^{-5}$	$1.24 \times 10^{-2} \pm 1.16 \times 10^{-3}$	$4.00^{+0.014}_{-0.015}$	$3.37^{+1.11}_{-1.72}$	6647.43	124
	lg$_1$(4)	$1.38 \times 10^{-4} \pm 1.91 \times 10^{-5}$	$1.56 \times 10^{-2} \pm 2.15 \times 10^{-3}$	$4.04^{+0.019}_{-0.022}$	$3.71^{+0.82}_{-1.76}$	3524.41	13
	ls$_1$	$8.20 \times 10^{-5} \pm 1.53 \times 10^{-5}$	$9.25 \times 10^{-3} \pm 1.73 \times 10^{-3}$	$3.96^{+0.026}_{-0.032}$	$2.88^{+1.45}_{-1.59}$	2954.11	86
	li$_1$	$4.50 \times 10^{-5} \pm 8.46 \times 10^{-6}$	$5.07 \times 10^{-3} \pm 9.54 \times 10^{-4}$	$3.86^{+0.028}_{-0.035}$	$1.92^{+1.76}_{-1.16}$	10,748.0	134
	li$_1$(2)	$5.51 \times 10^{-5} \pm 9.85 \times 10^{-6}$	$6.21 \times 10^{-3} \pm 1.11 \times 10^{-3}$	$3.90^{+0.026}_{-0.032}$	$2.23^{+1.72}_{-1.32}$	4784.35	168
	li$_1$(3)	$6.69 \times 10^{-5} \pm 7.33 \times 10^{-6}$	$7.54 \times 10^{-3} \pm 8.26 \times 10^{-4}$	$3.93^{+0.016}_{-0.018}$	$2.54^{+1.62}_{-1.46}$	10,973.1	70
	li$_1$(4)	$1.52 \times 10^{-4} \pm 1.69 \times 10^{-5}$	$1.71 \times 10^{-2} \pm 1.91 \times 10^{-3}$	$4.05^{+0.016}_{-0.018}$	$3.84^{+0.70}_{-1.74}$	6707.67	190
	r	$6.96 \times 10^{-5} \pm 9.58 \times 10^{-6}$	$7.85 \times 10^{-3} \pm 1.08 \times 10^{-3}$	$3.93^{+0.020}_{-0.023}$	$2.61^{+1.59}_{-1.48}$	3484.79	95
	r (2)	$7.55 \times 10^{-5} \pm 2.0 \times 10^{-5}$	$8.51 \times 10^{-3} \pm 2.25 \times 10^{-3}$	$3.94^{+0.036}_{-0.040}$	$2.74^{+1.53}_{-1.54}$	1288.93	34
	r (3)	$5.94 \times 10^{-5} \pm 1.69 \times 10^{-5}$	$6.70 \times 10^{-3} \pm 1.9 \times 10^{-3}$	$3.91^{+0.039}_{-0.044}$	$2.35^{+1.69}_{-1.37}$	616.277	120
	r (4)	$1.20 \times 10^{-4} \pm 1.2 \times 10^{-5}$	$1.35 \times 10^{-2} \pm 1.35 \times 10^{-3}$	$4.02^{+0.014}_{-0.016}$	$3.50^{+1.00}_{-1.74}$	10,948.2	285

Ganymede, are believed to have been formed early in the history of Ganymede, likely during the light terrain formation, when there was an intense bombardment by large projectiles, whose diameters were several tens of kilometers. Gilgamesh basin was emplaced into the light terrain at a later time than the degraded basins in the dark terrain (Schenk et al. 2004). These older impact events could have generated significant thermal anomalies in the mantle. The heat generated could alter the mantle's buoyancy enough to create upwellings and to drive tectonic activity. The effect would be stronger if Ganymede had an uneven thickness of its lithosphere during that time. Large impacts could have also added heat to the differentiation process. Moreover, large impact events could cause the onset of synchronous rotation. According to Murchie & Head's (1986) findings, the large impacts led to a global reorientation of Ganymede's rotational axis by approximately 15°. However, observing impact craters on Ganymede's neighbor Callisto raises doubt whether large impact events can trigger tectonism of light terrains. Callisto is probably a partially differentiated body (e.g., Sohl et al. 2002; Nagel et al. 2004), having a heavily cratered surface and containing the largest multiring impact basin in the solar system, Valhalla. However, it does not have any tectonically resurfaced terrains.

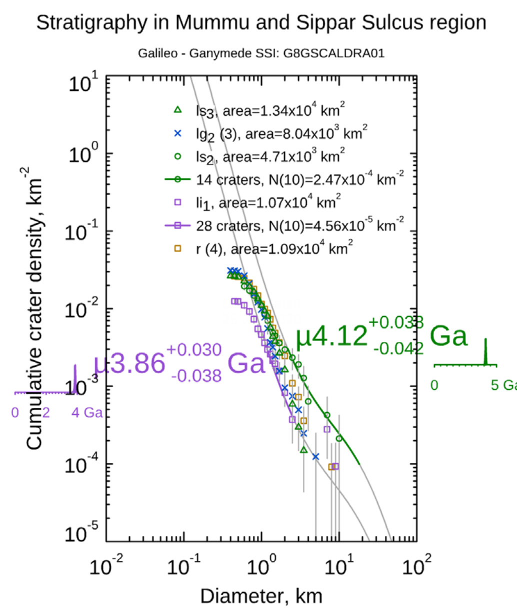

Figure 22. Comparison of the relative ages of the different terrain units from Mummu and Sippar Sulcus (SSI observation G8GSCALDRA01) based on CSFDs. The plot displayed here represents ages derived from LDM. For ages based on JCM, refer to Table 10.

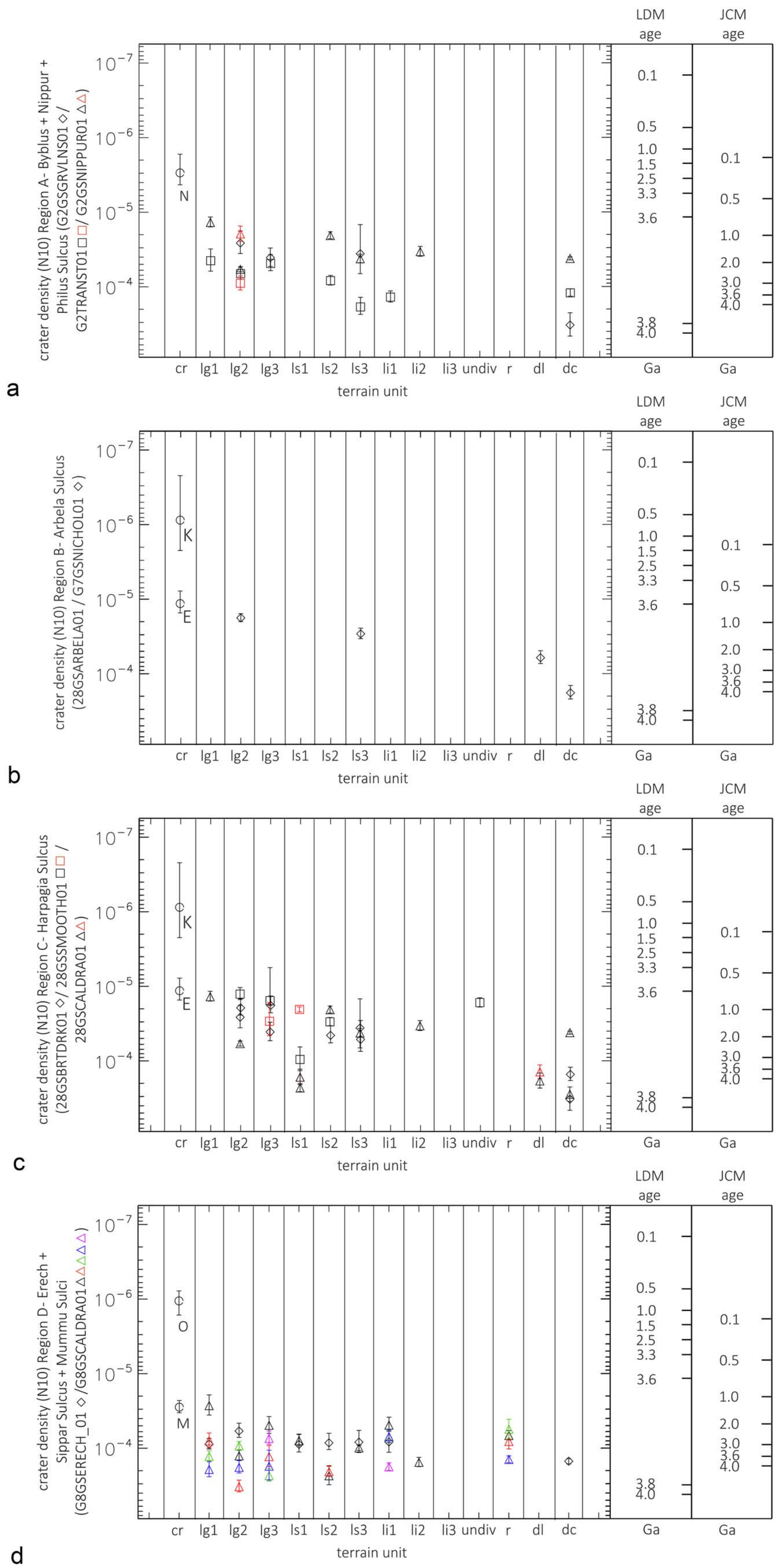

Figure 23. N (10) values derived for Regions (a) A, (b) B, (c) C, and (d) D. Please note that the N (10) values derived for fresh impact craters (cr) Kittu (K) and Enkidu (E), which are located near Regions B and C as well as Melkart (M) and Osiris (O), located near Region D, have been included as stratigraphic markers for the youngest period in the specific region. Also, note that different colors indicate various facies of a particular type of terrain.

7. Conclusions

We analyzed selected regions on Ganymede for which high-resolution remote sensing data are available. The combination of geologic mapping and CSFD measurements was a useful tool to explore the stratigraphic relationships of each investigated individual terrain unit in the studied regions. However, we often found a mismatch in the relative ages derived from cross-cutting relationships and crater statistics. Dark cratered terrains are found to be the oldest terrains, and light terrains are the youngest ones, whereas the dark lineated and reticulate terrains have intermediate ages, all of which agree with earlier studies. Light subdued terrains from the sub-Jovian hemisphere are older and those from the anti-Jovian hemisphere are younger. Tectonic resurfacing of the dark cratered terrains has led to the formation of dark lineated terrains. Prolonged tectonic resurfacing in the form of normal and strike-slip faulting gradationally has transformed the dark lineated terrain into new light terrains. The early stage of evolution of Ganymede is represented by dark cratered terrains, which are simply densely cratered and lacking lineaments. Its intermediate stage (when dark lineated terrains have started to evolve) is recorded by lineaments that are mostly widely spaced. The morphology of light grooved, light subdued, and light irregular terrains represents lately formed geological units within which the light irregular terrains are usually cross-cut by the light grooved and light subdued terrains. Younger light subdued terrains appear as narrower stripes, while older light subdued terrains appear as broader areas. In most cases, light grooved and light subdued terrains are found adjacent to each other. The formation of light grooved terrains can occur via extensive faulting within light subdued terrains. Therefore, a clear understanding of overall tectonic processes would be possible with wider coverage and better resolution of images and digital terrain models.

The two chronology models, LDM and JCM, correlate crater statistics with absolute ages. Both models lead to considerably different results. On one hand, according to LDM, the age derived for light terrain units (~3.6 Ga–4 Ga) is not much younger than the ancient dark terrains (~3.7 Ga–4.2 Ga). On the other hand, JCM-derived ages point to a longer formation period for light terrain units (~0.7 Ga to >4 Ga), which ended around 1 Ga ago, unlike the case of dark terrain (~3.5 to >4 Ga). Based on the CSFDs and the models, light terrain formation may have begun soon after dark terrain formation, with a time gap of ~0.2 Ga. However, as shown in this study, a complete understanding is far from being reached, due to the limits of the chronology models and the currently available restricted spatial resolution of Ganymede's surface. In addition to the significant differences in the model ages of the light terrain units, the estimated errors of both models are often too large to distinguish the ages between individual tectonic units of the light terrains. Therefore, improvements of these models are necessary. Updated chronologies should enable us to constrain the errors through a better description of how and when the planets changed their orbits in the past.

This study supports the JUICE mission. Particularly, the images acquired by the JANUS camera will enable thorough analyses of Ganymede's entire surface at unprecedented spatial resolutions and thus to investigate further and comprehend its relative and/or geologic age, tectonic processes, and relationships to its complex internal dynamics. Nevertheless, resolving model age-related issues on Ganymede (and the other icy moons) in the long-term future requires the collection of samples at landing sites to obtain absolute radiometric ages accurately. The optimal landing site for calibrating CSFDs with radiometric ages would be located in light terrain areas with minimal saturation due to craters, while avoiding large ray crater strewn fields.

Acknowledgments

We acknowledge the support of the DLR-DAAD PhD fellowship from the German Aerospace Center and the German Academic Exchange Service. We thank the editor, Edgard G. Rivera-Valentín, and two anonymous reviewers for their detailed comments and suggestions, which greatly contributed to the improvement of this manuscript.

Appendix A
CSFDs and Ages

A.1. CSFDs and Surface Ages

A.1.1. The Crater PF Polynomial of the Moon and Ganymede

As described in Section 3.2.2, polynomials of eleventh degree were adopted to fit the crater PF of a planet, satellite, or asteroid (e.g., Neukum & Ivanov 1994; Neukum et al. 2001; Werner & Ivanov 2015; Hiesinger et al. 2016). The PF of Ganymede is derived from the lunar PF, as shown in Figure 2 (regular section). This polynomial can fit measured CSFDs.

At small crater sizes (less than ~1 km), the lunar PF (and any lunar-derived PF) has a cumulative slope of ~−3. For craters larger than several kilometers to the largest sizes of 100s of kilometers, the slope changes between ~−3 and ~−1. This characteristic shape reflects the shape of the impactor SFD, derived from collisional evolution of these bodies with time (e.g., Ivanov et al. 2002). For inner solar system bodies, the correlation of CSFDs with the SFDs of asteroids that created the majority of craters is straightforward (e.g., Neukum & Ivanov 1994; Neukum et al. 2001; Ivanov et al. 2002; Werner & Ivanov 2015).

The Ganymede PF and its polynomial coefficients (Table A1) is obtained by a lateral shift of the lunar PF in log(D) (Section 3.2.2). This empirical method, however, is subjective and dependent of the interpreter: the lunar PF is shifted in log(D) until a specific Ganymede PF is found which best fits the CSFDs (e.g., Neukum et al. 1998). Similarly, the same methodology was applied to derive the PFs for Europa and Callisto (Neukum et al. 1998).

Although it is not explicitly said, such a shift of the PF is related to the specific impact condition of each body, for example the (average) impact velocity or the (average) frequency of impactors. A derivation of a Ganymede PF from crater scaling laws, like for Mars , is possible but this did not produce good results because of many unknowns in the crater scaling parameters.

Using a single PF polynomial for CSFDs measured in surface units of different ages tacitly assumes that the PF did not change its shape over time. Whether a PF is time independent is subject to debate, however. Several groups of investigators concluded from their measurements of terrestrial planets that the shape has changed with time due to a change in the impactor SFD (e.g., Strom et al. 2005, 2018; Kirchoff et al. 2022 and references therein). Other studies supported instead that any changes are within a factor of, or lower than, 2, and

Table A1
Coefficients of the Ganymede PF Polynomial in Comparison with the Lunar PF

Coefficient a_k	Ganymede PF	Lunar PF
a_0	−3.181	−2.5339
a_1	−3.2491	−3.6269
a_2	1.0307	0.4366
a_3	0.6933	0.7935
a_4	−0.2916	0.0865
a_5	−0.3061	−0.2648
a_6	0.0171	−0.0664
a_7	0.0533	0.0379
a_8	4.018×10^{-3}	0.0106
a_9	3.43×10^{-3}	-2.25×10^{-3}
a_{10}	4.065×10^{-4}	5.18×10^{-4}
a_{11}	3.97×10^{-5}	3.97×10^{-5}

Note. The Ganymede PF is from Neukum et al. (1998) and the lunar PF is from Neukum & Ivanov (1994).

therefore an eventual variation in time of the PF would not have affected the inferred age in comparison to other errors (e.g., Neukum et al. 2001).

The PF polynomial coefficients listed in Table A1 (Neukum & Ivanov 1994; Neukum et al. 2001) are used to calculate the cumulative frequency N_{cum} for a crater equal to, or larger than, a diameter D (in km) according to:

$$\log N_{\mathrm{cum}}(D) = \sum_{k=0}^{k=11} a_k \cdot [\log (D)]^k$$

.The lunar polynomial is valid in the diameter range of 10 m–300 km (Neukum & Ivanov 1994; Neukum et al. 2001). The term a_0 reflects the time dependence of the measured CSFD. For the lunar PF, the value $a_0 = -2.5339$ (similarly $a_0 = -3.4181$ for Ganymede) is correlated to a unit which is 1 Ga old in the LDM chronology (e.g., Neukum & Ivanov 1994). By shifting (fitting) the PF vertically in $\log(N_{\mathrm{cum}})$ to a CSFD, the relative age of a unit can be determined by changing the term a_0 alone, holding the values a_1 to a_{11} fixed because of the (assumed) time-independent CSFD polynomial. This procedure is described in the following section.

A.1.2. Derivation of Surface Ages from Crater Counts

A.1.2.1. The Software Tool Craterstats 2.0

We used ESRI/ArcGIS to map geologic units and to carry out crater counts. The toolbar CraterTools is an ArcGIS plug-in specifically developed for crater measurements, and provided by the Planetology Group at the Free University of Berlin (Kneissl et al. 2011).[3] In this study, we preferentially used images or mosaics in conformal map projections in which craters are represented as circles. The toolbar, however, is independent of map projections and accounts for any distortions caused by different map types (Kneissl et al. 2011). Two ArcGIS shape files are created, one for the area, another for the craters. After a measurement has been completed, the craters are exported into a spatial crater count (scc) file. Since a significant fraction of a crater can lie outside the measurement area and since large craters tend to obliterate smaller craters, several improved methods of the crater-counting technique have been developed for such cases (Kneissl et al. 2015, 2016; Riedel et al. 2018): (1) the traditional crater-counting approach takes only those craters into account whose centers lie within the measurement area boundary; (2) the buffered crater-counting approach also uses the fractions of those craters whose rims overlap the area boundary but whose centers lie outside the measurement area; the measurement area is enlarged by a buffer size of at least one crater radius for each one of these craters; (3) on densely cratered surfaces the impacts of large craters cause a depletion in small preexisting craters which affect the shape of the measured distribution; this can be corrected by the nonsparseness approach, removing the crater and ejecta area emplaced by the most pristine large impact craters, specified in an average obliteration factor; and last (4) the buffered nonsparseness approach which combines methods (2) and (3) (see detailed descriptions of all four methods in Kneissl et al. 2015, 2016; Riedel et al. 2018). Since the measurements presented in this study were carried out on high-resolution images in a comparably small diameter range (in general <10 km), we selected the buffered crater-counting approach.

Following the recommendations given by the Crater Analysis Techniques Working Group (1979; Arvidson et al. 1979), CSFDs—and, similarly, projectile SFDs—are plotted in diagrams with double-logarithmic (base 10) axes at the same scale, with the logarithm of crater frequency per square kilometer versus the logarithm of crater diameter in kilometers. Several plotting techniques can be used, i.e., (a) cumulative, (b) differential, and (c) relative crater size–frequency. The analysis and age dating of crater size–frequency measurements are performed in the separate software tool, craterstats 2.0. This software, provided freely by the Planetology group at the Free University of Berlin (Michael & Neukum 2008), operates within the framework of the IDL Virtual Machine, which is also available at no cost.[4] The tool can plot the crater statistics in the graphical presentation modes introduced by Arvidson et al. (1979). The cumulative crater frequency N_{cum}, which we preferred in this study, represents the number of craters in an area of diameters greater than, or equal to, the diameter of a specific crater. We use reference diameters of 1 and 10 km since the two chronology models are based on cratering rates for either 1 km or 10 km craters.

To obtain relative ages from a specific measurement, the Ganymede PF is approximated to the measured CSFD with the PTA method (Michael et al. 2016) by selecting an upper and lower boundary crater diameter. Like finding a PF polynomial for, e.g., Ganymede, this method is subjective: an interpreter tests different diameter boundaries until a "best" fit of the curve to the data is found visually (see the examples in Figures 6, 8, 10, etc.). When this procedure is carried out in the craterstats 2.0 software tool, the cumulative frequency for a crater equal to, or larger than 1 km (default), is directly obtained from the curve, and this value is used to represent the relative age of the unit and included in tables (see Tables 2–10). In this study, we also used a reference diameter of 10 km since the JCM chronology by Zahnle et al. (2003) is based on the cratering

[3] The software can be accessed and downloaded at https://www.geo.fu-berlin.de/en/geol/fachrichtungen/planet/software/_content/software/craterstats.html.

[4] The craterstats 2.0 software can be accessed and downloaded at https://www.geo.fu-berlin.de/en/geol/fachrichtungen/planet/software/_content/software/craterstats.html.

Table A2
Coefficients p_1, p_2, and p_3 of the LDM Chronology for Ganymede (Neukum et al. 1998) in Comparison with the One for the Moon (Neukum & Ivanov 1994)

Coefficient p	Ganymede	Moon
p_1	1.055×10^{-14}	5.44×10^{-14}
p_2	6.93	6.93
p_3	1.625×10^{-4}	8.38×10^{-4}

rate for 10 km craters. In the PF polynomial (assumed as time invariant), the factor between the (cumulative) frequencies of any two specific crater diameters is always constant and can be used to transfer a chronology function to any crater diameter (here, N_{cum} (D ⩾ 1 km)/N_{cum} (D ⩾ 10 km) = 112.74).

The AMAs of the LDM chronology are obtained in craterstats 2.0 according to the equation (Neukum & Ivanov 1994; Neukum et al. 1998):

$$N_{\text{cum}}\ (D \geqslant 1\ \text{km}) = p_1 \times [e^{(p_2 \times t)} - 1] + p_3 \times t$$

.

The AMA t (in Ga) is numerically calculated from the cumulative frequency N_{cum} for craters larger than or equal to 1 km. The three coefficients p_1, p_2, and p_3 of the Ganymede LDM chronology are listed in Table A2 in comparison with the lunar coefficients. The equation consists of two summands: the left summand (coefficients p_1 and p_2) represents the part of the chronology dominated by an exponentially declining cratering rate prior to ∼3–3.3 Ga, while the right summand (coefficient p_3) is dominated by the constant cratering rate. For AMAs younger than ∼3–3.3 Ga the exponential term becomes negligible.

Currently, the JCM chronology has not yet been implemented in craterstats 2.0. JCM AMAs therefore are calculated in a separate program (*jcmchronage*, written in ANSI C by Roland Wagner) according to the formula (Zahnle et al. 1998, 2003):

$$t' = \frac{N_{\text{cum}}}{\dot{C}}$$

,with N_{cum} representing the cumulative frequency for crater diameters equal to, or greater than, 10 km. $\dot{C}$ is the constant cratering rate for craters $D \geqslant 10$ km and t' is the temporary model age in Ga for a constant cratering rate (Zahnle et al. 1998, 2003). We adopted the cratering rate of $\dot{C} = 1.8 \times 10^{-14}$ for Ganymede from Zahnle et al. (2003).

Using a constant cratering rate for dating the oldest surfaces on Ganymede would yield AMAs considerably older than the age of the solar system of $T = 4.56$ Ga. Zahnle et al. (1998; and references therein) introduced a term $1/t$ to account for secular variations in the cratering rate, and the "true" JCM AMA t in Ga then is calculated according to:

$$t = T \times [1 - e^{\left(-\frac{t'}{T}\right)}]$$

.

This term was not further discussed in the Zahnle et al. (2003) paper but is still held valid in their updated JCM chronology (K. Zahnle, personal communication). However, we found that the oldest units in the dark terrains, with LDM AMAs of ∼4 Ga, are dated about ∼4.56 Ga if using JCM AMAs, which thus suggests an unrealistic high age (larger than the solar system one).

A.1.2.2. Potential Variations of CSFDs with Distance from the Apex Point of Orbital Motion

ECs are heliocentric bodies impacting a synchronously rotating satellite asymmetrically with respect to distance to the apex of orbital motion (0° N latitude, 270° E longitude; Shoemaker & Wolfe 1982, Horedt & Neukum 1984a, 1984b; Zahnle et al. 1998, 2003; Schenk et al. 2004; Xu et al. 2017; Kirchoff et al. 2022). A theoretically derived pronounced asymmetry of a factor of 20–60 in the cratering rates at the apex with respect to the antapex point has not been observed on both Jovian (Galilean) or Saturnian satellites, however (Schenk et al. 2004 and references therein). These authors reported a ∼4 factor difference in crater frequencies in light terrain, much lower than the theoretically predicted values. In a more recent study, Xu et al. (2017) found apex–antapex asymmetries of only a factor of ∼2 in CSFDs on dark terrains and ∼3 in those on light terrains, for all measured crater diameters. Bright ray craters, predominantly those on light terrain, however, show a pronounced asymmetry with respect to the distance from the apex. Nonsynchronous rotation, possibly episodic, polar wander, and, much less likely, saturation equilibrium were offered as explanations for this little pronounced apex–antapex asymmetry (e.g., Schenk et al. 2004; Xu et al. 2017; Kirchoff et al. 2022 and references therein).

A.1.2.3. Summary: CSFDs and Surface Ages

1. To obtain relative ages and AMAs from crater counts, we used the buffered crater-counting approach for a CSFD measured in a mapped surface unit, based on Cratertool in ArcGIS (Kneissl et al. 2015, 2016; Riedel et al. 2018).
2. A polynomial PF for Ganymede derived from the lunar PF can be used to fit measured CSFDs independently of the SFD of impactors since collisional evolution produced similar shapes of CSFDs on the moon and on icy satellites of, e.g., Jupiter (Bottke et al. 2022).
3. The Ganymede PF is fit to a CSFD using the PTA procedure with the tool craterstats 2.0 (Michael et al. 2016) to obtain the relative age of a unit which is represented by the cumulative frequency for a 1 km or 10 km crater.
4. In the same procedural step, an AMA for LDM can be derived. The AMA for JCM is calculated in a separate software tool written by one of us (Wagner), based on the cumulative frequency for a 10 km crater.
5. The error handling in AMA for both models is still incompletely implemented in craterstats 2.0 but this task may be completed in the near term (G. Michael, personal communication).
6. Taking a potential uncertainty factor of 3 in the cratering rate into account for each of the two chronology models, the errors in the AMAs are on the order of ∼0.1–0.2 Ga for LDM ages older than ∼3.3 Ga, and considerably higher (∼ 0.5–1 Ga or even more) for LDM ages less than ∼3.3 Ga, or JCM ages less than ∼4 Ga.
7. Secondary craters may affect a measurement, especially near large ray craters, thus the "true" age could be lower.
8. Variations in the crater frequencies due to the distance to the apex point of orbital motion of a study area are less significant since, with the exception of two areas, most are within a comparable distance to the apex.

Appendix B

B.1. Effect of the Crater Counting Area on the CSFDs

The crater-counting methodology and the obtained model ages may critically depend on (i) the minimum area for crater counting, (ii) resurfacing in the light terrains, (iii) the presence of secondary craters, (iv) sesquinaries, and (v) recent large craters obliterating preexisting craters. We carefully avoided crater cluster or aligned crater chains that are indicative of secondary cratering. In order to assess the influence of the given crater counting areas on the obtained results, we systematically tested the dependency of the *N* values on the area used for the crater counting. The test was performed on the SSI images covering Mummu Sulci and Sippar Sulcus (Figure B1). We systematically varied the area of investigation from small to large values for the same region and recorded the variation in the *N* (10) values. We considered four different terrains: (a) reticulate terrain (r), (b) light grooved terrain lg_2, (c) light subdued terrain ls_3, and (d) light irregular terrain li_1.

For the four different terrains we varied the area of investigation in six steps. We started our test using a 800 km^2 area and enlarged the areas in each step by 800 km^2. So, the test areas are: test 1: 800, test 2: 1600, test 3: 2400, test 4: 3200, test 5: 4000, and test 6: 4800 km^2. In the reticulate terrain (Figure B2(a)), test 1 (800 km^2) has the lowest CSFD of 7.19×10^{-5} and test 2 (1600 km^2) has highest CSFD of 1.15×10^{-4}, and CSFDs of the other test areas fall between these two curves. From this, it is understood that there is no considerable variation in the CSFDs of larger areas and smaller areas. In lg_2 (Figure B2(b)), test 2 (of 1600 km^2) has the lowest CSFD of 6.23×10^{-5} and test 6 (4800 km^2) has the highest CSFD of 7.77×10^{-5}, and the CSFDs of other test areas fall between these two curves. Thus, all six tests values are very similar.

In ls_3 (Figure B2(c)), the curves of all test areas fall into a single curve and there is almost no variation in their CSFDs. The lowest CSFDs noted is 1.69×10^{-4} of test 5 (4000 km^2) and the highest is 1.82×10^{-4} of test 2 (1600 km^2). In li_1 (Figure B2(d)), test 1 (of 800 km^2) has the lowest CSFD of 1.99×10^{-5} and test 5 (of 4800 km^2) has the highest CSFD of 2.80×10^{-5}. To conclude there is no systematic area effect recognizable in the data sets. We, therefore, infer that the obtained CSFDs are independent of the investigated respective areas. Of course, this also means that the absolute ages derived from LDM and JCM are independent of area.

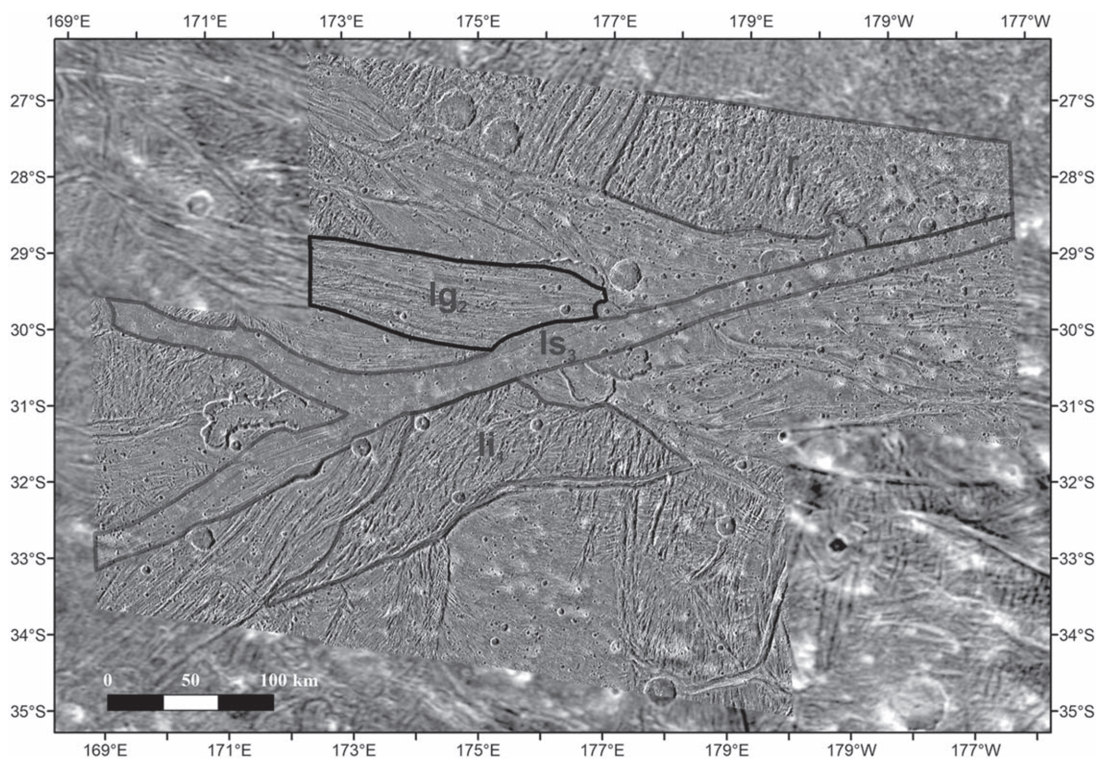

Figure B1. Test areas selected from Region D/Mummu and Sippar Sulcus (see Figure 13). Four different types of terrain units are used for the test, which have four different morphologies: reticulate terrain (r), light grooved terrain lg_2, light subdued terrain ls_3, and light irregular terrain li_1.

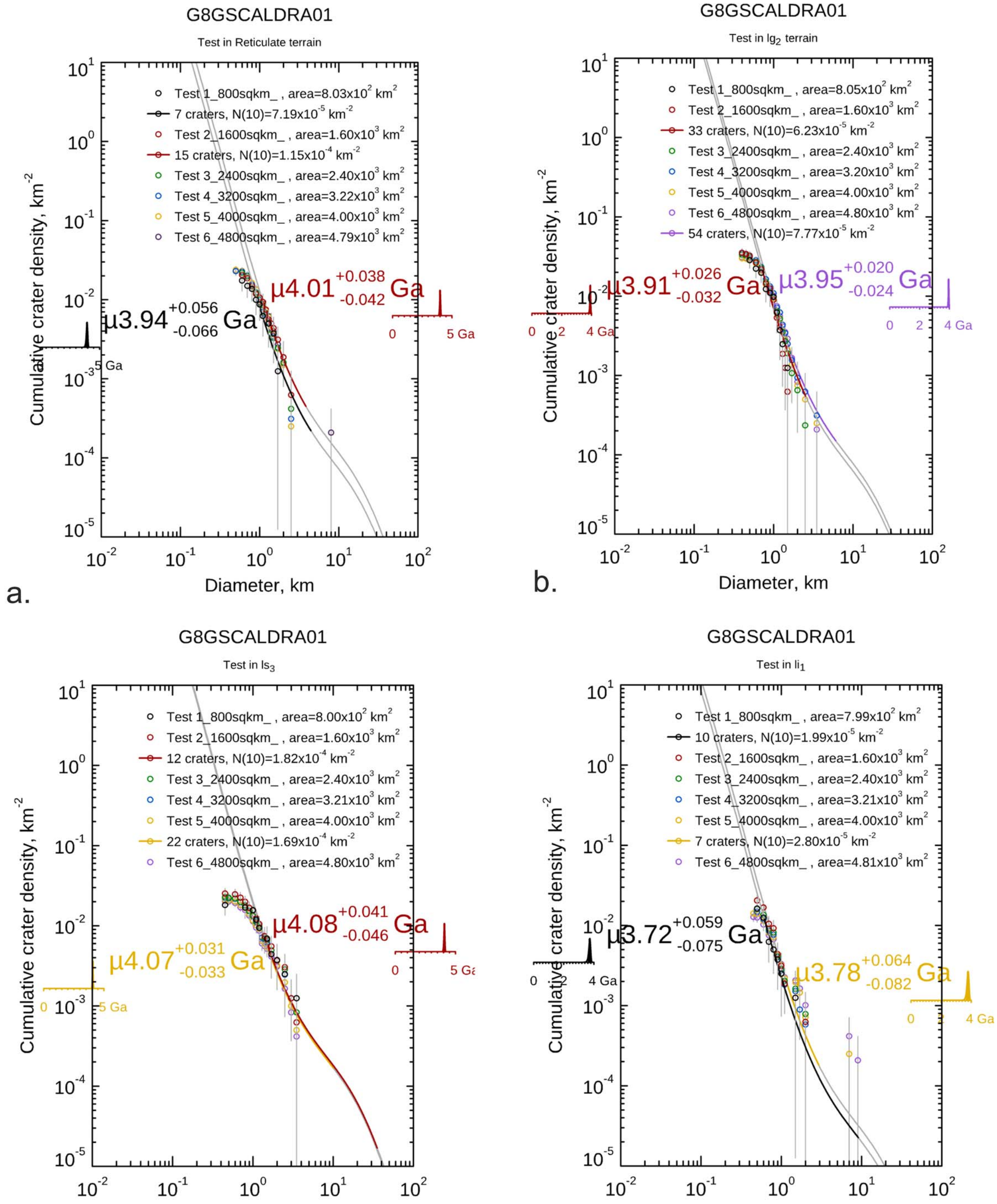

Figure B2. Histograms showing crater counts, CSFDs, and best curve fits for four different types of terrain units: (a) reticulate terrain (r), (b) light grooved terrain lg_2, (c) light subdued terrain ls_3, and (d) light irregular terrain li_1. In each of these individual terrain units, we consider six test areas: test 1 of 800 (black), test 2 of 1600 (red), test 3 of 2400 (green), test 4 of 3200 (blue), test 5 of 4000 (yellow), and test 6 of 4800 (violet) km^2. Two best-fit curves within each plot represents the test areas which have the lowest and highest crater CSFDs.

ORCID iDs

Namitha Rose Baby https://orcid.org/0000-0001-8032-9137

References

Alvarellos, J. L., Zahnle, K. J., Dobrovolskis, A. R., & Hamill, P. 2002, Icar, 160, 108
Archinal, B. A., A'Hearn, M. F., Bowell, E., et al. 2011, CeMDA, 109, 101
Arvidson, R., Guinness, E., & Lee, S. 1979, Natur, 278, 533
Baby, N. R., Stephan, K., Wagner, R., et al. 2022, EPSC, 16, 1016
Becker, T., Archinal, B., Colvin, T., et al. 2001, LPSC, 32, 2009
Belton, M. J. S., Klaasen, K. P., Clary, M. C., et al. 1992, SSRv, 60, 413
Benesh, M., & Jepsen, M. 1978, Voyager Imaging Science Subsystem Calibration Report 618-02, JPL, https://pds-rings.seti.org/voyager/iss/Benesh_Jepsen_1978.pdf
Bierhaus, E. B., Chapman, C. R., & Merline, W. J. 2005, Natur, 437, 1125
Bierhaus, E. B., Chapman, C. R., Merline, W. J., Brooks, S. M., & Asphaug, E. 2001, Icar, 153, 264
Bierhaus, E. B., McEwen, A. S., Robbins, S. J., et al. 2018, PlSci, 53, 638

Bland, M. T., Showman, A. P., & Tobie, G. 2009, Icar, 200, 207
Bland, M. T., Singer, K. N., McKinnon, W. B., & Schenk, P. M. 2017, Icar, 296, 275
Bottke, W. F., Marschall, F., Vokrouhlický, D., et al. 2022, LPSC, 2678, 2638
Bottke, W. F., Morbidelli, A., Jedicke, R., et al. 2002, Icar, 156, 399
Cameron, M. E., Smith-Konter, B. R., Burkhard, L., et al. 2018, Icar, 315, 92
Cameron, M. E., Smith-Konter, B. R., Collins, G. C., Patthoff, D. A., & Pappalardo, R. T. 2019, Icar, 319, 99
Cameron, M. E., Smith-Konter, B. R., Collins, G. C., Patthoff, D. A., & Pappalardo, R. T. 2020, JGRE, 125, e05995
Chapman, C. R., & McKinnon, W. B. 1986, Satellites (A87-23307 09-91) (Tucson, AZ: Univ. Arizona Press), 492
Choblet, G., Tobie, G., Sotin, C., Kalousova, K., & Grasset, O. 2017, Icar, 285, 252
Clark, R. N. 1980, Icar, 44, 388
Collins, G. C., Patterson, G. W., Head, J. W., et al. 2013, Global Geologic Map of Ganymede Scientific Investigations Map 3237, USGS
Crater Analysis Techniques Working Group 1979, Icar, 37, 467
Danielson, G. E., Kupferman, P. N., Johnson, T. V., & Soderblom, L. A. 1981, JGR, 86, 8683
Davies, M. E., Colvin, T. R., Oberst, J., et al. 1998, Icar, 135, 372
Davies, M. E., & Katayama, F. Y. 1981, JGR, 86, 8635
Dones, L., Chapman, C. R., McKinnon, W. B., et al. 2009, in Saturn from Cassini-Huygens., ed. M. K. Dougherty, L. W. Esposito, & S. M. Krimigis (Dordrecht: Springer), 613
The JUICE Science Working Team 2014, JUICE Jupiter ICy Moons Explorer 10 Exploring the Emergence of Habitable Worlds around Gas Giants, Definition Study Report ESA/SRE(2014)1, https://sci.esa.int/documents/33960/35865/1567260128466-JUICE_Red_Book_i1.0.pdf
Giese, B., Wagner, R., Neukum, G., et al. 2001, LPSC, 32, 1743
Grasset, O., Dougherty, M. K., Coustenis, A., et al. 2013, P&SS, 78, 1
Guest, J. E., Bianchi, R., & Greeley, R. 1988, Geologic Map of the Uruk Sulcus Quadrangle of Ganymede IMAP 1934, USGS
Hartmann, W. K. 1984, Icar, 60, 56
Head, J., Pappalardo, R., Collins, G., et al. 2002, GeoRL, 29, 2151
Head, J. W., Pappalardo, R. T., Collins, G., Greeley, R. & Galileo IMAGING Team 1997, LPSC, 28, 535
Head, J. W., Pappalardo, R. T., Kay, J., et al. 1998, LPSC, 29, 1666
Hiesinger, H., Jaumann, R., Neukum, G., & Head, J. W., III 2000, JGR, 105, 29239
Hiesinger, H., Marchi, S., Schmedemann, N., et al. 2016, Sci, 353, aaf4758
Horedt, G. P., & Neukum, G. 1984a, Icar, 60, 710
Horedt, G. P., & Neukum, G. 1984b, JGR, 89, 10405
Ivanov, B. A., Neukum, G., Bottke, W. F., Jr, & Hartmann, W. K. 2002, in Asteroids III., ed. W. F. Bottke, Jr et al. (Tucson, AZ: Univ. Arizona Press), 89
Jaumann, R., Stephan, K., Wagner, R., et al. 2022, in Ganymede, ed. M. Volwerk et al. (Cambridge: Cambridge Univ. Press) in press
Kay, J. E., & Head, J. W., III 1999, LPSC, 30, 1103
Kersten, E., Zubarev, A. E., Roatsch, T., & Matz, K.-D. 2021, P&SS, 206, 105310
Kirchoff, M. R., Barr, A., Bland, M., et al. 2022, in Ganymede, ed. M. Volwerk et al. (Cambridge: Cambridge Univ. Press) in press
Kirchoff, M. R., Bierhaus, E. B., Dones, L., et al. 2018, Enceladus and the Icy Moons of Saturn (Tucson, AZ: Univ. Arizona Press), 267
Klaasen, K. P., Clary, M. C., & Janesick, J. R. 1984, OptEn, 23, 334
Kneissl, T., Michael, G. G., & Schmedemann, N. 2016, Icar, 277, 187
Kneissl, T., Michael, G. G., Platz, T., & Walter, S. H. G. 2015, Icar, 250, 384
Kneissl, T., van Gasselt, S., & Neukum, G. 2011, P&SS, 59, 1243
Le Feuvre, M., & Wieczorek, M. A. 2011, Icar, 214, 1
Lucchita, B. K. 1980, Icar, 44, 481
Marchi, S., Massironi, M., Cremonese, G., et al. 2011, P&SS, 59, 1968
Marchi, S., Mottola, S., & Cremonese, M. E. 2009, AJ, 137, 4936
Massironi, M., Cremonese, G., Marchi, S., et al. 2009, GeoRL, 36, L21204
McEwen, A. S., Preblich, B. S., Turtle, E. P., et al. 2005, Icar, 176, 351
Mckinnon, W. B., & Parmentier, E. M. 1986, in Satellites, ed. J. A. Burns & M. S. Matthews (Tucson, AZ: Univ. Arizona Press), 718
McKinnon, W. B., Schenk, P. M., & Moore, J. M. 2001, LPSC, 32, Abstr. No. 2179, XXXII
Michael, G., & Neukum, G. 2008, 39th Annual LPSC, 1391, 1780
Michael, G. G., Kneissl, T., & Neesemann, A. 2016, Icar, 277, 279
Michael, G. G., & Neukum, G. 2010, E&PSL, 294, 223
Moore, J. M., Asphaug, E., Morrison, D., et al. 1999, Icar, 140, 294
Mueller, S., & McKinnon, W. B. 1988, Icar, 76, 437
Murchie, S. L., & Head, J. W. 1988, JGRB, 93, 8795
Murchie, S. L., & Head, J. W., III 1986, GeoRL, 13, 345
Nagel, K., Breuer, D., & Spohn, T. 2004, Icar, 169, 402
Neukum, G., & Horn, P. 1976, The Moon, 15, 205
Neukum, G., & Ivanov, B. A. 1994, in Hazards due to Comets and Asteroids, ed. T. Gehrels (Tucson, Az.: Univ. of Arizona Press), 359
Neukum, G., Ivanov, B. A., & Hartmann, W. K. 2001, SSRv, 96, 55
Neukum, G., Wagner, R., Wolf, U., et al. 1998, LPSC, 29, 1742
Nimmo, F. 2004, JGRE, 109, E01003
Nimmo, F., & Pappalardo, R. T. 2004, GeoRL, 31, L19701
Öpik, E. J. 1960, MNRAS, 120, 404
Palumbo, P., Jaumann, R., Cremonese, G., et al. 2014, EGUGA, 16, 10227
Pappalardo, R. T., & Collins, G. C. 2005, JSG, 27, 827
Pappalardo, R. T., Collins, G. C., Head, J. W., III, et al. 2004, in Jupiter. The Planet, Satellites, and Magnetosphere, ed. F. Bagenal, T. E. Dowling, & W. B. McKinnon (Cambridge: Cambridge Univ. Press), 363
Patterson, G. W., Collins, G. C., Head, J. W., et al. 2010, Icar, 207, 845
Prockter, L. M., Head, J. W., Pappalardo, R. T., et al. 1998, Icar, 135, 317
Richardson, J. E. 2009, Icar, 204, 697
Riedel, C., Michael, G., Kneissl, T., et al. 2018, E&SS, 5, 258
Robbins, S. J., Riggs, J. D., Weaver, B. P., et al. 2018, M&PS, 53, 891
Schenk, P. M. 2002, Natur, 417, 419
Schenk, P. M., Chapman, C. R., Zahnle, K., & Moore, J. M. 2004, in Jupiter. The Planet, Satellites, and Magnetosphere, ed. F. Bagenal, T. E. Dowling, & W. B. McKinnon (Cambridge: Cambridge Univ. Press), 427
Schenk, P. M., McKinnon, W. B., Gwynn, D., & Moore, J. M. 2001, Natur, 410, 57
Schenk, P. M., & Moore, J. M. 1998, In Solar System Ices, Astrophysics and Space Science Library, Vol. 227 (Dordrecht: Kluwer), 551
Schubert, G., Stevenson, D. J., & Ellsworth, K. 1981, Icar, 47, 46
Shoemaker, E., & Wolfe, R. F. 1982, in Satellites of Jupiter, ed. D. Morrison (Tucson, AZ: Univ. Arizona Press), 277
Shoemaker, E. M., Lucchitta, B. K., Wilhelms, D. E., Plescia, J. B., & Squyres, S. W. 1982, in Satellites of Jupiter (Tucson, AZ: Univ. Arizona Press), 435
Shoemaker, E. M., Wolfe, R. F., & Shoemaker, C. S. 1986, LPSC, 17, 799
Showman, A. P., & Malhotra, R. 1997, Icar, 127, 93
Showman, A. P., Mosqueira, I., & Head, J. W., III 2004, Icar, 172, 625
Showman, A. P., Stevenson, D. J., & Malhotra, R. 1997, Icar, 129, 367
Singer, K. N., McKinnon, W. B., Gladman, B., et al. 2019, Sci, 363, 955
Singer, K. N., McKinnon, W. B., & Nowicki, L. T. 2013, Icar, 226, 865
Smith, B. A., Briggs, G. A., Danielson, G. E., et al. 1977, SSRv, 21, 103
Smith, B. A., Soderblom, L. A., Johnson, T. V., et al. 1979a, Sci, 204, 951
Smith, B. A., Soderblom, L. A., Beebe, R., et al. 1979b, Sci, 206, 927
Sohl, F., Spohn, T., Breuer, D., & Nagel, K. 2002, Icar, 157, 104
Spaun, N. A., Head, J. W., III, Pappalardo, R. T. & Galileo SSI Team 2001, LPSC, 32, 1448
Spencer, J. R. 1987, Icar, 70, 99
Squyres, S. W. 1980, GeoRL, 7, 593
Stephan, K., Roatsch, T., Tosi, F., et al. 2021, P&SS, 208, 105324
Strom, R. G., Malhotra, R., Ito, T., Yoshida, F., & Kring, D. A. 2005, Sci, 309, 1847
Strom, R. G., Marchi, S., & Malhotra, R. 2018, Icar, 302, 104
Wagner, R., Head, J. W., III, Wolf, U., & Neukum, G. 2010, JGRE, 115, E06015
Wagner, R., Stephan, K., Schmedemann, N., et al. 2018, EPSC, 12, 855
Wagner, R. J., Schmedemann, N., Werner, S. C., et al. 2017, EPSC, 11, 470
Wagner, R. J., Schmedemann, N., Werner, S. C., et al. 2019, EGUGA, 21, 7208
Werner, S. C., & Ivanov, B. A. 2015, in Treatise on Geophysics—Planets and Moons, Vol. 10, ed. G. Schubert (2nd ed.; Amsterdam: Elsevier), 327
Wilhelms, D. E. 1997, Geologic Map of the Osiris (Jg-12) and Apsu Sulci (Jg-13) Quadrangles of Ganymede IMAP 2442, USGS
Woronow, A. 1978, Icar, 34, 76
Xu, L., Hirata, N., & Miyamoto, H. 2017, Icar, 295, 140
Zahnle, K., Alvarellos, J. L., Dobrovolskis, A., & Hamill, P. 2008, Icar, 194, 660
Zahnle, K., Dones, L., & Levison, H. F. 1998, Icar, 136, 202
Zahnle, K., Schenk, P., Levison, H., & Dones, L. 2003, Icar, 163, 263
Zubarev, A., Nadezhdina, I., Oberst, J., Hussman, H., & Stark, A. 2015, P&SS, 117, 246
Zubarev, A. E., Nadezhdina, I. E., Brusnikin, E. S., Karachevtseva, I. P, & Oberst, J 2016, SoSyR, 50, 352
Zuber, M. T., & Parmentier, E. M. 1984, Icar, 60, 200